Crystal growth and physical properties of Ferro-pnictides

Dissertation

zur Erlangung des akademischen Grades
Doctor rerum naturalium (Dr. rer. nat.)

vorgelegt

der Fakultät Mathematik und Naturwissenschaften
der Technischen Universität Dresden

von

M.Sc.-Physics. **Saicharan Aswartham**
geboren am 25. April 1983 in Guntakal, India

Gutachter: Prof. Dr. B. Büchner
: Prof. Dr. C. Felser

Tag der Einreichung: 14. August 2012
Tag der Disputation: 8. November 2012

Contents

1 **Introduction** **1**
- 1.1 Fe-As superconductors . . . 3
- 1.2 Single crystals . . . 8

2 **Experimental Techniques** **11**
- 2.1 Synthesis of precursor materials . . . 11
  - 2.1.1 FeAs . . . 11
  - 2.1.2 BaAs . . . 13
  - 2.1.3 KAs . . . 13
- 2.2 High temperature solution growth . . . 14
- 2.3 X-ray diffraction . . . 17
- 2.4 Energy dispersive X-ray spectroscopy . . . 17
- 2.5 Inductively coupled plasma spectroscopy . . . 18
- 2.6 Magnetization measurements . . . 19
- 2.7 Resistivity measurements . . . 19

3 **Unified phase diagram of $BaFe_2As_2$ single crystals** **21**
- 3.1 Introduction . . . 21
- 3.2 $Ba(Fe_{1-x}Co_x)_2As_2$ . . . 23
  - 3.2.1 Crystal growth . . . 23
    - Self-flux technique(SFT) . . . 23
  - 3.2.2 Characterization . . . 26
  - 3.2.3 Resistivity measurements . . . 26
  - 3.2.4 Magnetization measurements . . . 30
  - 3.2.5 Ac susceptibility measurements . . . 34
  - 3.2.6 Summary and conclusions . . . 34
- 3.3 $Ba_{1-x}Na_xFe_2As_2$ . . . 36
  - 3.3.1 Crystal growth . . . 36
  - 3.3.2 Characterization . . . 37
  - 3.3.3 Magnetization measurements . . . 38
  - 3.3.4 Resistivity measurements . . . 42
  - 3.3.5 Summary and conclusions . . . 43
- 3.4 Unified phase diagram . . . 44

4 Suppression of superconductivity with charge doping in LiFeAs 47
4.1 Introduction 47
4.2 Crystal growth 49
4.3 Characterization 50
4.3.1 Inductively coupled plasma spectroscopy 50
4.3.2 Energy dispersive spectroscopy and x-ray diffraction 51
4.4 Magnetization measurements 52
4.5 Resistivity measurements 53
4.6 Summary and Conclusion 55

5 Influence of doping in KFe_2As_2 single crystals 57
5.1 Introduction 57
5.2 Crystal growth 59
5.2.1 FeAs flux 59
5.2.2 KAs flux 60
5.3 Characterization 60
5.4 Magnetization measurements 61
5.5 Resistivity measurements 62
5.6 Influence of doping 66
5.6.1 $(K_{1-x}Na_x)Fe_2As_2$ 66
5.6.2 $K(Fe_{1-x}Tm_x)_2As_2$ 67
5.7 Summary and Conclusion 70

6 Influence of Eu in $BaFe_2As_2$ single crystals 73
6.1 Introduction 73
6.2 Crystal growth and characterization 74
6.3 Magnetization measurements 75
6.4 Resistivity measurements 78
6.5 ESR measurements 79
6.6 Summary and Conclusion 80

7 Summary/conclusions and Outlook 81

List of publications 93

Bibliography 97

Acknowledgements 109

Eidesstattliche Erklärung 111

1 Introduction

One of the most fascinating scientific achievements of 20th century physics is superconductivity, discovered in April 1911 by Kamerlingh Onnes at the University of Leiden. To his surprise Onnes observed a rapid vanishing of resistivity below the critical temperature of around 4 K in metallic mercury [1]. Another landmark discovery in the field of superconductivity is the Meissner Ochsenfeld effect, discovered by Walther Meissner and Robert Ochsenfeld by measuring the magnetic field down to the critical temperature in lead and tin samples. They found out that below the superconducting transition temperature the samples expell the magnetic fields showing an ideal diamagnetic behaviour [2]. This phenomenon led to a new definition of superconductor, i.e., all superconductors below the critical temperature are perfect diamagnets. Though not fully understood even after 100 years of its discovery, superconductors still it finds potential applications in our day to day life, just to mention a few e.g., strong electromagnets used for Magnetic Resonance Imaging (MRI) and Nuclear magnetic resonance (NMR) are made up of superconductors. Many theories have been developed to understand the mechanism of superconductivity over the past century, among the most promising theories were, the Ginzburg-Landau theory [3] and Bardeen-Cooper-Schrieff (BCS) theory [4]. Ginzburg-Landau theory does not provide any microscopic explanation for the superconducting mechanism but is rather focused on the macroscopic properties like thermodynamic

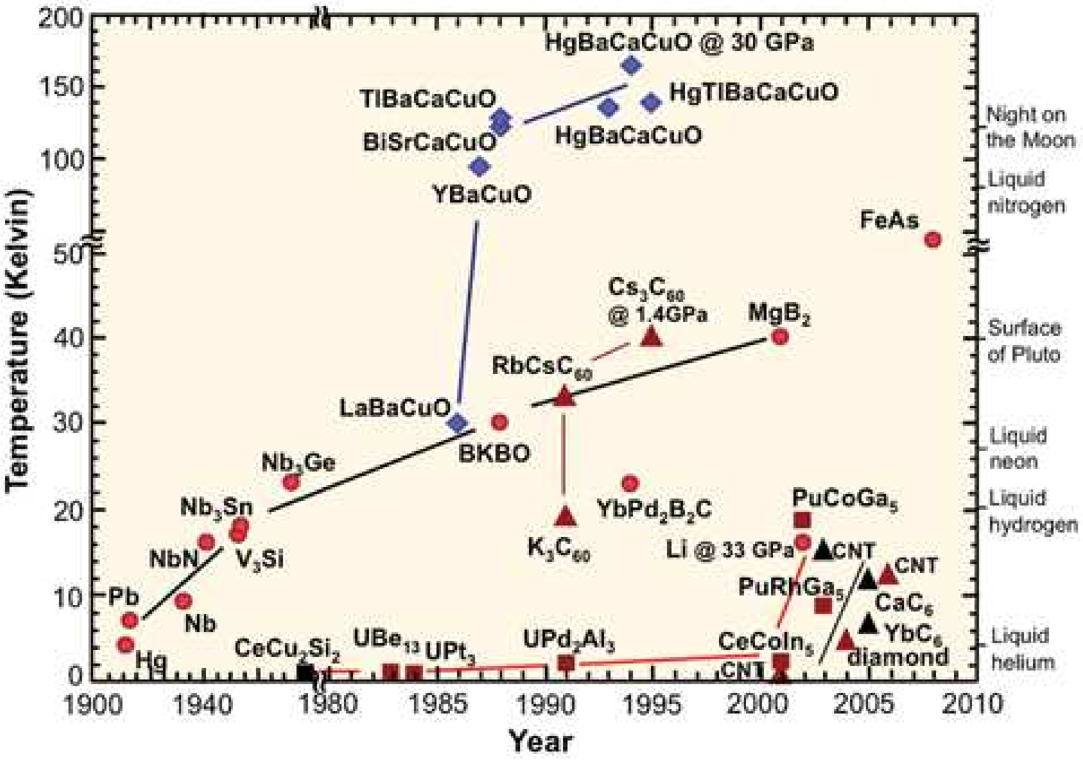

Figure 1.0.1: Superconductivity over the years. [Image courtesy of DOE, US. [5]]

properties [3]. BCS theory is the only theory which gave a microscopic explanation of the superconductivity so far, and all the conventional superconductors can be explained within BCS theory [4]. Fig 1.0.1 shows the discoveries of new superconductors that had taken place over the past century. The first unconventional superconductors were the heavy fermion superconductors discovered in 1978 [6], but the real surprising result was the discovery of high temperature superconductivity in ceramic materials with perovskite like structure, the renowned copper oxide superconductors (cuprates) [7]. Strontium ruthenate also belongs to the list of the family of unconventional superconductors [8], and strontium ruthenate is yet the only superconductor with the perovskite structure without copper. The newly discovered Fe-As superconductors [9] also belong to the "uncoventional list". It seems so far that the most common feature among all the above mentioned uncoventional superconductors are the competing orders or coexistence of magnetism and superconductivity [10]. In the scientific community working in superconductivity it is commonly believed that magnetism in these materials has to be understood in order to understand the superconductivity.

This thesis describes the single crystal growth of Fe-based superconductors, and the thesis is organised in the following way. Chapter 1 gives a brief introduction to the Fe-based superconductors and a few words about the essentials of single crystals in fundamental research. In chapter 2, experimental techniques which are used in this thesis work are explained, like the solution growth technique, characterization techniques and physical property measurements. Chapter 3 presents the crystal growth, characterization and superconducting properties of high quality single crystals of electron and hole doped $BaFe_2As_2$. In this chapter a unified phase diagram is constructed for the $BaFe_2As_2$ system. In chapter 4, crystal growth of $LiFe_{1-x}Co_xAs$ grown from self-flux will be explained, this chapter presents more insight into the LiFeAs system, which is different in many aspects compared to the rest of the Fe-based superconductors. KFe_2As_2 is another special member of Fe-based superconductors, with its peculiar characteristics. In chapter 5 single crystals of KFe_2As_2 grown from two different fluxes, namely FeAs-flux and KAs-flux are explained and the influence of doping with selected elements like Na, Rh, Co and Cr has been presented in this chapter. Where as in chapter 6, I have explained a different type of susbtitution in $BaFe_2As_2$ system. This chapter presents crystal growth, magnetic and superconducting properties of Eu-susbstituted $BaFe_2As_2$ single crystals. Finally I summarized all these results by presenting a short outlook.

1.1 Fe-As superconductors

In this section, I will focus on the most recently discovered unconventional superconductors, i.e., the Fe-based high temperature superconductors. In 2008, the first Fe-based

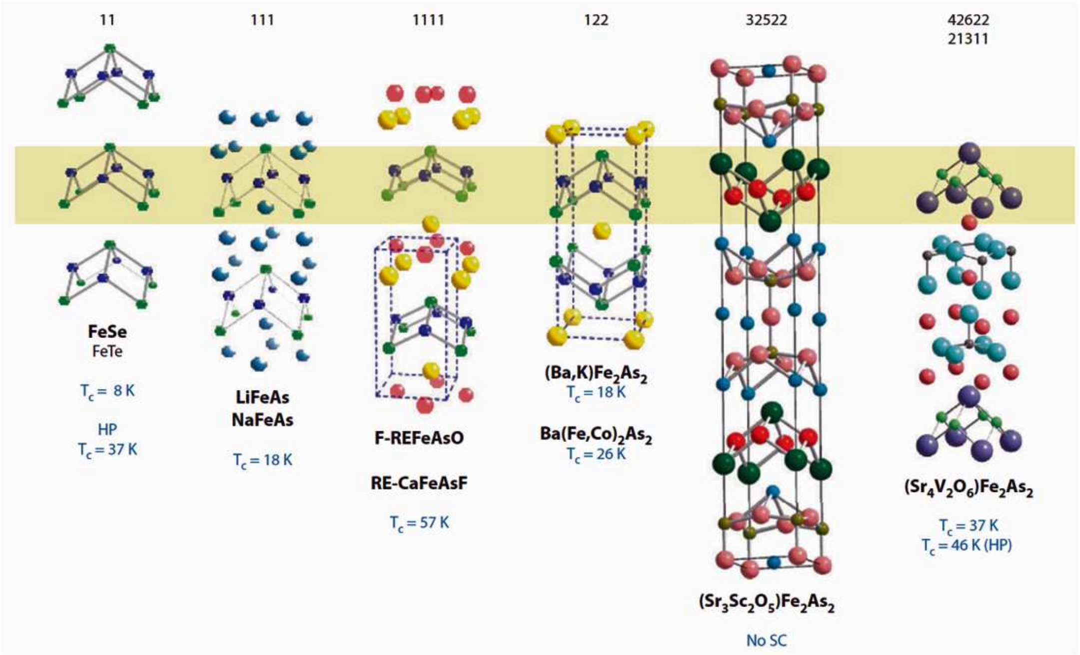

Figure 1.1.1: Six different types of crystal structures from Fe-As superconductors [11]

high temperature superconductor was discovered by the Kamihara et al.[9] with a transition temperature of 26 K in $LaFeAsO_{1-x}F_x$ with x=0.1. Within a short period of time the superconducting transition has reached as high as 55 K in $SmFeAsO_{1-x}F_x$ [12] which is the highest superconducting transition temperature besides cuprates. The discovery of Fe-based superconductors has clearly overthrown the monopoly of copper in high temperature superconductivity. Fig 1.1.1 shows six different types of crystal structures of Fe-based superconductors. Classification of the Fe-based superconductors are based on the stoichiometry of the parent compounds as ”11”, ”111”, ”122”, ”1111”, ”32522” and ”42622” families as shown in Fig 1.1.1. The common feature in all these families of Fe-based materials are the Fe-Pn (Pn; pnictogen or chalcogenide) layers, which are believed to be responsible for the superconductivity. At first it is worth to discuss the ”1111” family which holds the highest critical temperature T_c, the parent compound with general notation RFeAsO (R: rare earth), belongs to the ZrCuSiAs type with the

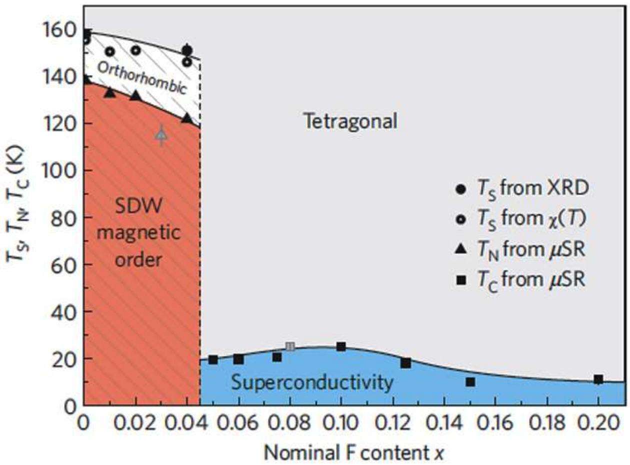

Figure 1.1.2: Electronic phase diagram of LaFeAsO$_{1-x}$F$_x$ showing structural (T_S), magnetic (T_N) and superconducting transition (T_c) temperatures [13]

space group of P4/nmm. Fig 1.1.2 shows the phase diagram of LaFeAsO$_{1-x}$F$_x$[13]. The undoped parent compound under goes a structural transition at T_S=158 K from space group P4/nmm to space group P112/n at low temperatures, immediately followed by an antiferromagnetic SDW transition at T_N=134 K [13, 14]. With fluorine doping, T_S and T_N are suppressed and bulk superconductivity evolves. With x = 0.10 in LaFeAsO$_{1-x}$F$_x$ is an optimally doping which leads to the highest critical temperature T_c of 26 K. In the case of LaFeAsO$_{1-x}$F$_x$ there is a clear seperation between magnetic order and superconductivity, specifically the compound with x = 0.04 is at the border between magnetic order and superconductivity as shown in the Fig 1.1.2. In case of the SmFeAsO$_{1-x}$F$_x$ there is coexistence region with x = 0.1 to 0.15, where magnetic order and superconductivity overlap with each other [15].

The second important familiy is the so called "122", the parent compound with general notation AFe$_2$As$_2$ (A=Ba, Sr, Ca, Eu) which belongs to the ThCr$_2$Si$_2$-type structure. In contrast to the "1111" family, the undoped parent compound show a concomitant structural T_S and magnetic transition T_N at low temperatures for example in BaFe$_2$As$_2$ T$_0$=T$_{S/N}$=137 K [16], in CaFe$_2$As$_2$ T$_0$=T$_{S/N}$=172 K [17], in SrFe$_2$As$_2$ T$_0$=T$_{S/N}$=198 K

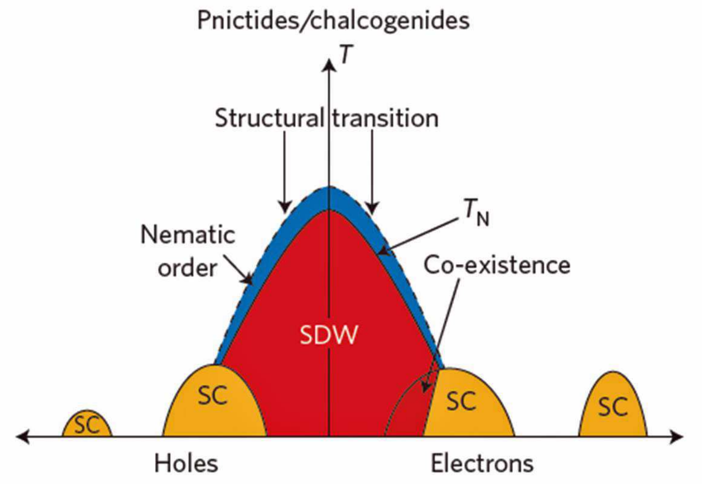

Figure 1.1.3: The generic phase diagram of electron and hole doping in Fe-As superconductors, showing structural (T_S), magnetic (T_N) and superconducting transition (T_c) temperatures [21].

[18] and for $EuFe_2As_2$ T_0=$T_{S/N}$=200 K [19, 20]. Superconductivity can be achieved by suppressing these structural and magnetic transitions. Superconductivity is introduced within 122 either by doping with holes or with electrons. Fig 1.1.3 shows the proposed unified phase diagram of electron and hole doping in Fe-As superconductors [21]. For example, in $BaFe_2As_2$ superconductivity is achieved by either "hole" doping with K with the maximum T_c=38 K, or superconductivity is achieved by "electron" doping with Co with the maximum T_c=25 K (see Fig 1.1.4). Here it is worth mentioning the two special cases in the phase diagram both of which are also belong to 122 family, namely, extremely hole doped KFe_2As_2 and extremely electron doped KFe_2Se_2.

The third family is the so called "111", with the general notation AFeAs (A= Li, Na). The "111" series class orders in Cu_2Sb type structure. LiFeAs is a unique member of Fe-As superconductors because of its peculiar characteristics like the absence of structural and magnetic transitions. Superconductivity arises in the stoichiometric LiFeAs with maximum T_c=18 K [24]. Superconductivity was also found in NaFeAs with maximum T_c=9 K [25] which is isostructural to LiFeAs, but there are substantial differences

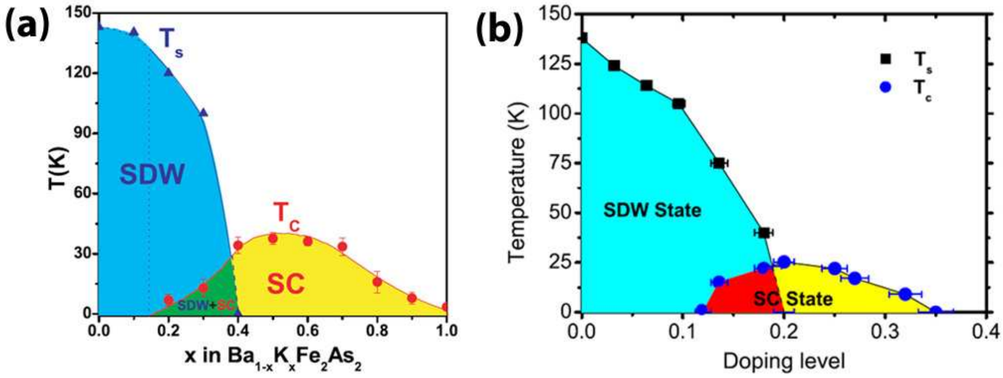

Figure 1.1.4: (a) K-doped BaFe$_2$As$_2$ phase diagram (b) Co-doped BaFe$_2$As$_2$ phase diagram [22, 23]

between these two set of isostructural superconductors. There is no bulk superconductivity in stoichiometric NaFeAs but a structural transition at T_S = 50 K [26], a magnetic transition around T_N=40 K [25] similar to the rest of the Fe-As families. In Na-deficient samples of Na$_{1-\delta}$FeAs the transition temperature is raised to T_c=23 K, here Na deficiency acts like a self doping inducing holes.

The fourth family is "11", superconductivity has been reported in β-FeSe with transition temperature of T_c=8 K [27], which belongs to the PbO-type structure shown in Fig 1.1.1. In FeSe structure, Fe-As layers have been replaced by Fe-Se layers and this is the most simple crystal structure among all known Fe-As superconductors. With Te-substitution in β-FeSe$_{1-x}$Te$_x$ the superconducting transition has found to increase upto T_c=15 K with x = 0.5. On the other side of the phasediagram, pure FeTe is not a superconductor [28]. Moreover, Fe$_{1+y}$Se$_x$Te$_{1-x}$ undergoes a structural transition at T_S = 67 K from tetragonal-to-monoclinic and develops antiferromagnetic order [29].

Although the T$_c$ of the 1111 family is found to be highest among the Fe-based superconductors, their intrinsic properties, e.g. their detailed electronic structure, are yet unexplored as the growth of large and high quality single crystals is challenging and requires high pressure yielding tiny crystals only [30]. The families of "122", "111", "11" are relatively easy to grow in the form of single crystals, as the melting point of these compounds are with in accessable range in ambient pressures. This fact gives the possibility to grow large homogeneous single crystals with the high temperature solution growth technique. In this thesis, I will present a systematic study on crystal growth by high temperature solution growth technique to grow crystals of compounds corresponding to ”122” and ”111” families of Fe-based superconductors.

1.2 Single crystals

In experimental solid state physics/chemistry single crystals occupy a unique position especially in fundamental research. Single crystals always have an advantage over polycrystalline samples because of the absence of grain boundaries and often with less impurities. Physical properties of single crystals are anisotropic in nature and depends on the crystallographic orientation. For advanced and sophisticated measurements like angle resolved photoemission spectroscopy (ARPES), de Haas-van Alphen (dHvA), scanning tunnelling microscopy (STM) high quality single crystals with well determined orientation are essential. This underlines the important role of crystal growth in experimental solid state research. Many different techniques have been developed to grow single crystals, namely solution growth, Bridgman-Stockbarger, Czochralski, floating zone etc. In case of Fe-based superconductors most of the compounds are incongruently melting with the elements having high vapour pressure. The incongruently melting behaviour and the elements with high vapour pressure are the strong limiting points in employing the appropriate growth technique to be used for single crystal growth of Fe-based superconductors. The high temperature solution growth technique has the potential to control high vapour pressures and allows to grow single crystals from incongruently melting materials. So it is obvious to start with the solution growth for these type of incongruently melting materials like Fe-based superconductors. However the Bridgman method was also sucessfully applied by slightly modifing the growth conditions as discussed in [31]. In this work, I explore the high temperature solution growth technique for the growth of Fe-As superconductors.

2 Experimental Techniques

2.1 Synthesis of precursor materials

The first step in all single crystal growth experiments consisted of the preparation of the corresponding precursor materials such as: FeAs, Fe_2As, Co_2As, BaAs and KAs. It should be noted here that the entire room temperature processing, i.e., weighing, mixing, grinding and storage were carried out in an Ar-filled glove-box, where O_2 and moisture level was maintained to be less than 0.1 ppm.

2.1.1 FeAs

To react As with Fe or Co, sublimated As lumps (Alfa Aesar; purity 99.999%) and Fe(Co) powder (Alfa Aesar; purity 99.998% (Fe) and Hereaus 99.8% (Co)) were weighed in the desired molar ratio, mixed and ground to form a homogeneous powder, which was pressed in a stainless steel dye to form pellets of diameter ø=10 mm. These pellets (altogether weighing around 10 g) were sealed in 15 cm long silica tube under a high-vacuum ($\approx 10^{-6}$ mbar), and subsequently heated up to 973 K with a rate of 300 K/h and a dwelling time of 10 h in a horizontal tubular furnace under flowing Argon gas (as a protective measure). Fig 2.1.1 shows freshly pressed pellets of FeAs which were sealed in silica tube.

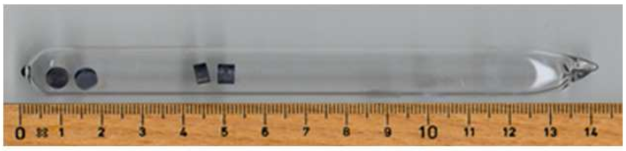

Figure 2.1.1: Pressed pellets of FeAs before the heat treatment in the sealed quartz tube with vacuum inside

Figure 2.1.2: Specially designed silica tube with glassy carbon crucible inside for the vapour transport reaction of BaAs.

2.1.2 BaAs

The reaction of As and alkali earth metals is known to be highly exothermic in nature, therefore the preparation of the precursor material BaAs was done by avoiding any direct physical contact between As and Ba. Therefore, chemical vapour transport was used to prepare BaAs from the elements. Sublimated As lumps (Alfa Aesar; purity 99.999%) and Ba shots (Sigma Aldrich Ch.; purity 99.99%) were weighed in molar ratio 1:1. Fig 2.1.2 shows the specially designed silica tube with a glassy carbon crucible placed inside. The weighed amount of arsenic was placed at the bottom of a silica tube (diameter 45 mm). The Ba shots were loaded in a glassy carbon crucible, which was carefully lowered into the silica tube to rest on the As heap. The tube was subsequently sealed under high-vacuum condition and placed in a muffle furnace. The temperature was gradually raised to 973 K over a period of 3 days, followed by a dwell of about 24 h and subsequent cooling to room temperature at 300 K/h. At the end of the experiment, all the As was found to have reacted with the Ba chunks forming a dark grey solid lump that was easy to remove from the crucible. These precursors were used in the subsequent crystal growth experiments.

2.1.3 KAs

As I already mentioned in section 2.1.2, the reaction between As and alkali earth metals is known to be highly exothermic, moreover metallic K reacts violently with oxygen and air moisture. So the reaction of As with metallic K was performed under different conditions compared to a conventional solid state reaction. For the reaction sublimated As lumps (Alfa Aesar; purity 99.999%) and metallic K ingot (Sigma-Aldrich purity 99.95%) were used. The melting point of metallic K is around 337 K, so for the reaction of K-As, at first a mortar is heated near to the melting point of the K. The hot mortar is then transferred into the glovebox where small metallic pieces of K from the ingot are droped in to the hot mortar which melts K immediatly. Now slowly As lumps were added to the liquid K and mixed properly with pestle. Even though this procedure was done at relatively slow pace to avoid a rapid reaction because of the exothermic reaction between K and As, small sparks were observed at the time of mixing. The well ground mixture is filled into the alumina crucible and sealed in the niobium crucible under Ar atmosphere. The sealed crucible assembly is placed in a vertical furnace, slowly heated with the rate of 25 K/h up to 373 K by a dwell of about 5 h and heated again with the rate of 25 K/h up to 573 K by a dwell of about 5 h. Finally the furnace is cooled to room temperature.

2.2 High temperature solution growth

In solution growth technique, the important criteria is solubility, i.e., achieving a supersaturated solution between the solute and the solvent. The supersaturation Δs is defined as $\Delta s = c - s_{(eq)}$, where c is the actual concentration and $s_{(eq)}$ is the equilibrium solubility [32]. Fig 2.2.1 shows a typical solubility curve as a function of temperature. In the Fig 2.2.1 the region above the line is supersaturated, which means the solution contains more than the equilibrium concentration of solute. Supersaturated solutions are not stable and will spontaneously nucleate in the solution or deposit on the walls of the container forming small crystals of the solute. Under optimized conditions, if a seed crystal is introduced in to the supersaturated solution, the excess solute will deposit on to it and grows as a large single crystal. In solution growth technique the solution has to be maintained in supersaturated state during the crystallization and as the concentration of the solution changes, the temperature has to be lowered to maintain the supersaturation. The solute is crystallizing from the solution, so both temperature and

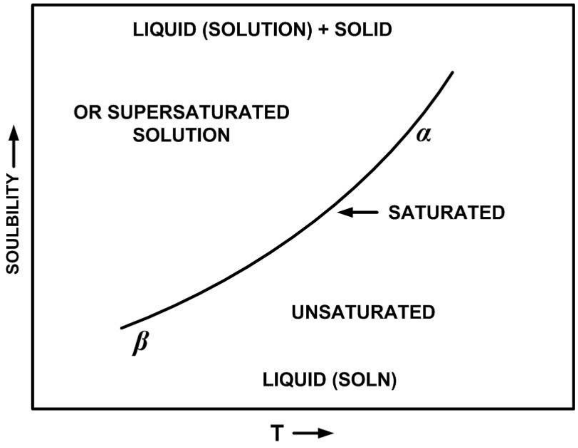

Figure 2.2.1: Solubility curve as a function of temperature [32].

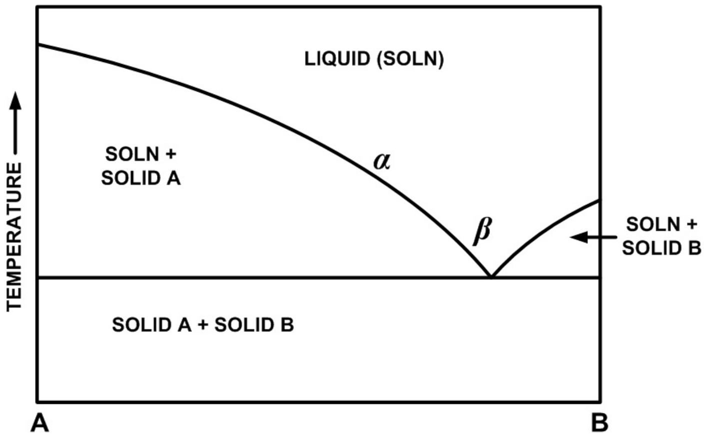

Figure 2.2.2: Binary phase diagram showing region for solution growth [32].

composition of the solution will change. Once the system reaches a eutectic region or some other phase then the solute can no longer crystallizes solely, so before that region the growth has to be stopped to get the pure solute crystal [32]. Fig 2.2.2 shows a typical binary phase diagram, here it is clearly shown the region for the solution growth i.e following the line from α towards β. Compound A is the one to be grown as a single crystal, and there is no compound inbetween A and B, as shown in the Fig 2.2.2. The eutectic phase which is a mixture of A and B, crystallizes at lower temperatures. Now by following the solubility line from α towards β by lowering the temperature, single crystals of A can be grown until the eutectic point as shown in Fig 2.2.2.

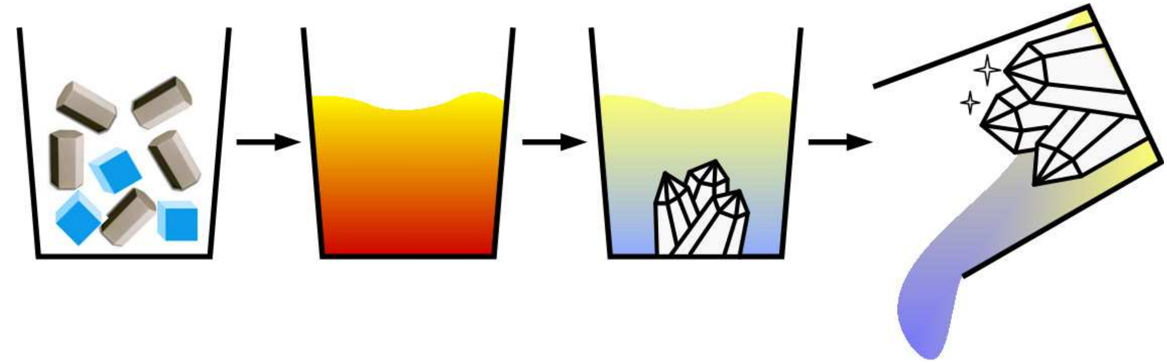

Figure 2.2.3: Schematic illustration of the solution growth technique.

Fig 2.2.3 shows a simple illustration of the solution growth technique to grow single crystals. Compound A and B are mixed together in an appropriate molar ratio, compound A is the solute which has to be grown as single crystal where as compound B is the solvent. A simple example is a mixture of salt and water, where salt is the solute and water the solvent. The salt is dissolved in hot water so that a homogeneous supersaturated solution is achieved. If the solution is, after sometime slowly cooled, large salt crystals will grow. Finally the excess water will be removed e.g., by decanting to collect the large salt crystals. In Fig 2.2.2 compound A is a salt and compound B is water, melting them together to make a supersaturated solution and lower the temperature slowly in a well controlled way to grow the crystals of A, and remove the excess of B as illustrated in Fig 2.2.3. The size of the crystals depends upon the cooling rate and the growth window i.e the region between the melting point and the eutectic point. The details of the growth for different compounds of Fe-based materials are found in the corresponding chapters.

2.3 X-ray diffraction

A structural characterization of the crystals e.g. including crystallographic structure, lattice parameters and phase purity is necessary prior to any further investigations. X-ray diffraction experiments were performed using a Rigaku Miniflex diffractometer (CuK_α radiation). In the case of powder diffraction measurements, single crystals were ground into fine powder using an agate mortar. In some cases Si is used as a internal standard to estimate the instrumental zero shift. X-ray measurements were also carried out on platelet like single crystals. In case of LiFeAs, x-ray measurement was carried out on the crystal-plane which was immersed in fomblin oil to protect from the air moisture.

2.4 Energy dispersive X-ray spectroscopy

SEM measurements were performed by S. Pichl. It is essential to carry out elemental analysis on the crystals, especially when the crystals are grown out of flux. It is very important to measure the real composition of the crystals, often there will be some difference between the nominal composition to that of achieved composition after the growth. Energy dispersive X-ray spectroscopy (EDX) is an analytical technique for the chemical analysis of the samples. In this work, several samples of each growth were examined with a Scanning Electron Microscope (SEMPhilips XL 30) equipped with electron microprobe analyzer for semi-quantitative elemental analysis using energy dispersive X-ray (EDX) mode. In this technique, an electron beam is incident on the surface of the sample which will interact with the sample, and inturn releases characteristic x-ray energy. In EDX, the energy and number of emitted x-rays are measured, from the intensities of the energy, qualitative analysis can be carried out. Images with the SEM were taken either with secondary electrons (low energies) or with the backscattered electrons (high energies). The backscattered electron image allows to detect the contrast between the regions with different compositions. Specifically the composition was estimated using EDX by averaging over several different points of platelet like single crystals. The EDX was measured on the same pieces, which were further investigated by magnetic susceptibility and resistivity.

2.5 Inductively coupled plasma spectroscopy

Estimating the composition from EDX is not possible for the lighter elements like Li, as lighter elemets are weak interacting to x-rays. Inductively coupled plasma spectroscopy is another powerfull analytical technique for the chemical analysis in which one can also estimate the composition for the lighter elements like Li. Inductively Coupled Plasma-Optical Emission Spectroscopy (ICPOES), is a type of emission spectroscopy that uses the inductively coupled plasma to produce excited atoms and ions that emit electromagnetic radiation at wavelengths characteristic of a particular element [33]. At first, ICPOES requires a solution of the material under study, secondly it is also necessary to calibrate the instrument by using a set of standard solutions of known concentration for each element to be determined. Therefore 2 sets of solution from each crystal growth batch were preapared. In a standard empty beaker with the known empty mass, 15 mg of single crystals were dissolved in 3ml of HNO_3 at about 100^0C. After dissolving the crystals, H_2O is added in to the beaker in such a way that the total weight of the solution becomes 300 g. From these sets of freshly prepared solutions, ICP analysis were carried out with ICAP 6500 Duo, Thermo Fisher Scientific GmbH with the standard solutions which were bought commercially for the elemental anlysis.

2.6 Magnetization measurements

Magnetization measurements were performed using a Magnetic Properties Measurement System (MPMS) and a Vibrating Sample Magnetometer (VSM) from Quantum Design. Before measuring the superconducting samples at low fields, the remanent field has been removed by applying 1 T and removing it by oscillatory mode. The absence of the remanent field gives the possibility to estimate the superconducting volume fraction more precisely. Zero-field-cooled (ZFC) and field-cooled (FC) magnetization measurements were carried out in a low field of 20 Oe from 1.8 K to 40 K with H||ab crystallographic directions. Normal state magnetization measurements were performed from 1.8 K to 300 K with an applied field of 1T with H||ab. In some cases data is collected with H||c to see the anisotropy.

2.7 Resistivity measurements

Temperature dependent resistivity was measured using a standard DC 4-probe technique. Electrical contacts parallel to the *ab*-plane were made using thin copper wires attached to the sample with silver epoxy. Resistivity measurements were performed on rectangular shaped samples cut out from large cleaved sections removed from the solidified ingot using a thin razor blade. The sizes of the resistivity specimens were typically between 2-4mm(length)*1-2mm(width)*200-500μm (thickness).

3 Unified phase diagram of $BaFe_2As_2$ single crystals

3.1 Introduction

The parent compound $BaFe_2As_2$ is an intermetallic compound which belongs to $ThCr_2Si_2$ structure-type [16]. The pristine $BaFe_2As_2$ compound undergoes a structural transition T_S from tetragonal to orthorhombic with a combined antiferromagnetic T_N spin density wave (SDW) transition at 140 K [16]. Superconductivity is achieved by suppressing this antiferromagnetic ordering, which is possible through several ways. One way of introducing superconductivity is by replacing divalent Ba^{2+} ions with a monovalent K^+ ions which is usually discussed interms of hole doping. Rotter *et al*. were the first to report superconductivity in K-doped $BaFe_2As_2$ with the highest T_c of 38 K [34]. Another way of inducing superconductivity in $BaFe_2As_2$ is by substituting Fe^{2+} by Co^{2+} ions. Sefat *et al*.[35] were the first to realize this type of Co-substitution in $BaFe_2As_2$ and they found superconductivity with T_c up to 22 K. Application of external pressure also leads to the bulk superconductivity in $BaFe_2As_2$ with T_c up to 18 K with an applied pressure of 11 GPa [36] which results in shrinking of the lattice. It is also possible to achieve superconductivity by substitution of isovalent P in As atoms in $BaFe_2As_2$ which

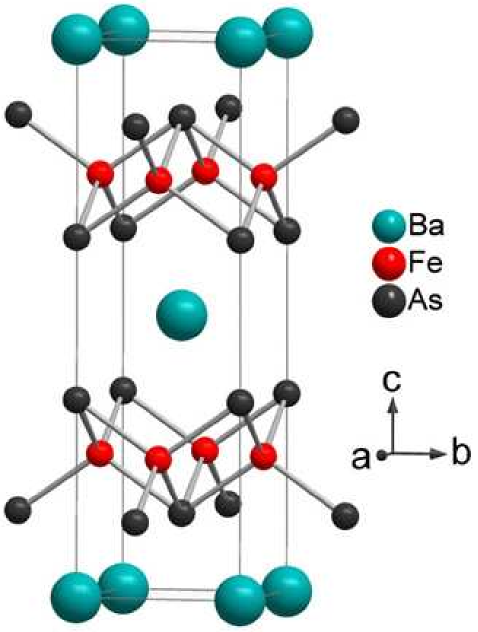

Figure 3.1.1: Crystal structure of $BaFe_2As_2$ which is a $ThCr_2Si_2$-type structure, space group I4mmm [34].

leads to superconductivity with a maximum T_c of 31 K [37]. The quest for new superconducting materials goes on and many new superconducting materials with different critical temperatures have been synthesized within the 122 series. Cortes-Gil *et al.* [38] reported superconductivity in polycrystalline samples of Na-doped $BaFe_2As_2$ which is analogous to that of K-doping. Here in this chapter I will present a systematic study of crystal growth, characterization and physical properties of two different chemical substitutions in $BaFe_2As_2$, namely (1) $Ba(Fe_{1-x}Co_x)_2As_2$ and (2) $Ba_{1-x}Na_xFe_2As_2$ and finally a unified phase diagram in $BaFe_2As_2$ will be derived for both types of substitutions.

3.2 $Ba(Fe_{1-x}Co_x)_2As_2$

3.2.1 Crystal growth

Parts of the following work were published in Journal of Crystal Growth [39] and the crystals discussed here were used for the studies using neutrons [40].

Self-flux technique(SFT)

A muffle-furnace from Nabertherm (inner-dimensions, $\approx 150 * 150 * 150 mm^3$) employing 6 u-shaped molybdenum-disilicide heating elements (3 elements uniformly spaced on each of the two side-walls) was used for the crystal growth experiments. In this furnace there is a large region ($\approx$ 90*90*90 mm^3) of fairly uniform temperature distribution around the geometric centre. Upon moving outside this region, the temperature tends to decrease or increase gradually depending on the position of the concerned point with respect to the heating elements. In particular, close to the midpoint of the front or rear walls of the furnace, which are devoid of heating elements, temperature is lower by about 20-25 K. In our experiments, the ampoule was placed along the line joining midpoint of the front and the rear wall of the furnace, tilted at an angle varying from 30^0 to 45^0 with respect to a horizontal line. By doing so the melt was expected to be in the temperature gradient of the furnace (depending upon the tilt angle the gradient may change slightly). In order to ensure that the melt experiences the same temperature gradient as in the furnace, the quartz ampoule was placed in a double-wall crucible assembly consisting of two thick coaxial alumina tubes, as shown schematically in Fig 3.2.1. Thick coaxial insulation of large thermal mass prevents small temperature fluctuations and radial heat losses during the growth process.

The precursor materials (see section 2.1) were weighed according to the composition

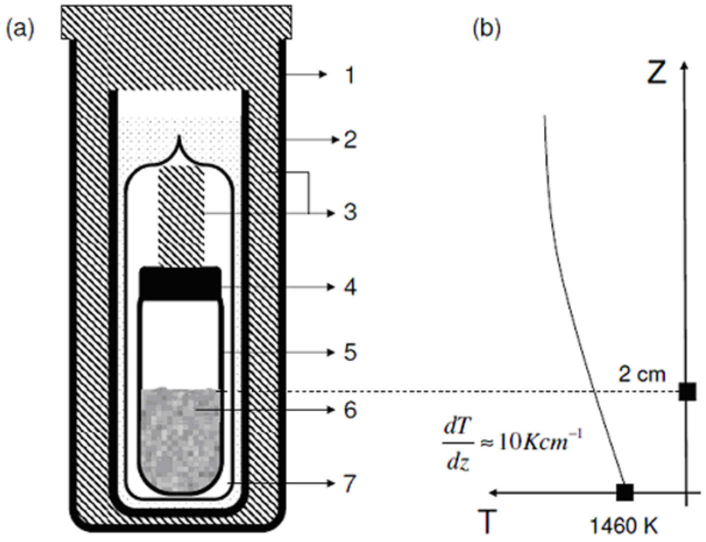

Figure 3.2.1: (a) Double-wall crucible assembly: (1) outer-alumina-shield, (2) inner- alumina-shield, (3) alumina-wool, (4) alumina lid, (5) alumina crucible, (6) molten charge, (7) Silica ampoule. (b) Temperature gradient over the length of the crucible [39].

$Ba(Fe_{1-x}Co_x)_{3.1}As_{3.1}$ and thoroughly mixed using a mortar and a pestle. The mixture, weighing about 5 g, was placed into an alumina crucible (ϕ_{in}=10 mm) which was introduced in a silica ampule (ϕ_{in}=16 mm, wall-thickness 2 mm). A thick alumina lid was placed on the crucible to prevent radiation heat loss from the molten charge (see Fig 3.2.1). Finally some quartz-wool was brought in from top to fill-up the remaining space. The ampoule was then sealed under a partial Argon pressure ranging from $\approx 10^{-5}$ mbar to about 200 mbar and introduced in the double-wall alumina housing. The entire crucible assembly as shown in Fig. 3.2.1 was then introduced in the furnace as described before. The furnace was heated up to 1463 K at 100 K/h with two intermediate dwellings of 3 h each at 1073 and 1303 K. The highest temperature was maintained for 12 h to allow for the homogenization of the melt, after which a slow-cooling at 2 K/h was initiated. The slow-cooling was terminated at 1248 K, this temperature was maintained for 1 h to allow stabilization of thermal equilibrium, after which the furnace

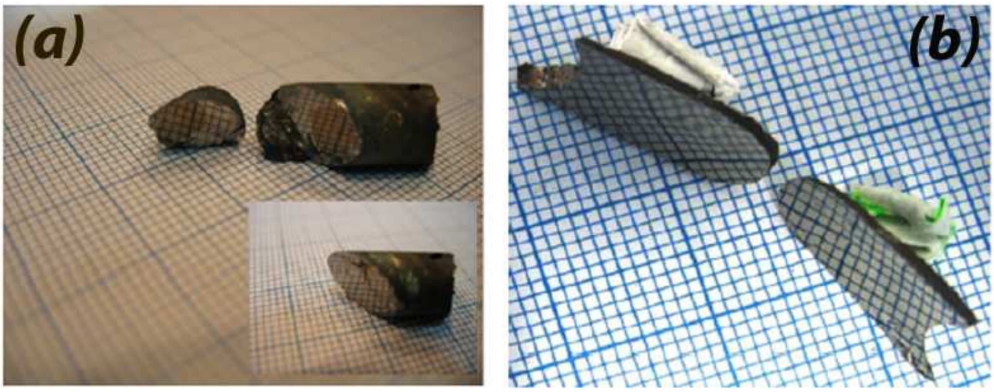

Figure 3.2.2: (a) Ba(Fe$_{0.9}$Co$_{0.1}$)$_2$As$_2$ (b) BaFe$_2$As$_2$. Inset in (a) shows a parallel cleaved surface at 2 mm from the cleavage plane in main panel.

was set to cool down to room temperature at a rate of 300 K/h. Due to the specific design features of our experimental set-up (Fig. 3.2.1), a situation analogous to the case of directional-solidification of a melt under a temperature gradient can be achieved. After the slow cooling with 2 K/h was initiated, the temperature of the bottom will reach first the liquidus temperature, where the seeding takes place. Upon further slow cooling more Ba(Fe$_{1-x}$Co$_x$)$_2$As$_2$ will solidify from the melt and the composition of the melt will continuously enrich itself with (Fe,Co)As; as commanded by the pseudo-binary BaFe$_2$As$_2$-FeAs phase diagram (Fig.3 of Ref.[41]). Thus, under the present experimental conditions, it is possible to obtain relatively flux-free single crystals at the bottom end of the crucible while the residual flux will go accumulating in the melt making it more and more (Fe,Co)As rich. Single crystals grown by this technique are shown in Fig 3.2.2(a) and (b). The shiny facets in these pictures are large cleavage planes whose boundaries are defined by the walls of the crucible. The inset of Fig 3.2.2(a) shows the same crystals in the main panel after cleaving further at 2mm, which clearly demonstrate that the solid-liquid interface during the growth experiment moves steadily analogous to the case of directional solidification of a melt. It was found that, the crystals grown under high-vacuum condition (Fig 3.2.2(a)) cleave at an angle of about 45^0 with respect to the crucible-axis, while those grown under 200 mbar of argon gas pressure (Fig 3.2.2(b)) cleave at even higher angles, in some case almost parallel to the crucible axis. It is possible that the shape profiles of the temperature isotherms, as seen by the melt, differ in the two cases depending on the pressure of the exchange gas inside the ampoule.

3.2.2 Characterization

The quality of the grown single crystals was assessed by several complementary techniques. From each batch, several samples were examined with SEM in EDX mode. The Co composition was estimated using EDX by averaging over several different points of the corresponding platelet-like single crystals. The Co composition estimated by EDX is quite comparable to the nominal composition for all Ba(Fe$_{1-x}$Co$_x$)$_2$As$_2$ single crystals, the estimated EDX values are listed in Table 3.2.1. Fig 3.2.3(a)(b) shows the SEM pictures of Ba(Fe$_{0.95}$Co$_{0.05}$)$_2$As$_2$ and BaFe$_2$As$_2$. These crystals grow as layered structures that are easy to cleave along the ab-plane. Fig 3.2.3(c)(d) gives an exaggerated view of the layered morphology, which depicts the layer-by-layer growth behavior of these compounds.

Lattice parameters were determined using powder x-ray diffraction, with Si as internal standard. For this purpose small pieces of single crystals from each batch were ground into fine powder. The lattice parameters of all the grown crystals are plotted in Fig 3.2.4. Upon Co-doping, the c-parameter decreases strongly but the a-parameter shows only a marginal increase, resulting in an overall decrease of the unit cell volume. All the data are in good agreement with the reported data in the literature [42].

3.2.3 Resistivity measurements

Data from G. Friemel [43]. A systematic decrease of the room temperature resistiv-

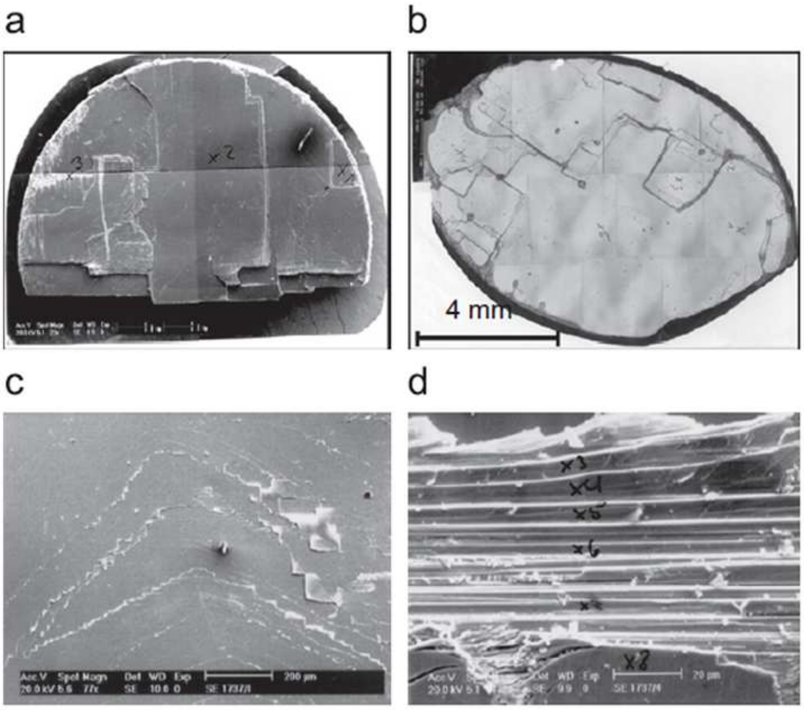

Figure 3.2.3: SEM images of single crystals grown using the self-flux technique: large cleaved sections of: (a) Ba(Fe$_{0.95}$Co$_{0.05}$)$_2$As$_2$ (b) BaFe$_2$As$_2$ (c) and (d) show the layer by layer growth of these single crystals and a tendency towards exfoliation owing to the layered structure

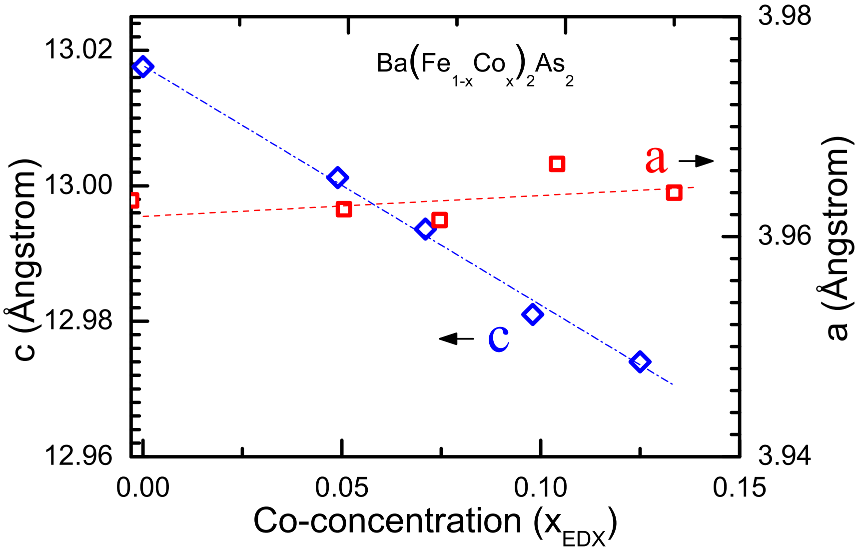

Figure 3.2.4: Lattice parameters of Ba(Fe$_{1-x}$Co$_x$)$_2$As$_2$ single crystals grown using self-flux.

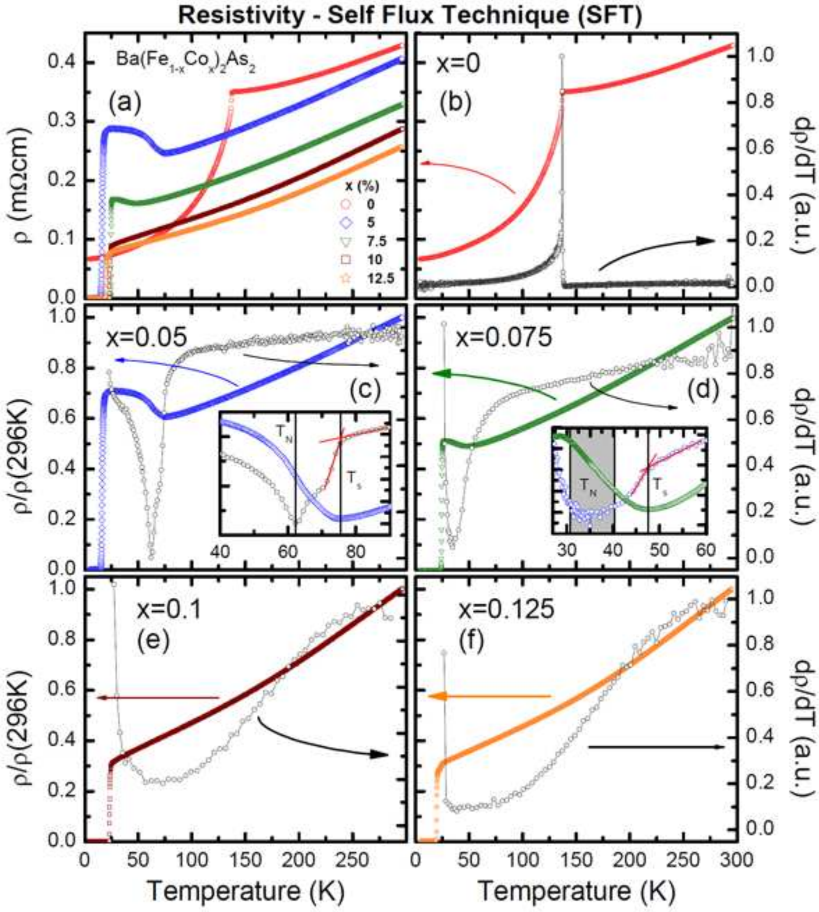

Figure 3.2.5: Temperature dependent resistivity ρ(T) of $Ba(Fe_{1-x}Co_x)_2As_2$ single crystals grown using the self-flux technique: Panel (a) shows ρ(T) of all samples. Panels (b) to (f) compare ρ(T) (normalized to room temperature) with the derivatives of ρ(T) versus temperature. The insets in panels (c) and (d) illustrate how the transition temperatures T_S and T_N have been extracted from the data. [resistivity measurements from G. Friemel] [39]

ity with increasing Co-doping can be observed. The sharp drop of ρ(T) observed in the pristine compound BaFe$_2$As$_2$ Fig 3.2.5(b) marks the onset of the combined structural/magnetic transition at T$_0$=T$_{S/N}$=137 K. The value of T$_0$ for the crystals grown from SFT (determined from the derivative plot as depicted in Fig 3.2.5)(c) is in good agreement with other recently reported values for self-flux grown single crystals [44, 42, 45]. The residual resistivity ratio (RRR= ρ(300 K)/ρ(5 K)) is 5.1 is significantly larger as compared to the values reported in literature [44, 46, 45, 47], which is usually interpreted as the signature of better quality of single crystals. The conclusion of a higher crystal quality from a higher RRR is very ambiguous for the present case of a SDW ordering compound, where parts of the Fermi surface are gapped in the SDW state. The actual value of the resistivity at low temperature in this case depends in a very subtle manner on the balance of a reduced carrier density (caused by the gap) and an enhanced carrier mean free path (due to reduced scattering) both of which depend differently on the sample purity. Upon Co-doping the structural/magnetic transition splits into two separate transitions [48] which completely alters the temperature dependence of the resistivity. Unlike the parent compound and the well documented case of LaO$_{1-x}$F$_x$FeAs, where the resistivity exhibits a strong downwards decrease at T$_0$,T$_S$ [49, 50], the resistivity shows a jump-like increase below the structural transition temperature. This behavior is most pronounced at the x=0.05 doping level as shown in Fig 3.2.5(c), which also shows the derivative dρ/dT.

Following the analysis described in Ref.[46] T$_S$=76 K is extracted from strong change of slope and T$_N$=62 K from the inflection point of the resistivity [48]. The upper anomaly is attributed to the structural transition and the lower one to the magnetic transition. The sample also shows a sudden drop of the resistivity below approximately 18 K due to onset of superconductivity. T$_c$ from the resistivity curve, T$_c{}^\rho$ (determined using the midpoint criteria, i.e., the temperature where resistivity has dropped to 50% of its normal state value), is estimated to be 16.3K. At x=0.075 (x_{EDX}=0.071) Co-substitution Fig 3.2.5(d), the transitions have shifted towards lower temperatures and apparently broadened, where the structural transition can be better resolved (T_S=47 K) than the magnetic one, which possibly occurs in the range 30-40 K (shaded area in the inset of Fig. 5d). $T_c{}^\rho$ for this sample is about 24.5 K. For the samples at the x=0.1 and 0.125 doping levels (see panels (e) and (f) in Fig 3.2.5), there is no indication of structural or magnetic transition from the resistivity data and the superconducting transition temperatures are found out to be $T_C{}^\rho$=23.7 K, and $T_c{}^\rho$=20 K, respectively [For x=0.125, we observe the signature of the onset of spurious superconductivity already at about 24K]. In addition, the estimated width of the transition $\Delta T_c{}^\rho$ for these single crystals using: $\Delta T_c{}^\rho$=[T(90)T(10)%], where T (α%) is the temperature, where ρ(T) is α% of its normal state value. We find $\Delta T_c{}^\rho$ = 0.6-0.7 K for the optimally doped samples (x=0.1) close to earlier reported values [15,22] and $\Delta T_c{}^\rho$=0.9 for x=0.125. At higher temperatures ρ of both samples exhibits a monotonically increasing behavior as a function of increasing temperature. The values of T_c, ΔT_c, structural (T_S) and magnetic transition temperature (T_N) of these crystals are presented in Table 3.2.1

3.2.4 Magnetization measurements

Susceptibility measured with applied field of 1T parallel to *ab* plane for the pristine $BaFe_2As_2$ is shown in Fig 3.2.6(a). The susceptibility is linear as a function of temperature until it reaches the combined structural T_S and magnetic T_N transition at T_0=137 K, which is inline with the resistivity data (3.2.3). Fig 3.2.6(b) shows the anisotropic behaviour of the parent compound $BaFe_2As_2$ from susceptibility measured along parallel to crystallographic *ab* and *c* axes with an applied field of 6 T. The susceptibility in the $BaFe_2As_2$ is always higher along H$||ab$ plane. The upturn in the susceptibility at low temperatures below 25 K, which may arise due to the curie tail effect similar to [44], is well pronounced in 1 T curve but suppressed with an applied field of 6 T (Fig 3.2.6(a)(b)).

Low field magnetization measurements have been performed after cooling the samples in zero (ZFC) and applied (FC) magnetic field from far above the critical temperature. Fig 3.2.7 presents the temperature dependence of the volume susceptibility (χ_{vol}) measured with an applied field of 20 Oe $||ab$. χ has been deduced from the measured magnetization and is not corrected for demagnetization effects. The T_c was determined from the bifurcation point between ZFC and FC magnetization and Table 3.2.1 summarizes the results. For the optimally doped samples, T_c values estimated from the susceptibility data are in good agreement with those from the resistivity data as shown in Table 3.2.1. The crystals presented in this work $Ba(Fe_{1-x}Co_x)_2As_2$ with x = 0.05 (underdoped), $T^{\rho}{}_c$ exceeds $T^{\chi}{}_c$ by 3 K and also with x = 0.125 (overdoped) there is a considerable difference of 2 K. It is noted that even the transition widths in both resistivity and susceptibility data are relatively broad. Apparently, this feature is not unique to the crystals presented in this work, as broad transitions in underdoped samples have also been reported previously [42, 51, 52]. The first speculation would be chemical inhomogeneity as explanation, for such a broadening in the underdoped region. However, NMR studies disregarded such a scenario of chemical inhomogeneity (see Refs. [53, 54]). The broad transition widths could be the intrinsic property for underdoped and overdoped region.

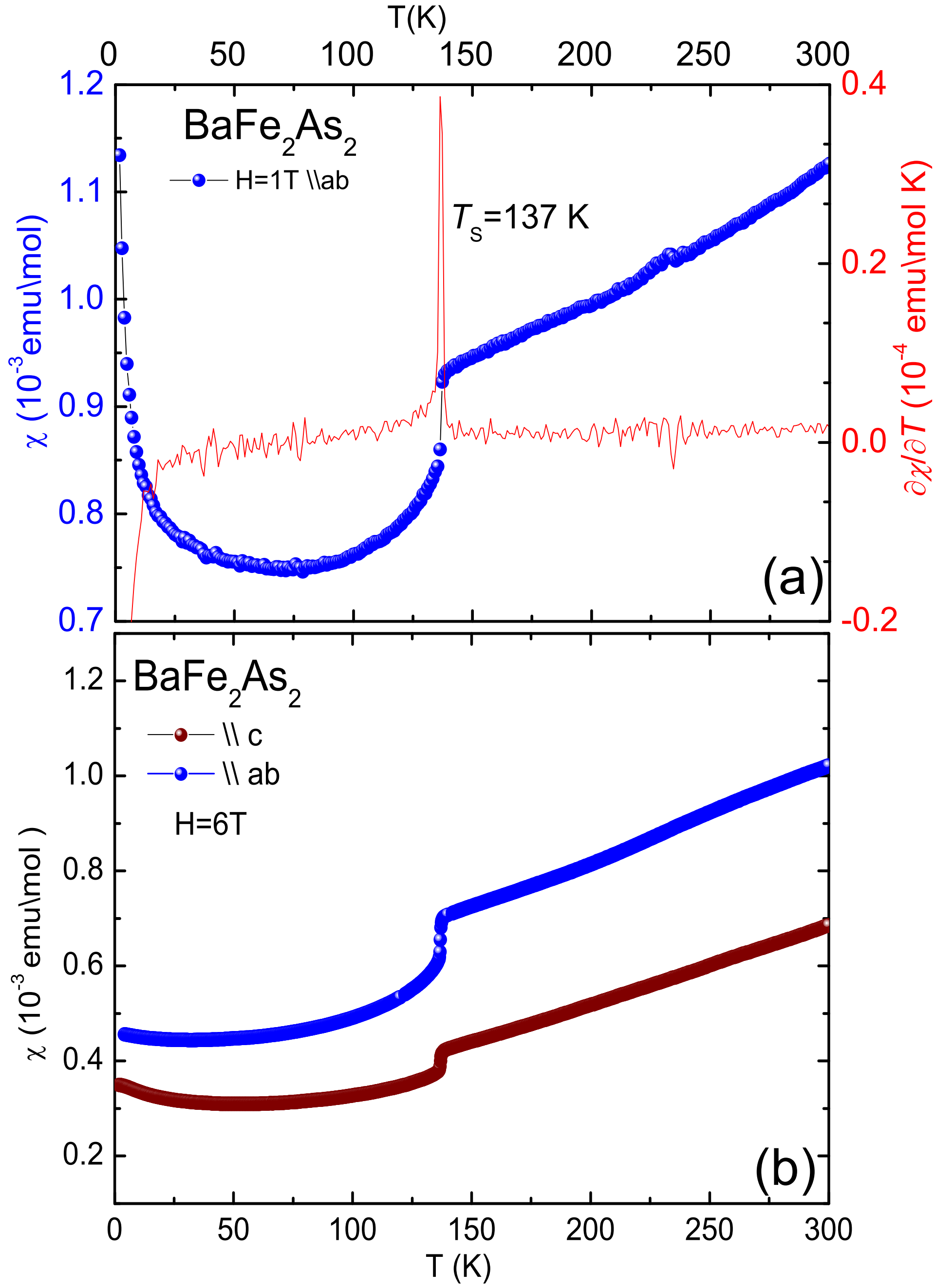

Figure 3.2.6: Temperature dependent susceptibility $\chi(T)$ of $BaFe_2As_2$ single crystals. (a) Susceptibility measured at an applied field of $1T \| ab$ plane. (b) Susceptibility measured at an applied field of $6T \| ab$ and $\| c$ planes.

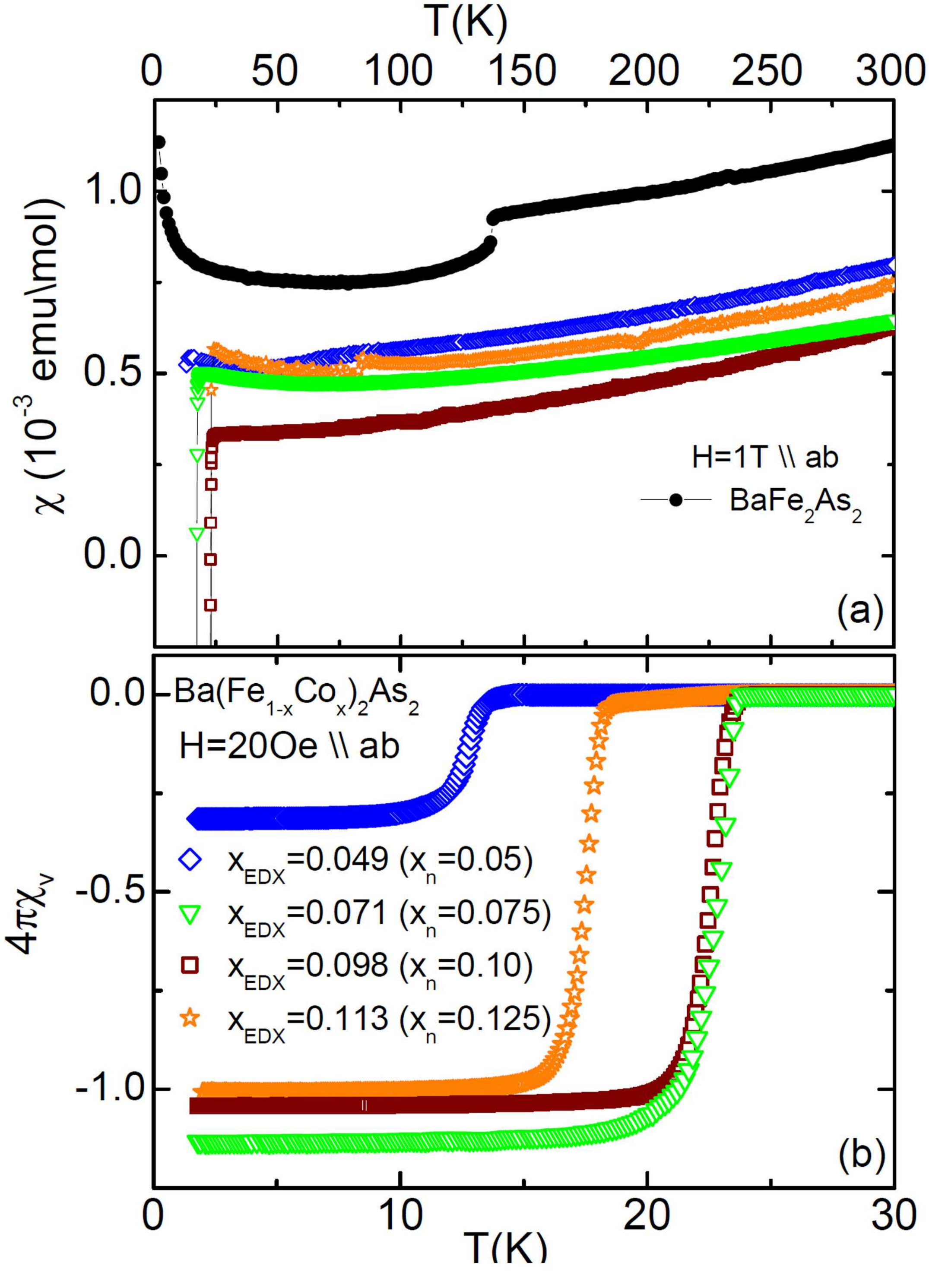

Figure 3.2.7: (a) Susceptibility χ = M/B for $Ba(Fe_{1-x}Co_x)_2As_2$ for different doping levels at H$\|ab$ = 1 T. (b) Temperature dependent volume susceptibility of superconducting $Ba(Fe_{1-x}Co_x)_2As_2$ single crystals.

Table 3.2.1: Physical properties of $Ba(Fe_{1-x}Co_x)_2As_2$ single crystals.

$x_{Nominal}$	x_{EDX}	T_S(K)	T_N(K)	T_c^{χ}(K)	T_c^{ρ}(K)	$\Delta\ T_c\ ^{\rho}$(K)
0.0	0	137	137	[a]	[a]	[a]
0.05	0.049	76	62	13.5	16.3	2
0.075	0.071	45	[a]	23.8	24.5	0.7
0.10	0.098	[a]	[a]	23.5	23.7	0.65
0.125	0.113	[a]	[a]	18	20	2

[a] absent

3.2.5 Ac susceptibility measurements

Ac susceptibility measurements were performed and analysed by G. Prando and M. Abdel-Hafiez [55]. The purity and the quality of the single crystals often play crucial role while investigating intrinsic properties of materials. The crystals grown from the optimized self-flux technique as explained in section 3.2.1 not only yeilded large size flux free crystals but also of the excellent quality. Ac susceptibility measurements were performed on one of the optimally doped single crystal of $Ba(Fe_{0.9}Co_{0.1})_2As_2$ with the T_c = 23.5 K, for the investigation of vortex physics in these materials. The width and the sharpness of the superconducting transition T_c obtained from the measurement shows the exceptionally high quality of the single crystal as shown in Fig 3.2.8 [55]. The high quality of the investigated single crystal allowed the detection of dynamical-scaling as reported in [55].

3.2.6 Summary and conclusions

In summary, single crystals of $Ba(Fe_{1-x}Co_x)_2As_2$ with $x = 0$, 0.05, 0.075, 0.10 and 0.125 were grown using a self-flux method. The superconducting and normal state properties have been systematically studied by means of temperature dependent magnetic sus-

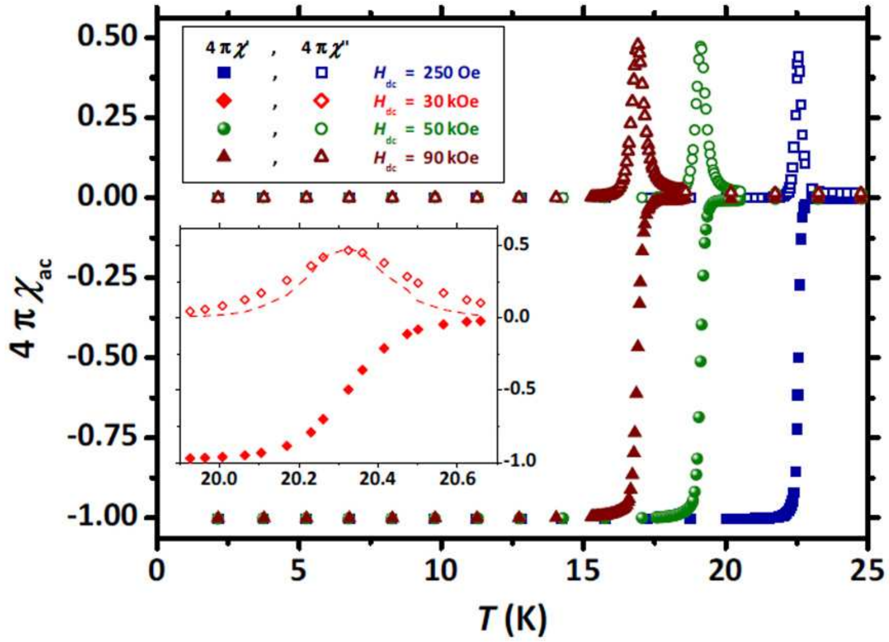

Figure 3.2.8: χ_{ac} vs. Temperature for both real and imaginary components at ν_m = 9685 Hz and at different H$_{dc}$. Inset: zoom for H$_{dc}$ = 30 kOe around the step-like drop of the real component. The dashed line represents the derivative of the χ'_{ac} with respect to T [55].

ceptibility and electrical resistivity. Substitution of Co by Fe leads to the suppression of SDW ordering and induces superconductivity up to 25 K for x=0.1. The temperature of the phase transitions discussed above, T$_c$, T$_S$ and T$_N$, for the single crystals of Ba(Fe$_{1-x}$Co$_x$)$_2$As$_2$ are plotted in Fig 3.2.9 to map out a substitution dependent electronic phase diagram. In the overdoped regime, the superconducting transition temperature T$_c$ is about 5 K higher compared to the phase diagrams published by Lester et al.[48] and Ni et al.[42]. This observation cannot be explained by taking into account an error bar of about 0.5-1% in the Co-concentration stemming from the EDX measurements. On the other hand, this data show a good agreement in the entire Co-concentration range with the results of Chu et al.[51]. An overall agreement between these independently obtained data sets can be readily seen, indicating the reproducibility of the electronic phase diagram of Ba(Fe$_{1-x}$Co$_x$)$_2$As$_2$ superconductors. All these results of Ba(Fe$_{1-x}$Co$_x$)$_2$As$_2$ have been summerized in Ref [39].

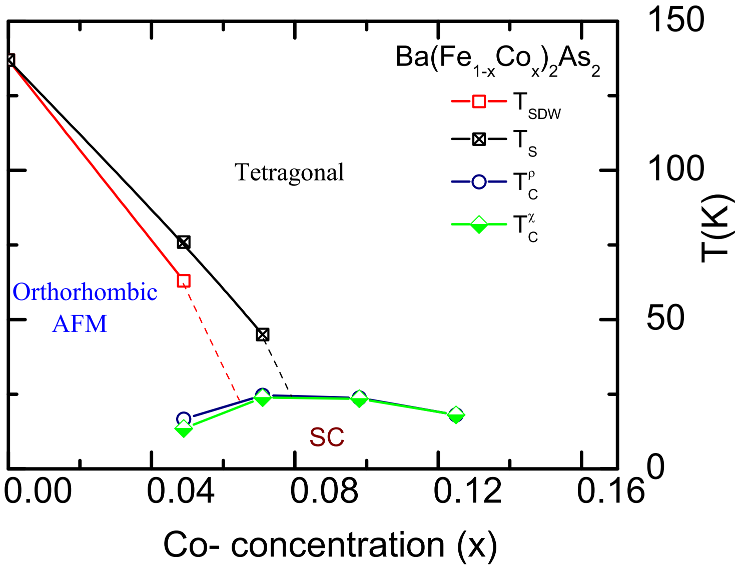

Figure 3.2.9: Evolution of structural T_S, magnetic T_N, and superconducting T_c, transition temperatures as a function of Co-concentration (x) obtained using EDX in $Ba(Fe_{1-x}Co_x)_2As_2$ single crystal.

3.3 $Ba_{1-x}Na_xFe_2As_2$

Parts of the work shown in this chapter were published in Phys. Rev. B [56], the same crystals were also used for calorimetric investigation [57].

3.3.1 Crystal growth

Prior to the crystal growth the starting precursor materials were prepared (see section 2.1). These precursor materials were used as a starting materials. According to the desired stoichiometry $(Ba_{1-x}Na_x)$:Fe:As were used in a molar ratio of 1:4:4. The corresponding Na was used in its metallic form and was placed at the bottom of the alumina crucible, while the well ground mixture of the pre-reacted pnictide material was carefully placed on top. The alumina crucible was then put into a niobium container which was sealed under 0.5 atm pressure of Argon in arc-melting facility. The sealed niobium

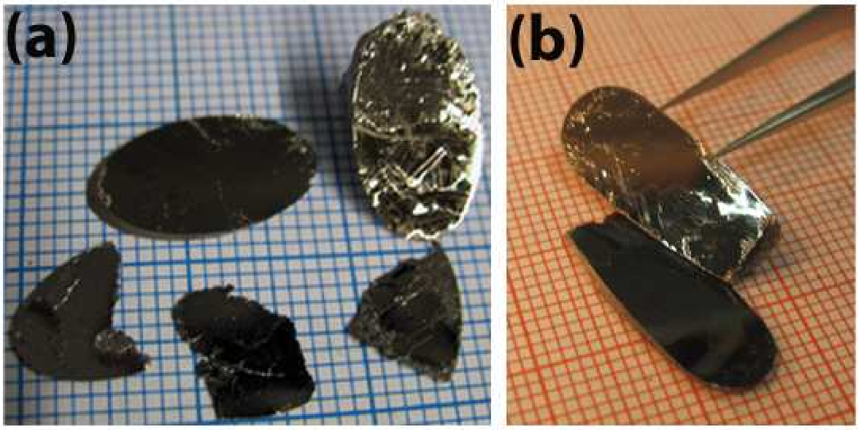

Figure 3.3.1: (a) As grown plate-like single crystals of $Ba_{0.65}Na_{0.35}Fe_2As_2$ (b) Freshly cleaved single crystals of $Ba_{0.75}Na_{0.25}Fe_2As_2$.

crucible assembly was placed in vertical furnace with Ar atmosphere. The furnace was heated up to 1373 K with a rate of 100 K/h where it remained for 10 hours to ensure homogenous melting and afterwards cooled down to 1023 K with a rate of 2 K/h. Finally the furnace was cooled to room temperature with 300 K/h. Platelet-like single crystals of cm-size were obtained as demonstrated by Fig 3.3.1(a),(b). The surfaces of the crystals are shiny and metallic-like (see Fig 3.3.1(a),(b)). All crystals show layered morphology and are thus typically easy to cleave along the *ab* plane. These cleaving planes are shown in Fig 3.3.2(a-f).

3.3.2 Characterization

Elemental analysis were carried out using the energy dispersive x-ray (EDX) (see 2.4). The composition and in particular the Na-doping level was obtained by averaging over several different points of each single crystal. The corresponding compositions and standard deviations are x = 0.250 ± 0.005, x = 0.350 ± 0.01, and x = 0.400 ± 0.01. The homogenous distribution of Na, as reflected by the small SD, confirms the reasonable homogeneity of our crystals. Fig 3.3.2(a-e) exemplarily shows the SEM images of the

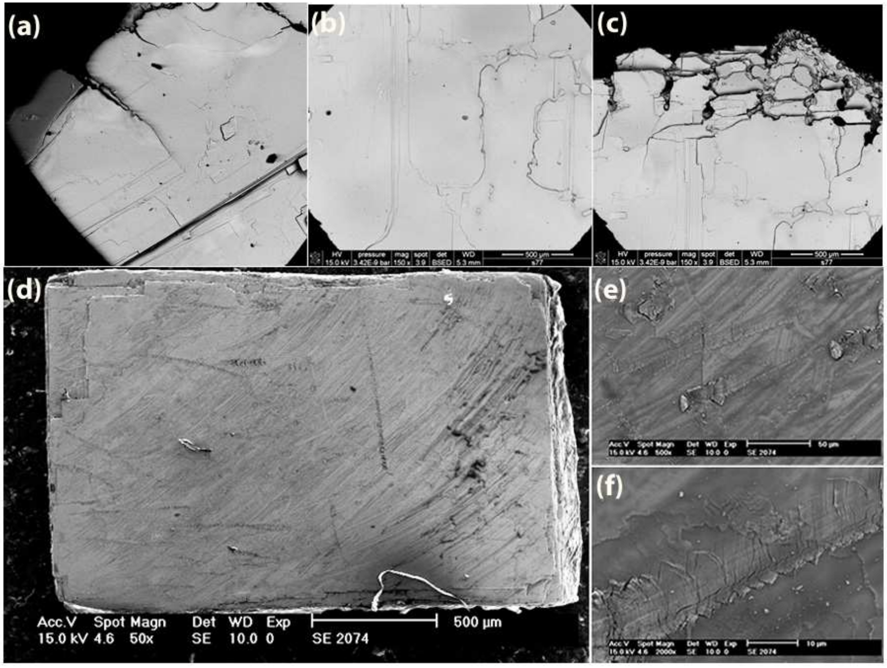

Figure 3.3.2: (a-c) SEM pictures of a $Ba_{0.75}Na_{0.25}Fe_2As_2$single crystal. (d-e) SEM pictures of the $Ba_{0.65}Na_{0.35}Fe_2As_2$ single crystal which shows the typical layer by layer growth.

single crystals with Na content of x = 0.25 and x = 0.35. The layer by layer growth can be easily seen here.

Fig 3.3.3 shows an x-ray diffraction pattern taken on plate-like single crystals with different Na-contents using a Rigaku miniflex with Cu-K_α-radiation. Only reflections with $00l$ Miller indices are observed, as expected for c-axis orientation. All the reflections are indexed based on the $ThCr_2Si_2$ structure-type, which confirms the phase purity of our $Ba_{1-x}Na_xFe_2As_2$ single crystals.

3.3.3 Magnetization measurements

Magnetization measurements have been performed after cooling the samples in zero (ZFC) and applied (FC) magnetic field from far above the critical temperature.

Fig 3.3.4(a) shows the molar susceptibility measured in an applied magnetic field of 1 T with $H||ab$. The susceptibility data of the parent compound clearly shows an anamoly

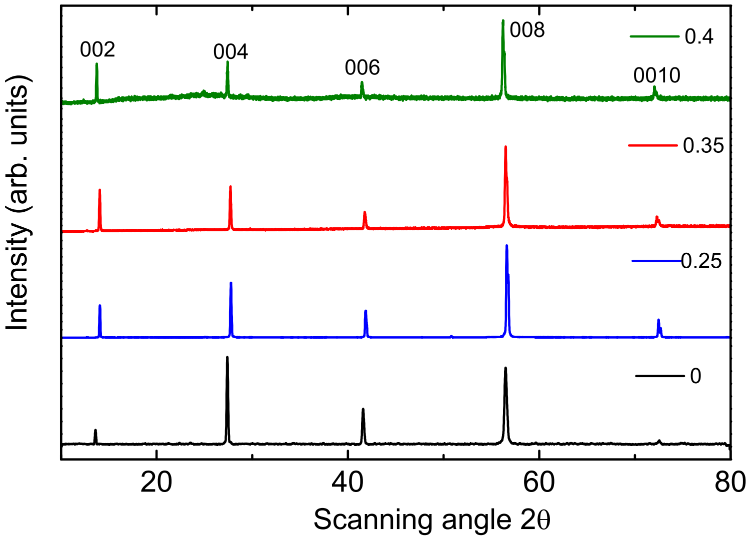

Figure 3.3.3: (a) XRD pattern of $Ba_{1-x}Na_xFe_2As_2$ showing only $00l$ reflections. The XRD data were collected using plate-like crystals.

at 137 K which corresponds to the combined structural (T_S) and magnetic (T_N) transition in $BaFe_2As_2$ (see e.g. [39] and section 3.2). This transition is clearly suppressed and shifted to lower temperatures upon the substitution of Ba by Na. Specifically, the T_S/T_N transition for $Ba_{0.75}Na_{0.25}Fe_2As_2$ occurs at 123 K. Moreover, this transition is also significantly broadened compared to the parent compound. The shift and broadening of the T_S/T_N transition is more apparent in the derivative of the static susceptibility (inset of Fig 3.3.4(a)). No indication of splitting of the structural and magnetic transition is observed. However, in case of a hole-doped $Ba_{0.86}K_{0.14}Fe_2As_2$ crystal in the underdoped regime grown from Sn flux, a clear splitting of T_S and T_N, monitored by distinct anomalies in both $d\rho/dT$ and specific heat, was reported by Urbano *et al.* [58]. In contrast to that Avci *et al.* found no splitting at all doping levels of polycrystalline $Ba_{1-x}K_xFe_2As_2$ where T_s and T_N co-exist [59]. Generally, samples grown from self-flux are considered to have a higher quality than those grown from Sn flux. As an example, Mathieu *et al.*

could show that Sn may even substitute Ba in $BaFe_2As_2$ [60]. Such difference in quality related to the different flux types might explain the absence/presence of the T_S and T_N splitting. At T=10 K , $Ba_{0.75}Na_{0.25}Fe_2As_2$ undergoes also a superconducting transition, which is a general feature of underdoped samples. Samples with higher Na-contents (x=0.35, 0.4) show no indication neither for a structural nor a magnetic transition, but a superconducting transition only. Interestingly, all samples show a linear temperature dependence of the susceptibility χ(T) (see Fig 3.3.4). The range of this linearity is from 300 K to about 150 K for samples exhibiting a structural and magnetic transition (x=0, 0.25) and 300 K to 50 K for samples with x=0.35, 0.4. This linearity of the susceptibility has already been discussed for undoped $BaFe_2As_2$ and both electron-doped $LaO_{1-x}F_xFeAs$ and $Ca(Fe_{1-x}Co_x)_2As_2$ [61, 44]. So it was concluded that this linearity is a general feature and that the normal state susceptibility is not affected by the type of charge carriers. Here, I will analyze the slope of the linear part of the magnetic susceptibility for the $Ba_{1-x}Na_xFe_2As_2$. The average slope of the susceptibility $d\chi/dT$ at high temperature is 8 $\times 10^{-7}$ erg/(G^2mol K) which is similiar to the value of the slope reported for the electron-doped $LaO_{1-x}F_xFeAs$ and $Ca(Fe_{1-x}Co_x)_2As_2$ [61]. However, the slope of the parent and underdoped compound is very similar (1×10^{-7} erg/(G^2mol K)) and decreases significantly for the samples with higher Na-contents (8×10^{-7} erg/(G^2molK) for x=0.35; 3×10^{-7} erg/(G^2molK) for x=0.4). One may conclude that the linearity in susceptibility is a characteristic property of Fe-based superconductors, but that the slope might differ for different types of charge carriers.

Fig 3.3.4(b) presents the temperature dependent volume susceptibility χ_{vol}. χ has been deduced from the measured magnetization and is not corrected for demagnetization effects. The sharp superconducting transition with a transition width of less than 2.5 K confirms the good quality of the crystals. T_c had been determined from the bifurcation

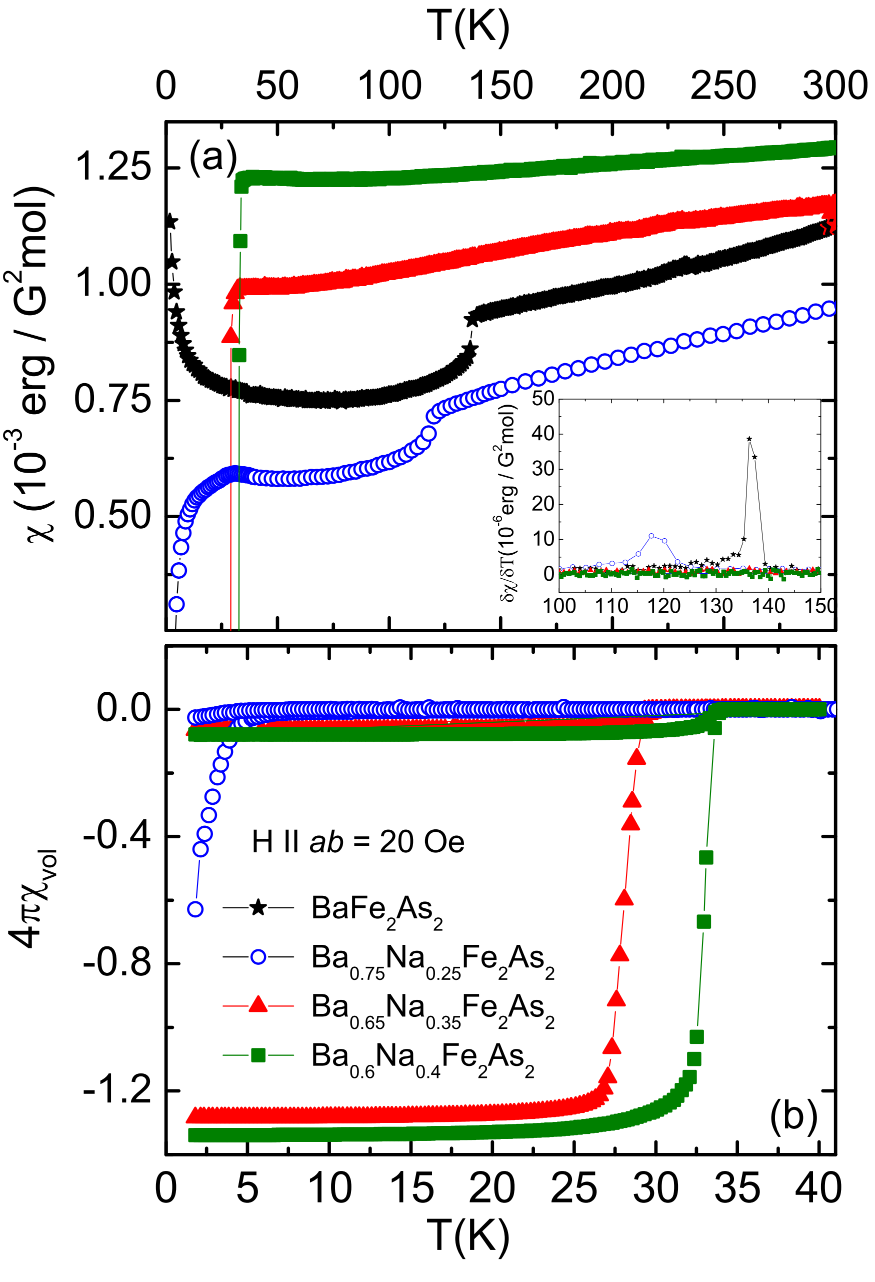

Figure 3.3.4: (a) Susceptibility χ = M/B for $Ba_{1-x}Na_xFe_2As_2$ for different doping levels at H$\|ab$ = 1 T. The inset shows the derivative of the static susceptibility. (b) Temperature dependence of the volume susceptibilty χ_{vol} following ZFC-FC protocol as described in the text, all data have been collected for B$\|$ ab and the applied field was 20 Oe.

point between the ZFC and FC magnetization. Using this approach, T_c was estimated to be 10 K, 29 K and 34 K for samples with $x = 0.25$, 0.35 and 0.4, respectively. The critical temperatures of the single crystals presented here are in good agreement with the ones observed for polycrystalline samples of Na-doped $BaFe_2As_2$ by Cortes-Gil *et al.* [38].

3.3.4 Resistivity measurements

Fig 3.3.5 shows the resistivity of all $Ba_{1-x}Na_xFe_2As_2$ single crystals [data from D. Bombor]. For the undoped and $x = 0.25$ samples the derivative of the resistivity (inset Fig 3.3.5) shows a clear maximum at $T_c(x = 0)$=137 K and $T_{S/N}(x = 0.25)$=117 K, typically found in hole-doped 122-compounds (see e.g. [62]) which is an indication of the structural and magnetic transition. Note that, here there is no indication of a doping induced splitting of this transition as observed in electron-doped 122-compounds [63, 64, 39]. The normal state resistivity decreases by 20% with doping, which is also observed in K-doped Ba122-compounds [62] in contrast to a decrease of 50 % for electron-doped samples [63, 64, 39]. The sample with ($x = 0.25$) shows both an antiferromagnetic and a superconducting transition which is typically seen in all underdoped 122-compounds [42, 39, 65]. In general, a transition towards superconductivity could be observed in all samples containing Na. The critical temperature was assigned where the resistivity drops to 50% of its value in normal state. Using this approach, superconductivity is found below $T_c(x = 0.25) = 9$ K, $T_c(x = 0.35) = 32$ K $T_c(x = 0.40) = 34$ K, which is in line with the T_c derived from magnetization measurements.

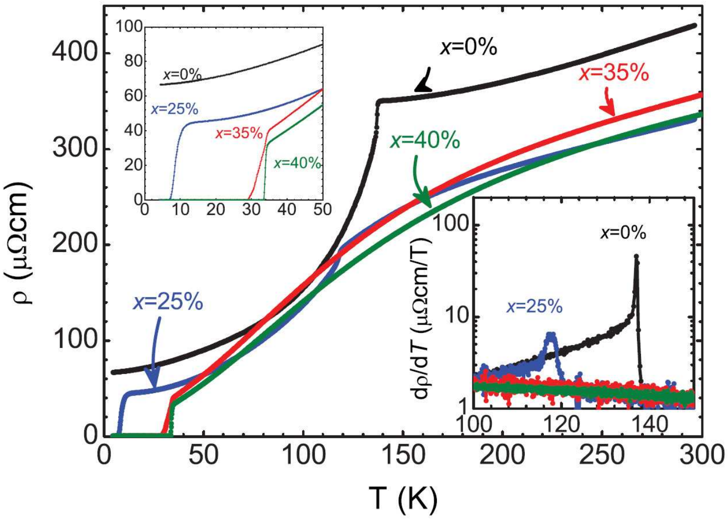

Figure 3.3.5: In-plane electronic resistivity ρ of $Ba_{1-x}Na_xFe_2As_2$ single crystals for different Na-contents x in dependence of the temperature. Inset: Derivative $d\rho/dT$ around the combined structural and magnetic transition. [data from D. Bombor]

3.3.5 Summary and conclusions

In summary, single crystals of $Ba_{1-x}Na_xFe_2As_2$ with $x = 0$, 0.25, 0.35, 0.40 were grown using a self-flux method. The superconducting and normal state properties have been systematically studied by means of temperature dependent magnetic susceptibility and electrical resistivity. Substitution of Ba by Na leads to the suppression of SDW ordering and induces superconductivity up to 34 K for x=0.4. The investigation of the electronic structure of the $Ba_{1-x}Na_xFe_2As_2$ single crystals by ARPES reveals striking similarities of the Fermi surface with the famous K- (hole)-doped sister compounds [56]. These results suggest a generic behaviour of the 122 series upon hole-doping. The temperature of the phase transitions discussed above, T_S, T_N and T_c, for the single crystals of $Ba_{1-x}Na_xFe_2As_2$ grown in the present work are plotted in Fig 3.3.6 to map out an electronic phase diagram. The data for single crystals from this work are in good agreement with the ones reported for in polycrystalline samples by Cortes-Gil *et al.* [38].

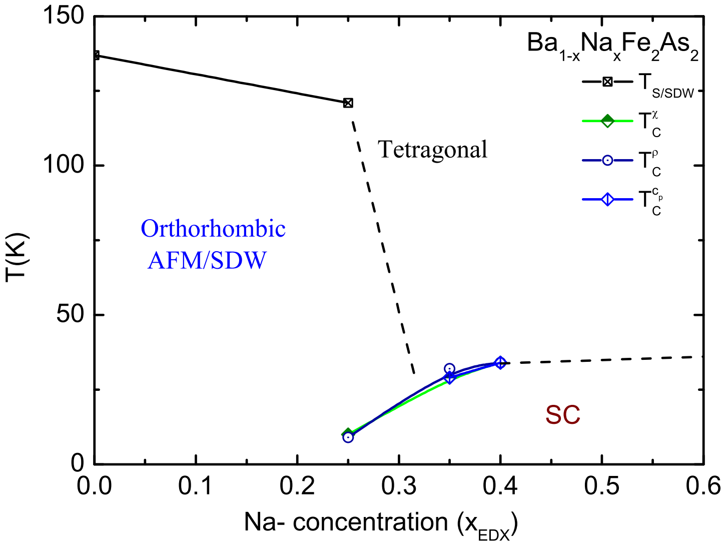

Figure 3.3.6: Evolution of structural T$_S$, magnetic T$_N$, and superconducting T$_c$, transition temperatures as a function of Na-concentration in Ba$_{1-x}$Na$_x$Fe$_2$As$_2$ single crystal.

3.4 Unified phase diagram

Unified phase diagram has been constructed for BaFe$_2$As$_2$ with electron, i.e., Ba(Fe$_{1-x}$Co$_x$)$_2$As$_2$ and hole doping, i.e., Ba$_{1-x}$Na$_x$Fe$_2$As$_2$ as shown in Fig 3.4.1. The dotted lines are guides for the eyes. A clear difference between hole and electron doped side is the splitting of the structural T$_S$ and magnetic phase transitions T$_N$ for underdoped compounds, while no splitting is observed for the hole doped side. On both sides of the phase diagram, the magnetic and superconducting regions overlap for underdoped samples. Whether there is co-existance or competition between magetic and superconducting phases is an ongoing debate and will be the subject of further studies. The phase diagram presented here is in good agreement with the other reported hole and electron doped in the BaFe$_2$As$_2$ system [22, 23, 38].

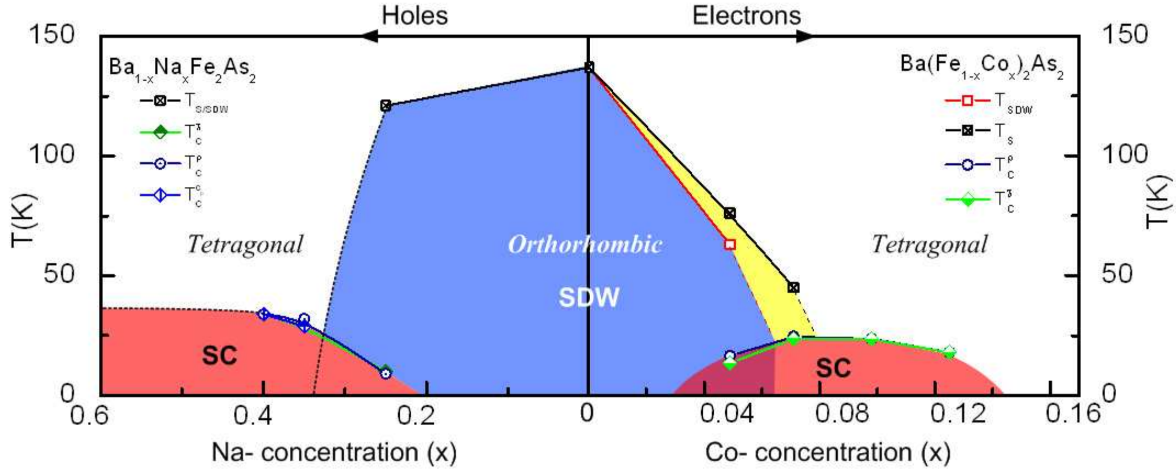

Figure 3.4.1: Unified phase diagram, showing structural, magnetic and superconducting regions of electron and hole doped regions in $BaFe_2As_2$ single crystals, dotted lines are guide line to eye.

4 Suppression of superconductivity with charge doping in LiFeAs

4.1 Introduction

In the field of superconductivity, LiFeAs has recently generated enormous pursuit among the researchers working with Fe-based superconductors [24]. Interestingly, one of the first publications on LiFeAs dates back to 1968 [66], though it did not attract much attention until the recent discovery of superconductivity in Fe-As compounds [9]. Among different types of Fe-based superconductors, LiFeAs has been found to be an unique representative. One reason is that the magnetically ordered spin density wave state, which is suppressed upon doping, and is considered to be obligatory for superconductivity in all Fe-As superconductors [13, 15, 51], is not present in LiFeAs even after the application of pressure up to 20 GPa [67]. Since the occurrence of a spin density wave is closely connected to the form of the Fermi surface, a detailed study of the electronic structure has been performed to clarify this issue. Recent ARPES investigations on LiFeAs reveal the absence of Fermi surface nesting, high renormalization of the conduction bands and high density of states at the Fermi level [69]. This brings up the question how superconductivity is derived in the stoichiometric superconductor LiFeAs. Recent studies on this

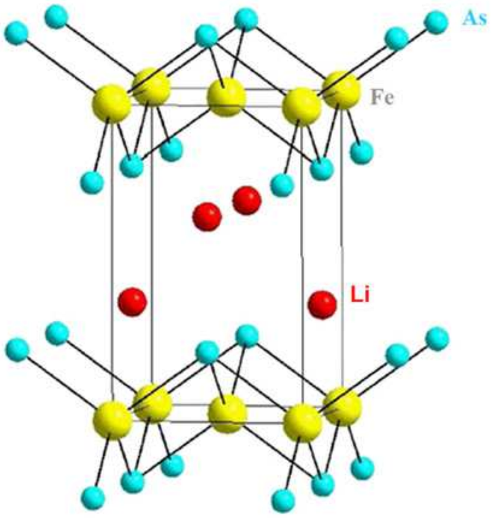

Figure 4.1.1: Crystal structure of LiFeAs which is a $Cu_2Sb/PbClF$-type structure, space group P4/nmm [68].

system have speculated that LiFeAs could be a triplet p-wave superconductor [70, 71], although precise determination and further investigations are necessary to confirm this. This emphasizes the importance of further experimental and theoretical studies of the LiFeAs system.

Owing to the complexities involved in the synthesis, such as the sample handling, LiFeAs turns out to be one of the least studied in Fe-based superconductors, especially when compared to the 122 family. The parent compound LiFeAs crystallizes in a tetragonal $Cu_2Sb/PbClF$-type structure ($P4/nmm$) and consists of Fe_2As_2 layers connected by edge-sharing $FeAs_4$ tetrahedra, similar to other pnictide superconductors [72]. It is well known that all Fe-based superconductors are quite sensitive to chemical substitution and pressure. Even in the isostructural NaFeAs, chemical substitution has been shown to affect T_c significantly [73]. This generated interest towards chemical substitution in the stoichiometric, isostructural and isovalent superconductor LiFeAs. In particular, Pitcher *et al*. [74] have recently reported on the substitution of Fe by Co and Ni in polycrystalline

LiFeAs samples. In the present work, I will focus on the growth of LiFe$_{1-x}$Co$_x$As (x =0, 0.025, 0.05 and 0.075) single crystals, their magnetic and transport properties. Parts of these results were published in Phys. Rev. B [75].

4.2 Crystal growth

Single crystals of LiFe$_{1-x}$Co$_x$As with $x = 0$, 0.025, 0.05 and 0.075 were grown by a self-flux technique, for details see [76, 75]. For the 2.5% Co-doped sample, powder materials of Fe (Alfa Aesar, 99.99%), As (Alfa Aesar, 99.99%), lumps of Li (Alfa Aesar, 99.9%) and Co powder (Alfa Aesar, 99.8%) were used. Initially, As, Fe and Co were ground thoroughly in an agate mortar to ensure homogeneity and then small lumps of the Li metal were added to the Fe-Co-As mixture. A molar ratio of Li : Fe$_{1-x}$Co$_x$: As = 3 : 2 : 3 was used. For the 5% Co-doped sample pre-reacted FeAs, Co$_2$As and metallic Li lumps in the molar ratio of 3 : 2 : 3 was used. For each growth, in total 5 grams of the precursor material were taken in a niobium crucible and welded under 1.2 atmospheric pressure of Ar in an arc-melting facility. The niobium crucible assembly was heated up to 1363 K for 18 hours, dwelling at this point for 5 hours and cooled down to 873 K with a rate of 4.5 K/hour. Thin mm-sized plate-like single crystals were extracted mechanically from the ingot. The inset of Fig. 4.2.1(b) exemplarily shows an as-grown LiFe$_{0.95}$Co$_{0.05}$As single crystal. All crystals grow in a layered morphology with the thickness of the order of μm; they are easy to be cleaved along the *ab*-plane. The layered morphology is apparent in the electron microscope picture Fig. 4.2.1(a). Single crystals of different doping levels, namely, LiFe$_{1-x}$Co$_x$As with $x = 0$, 0.025, 0.05 and 0.075 were grown using this method. All LiFe$_{1-x}$Co$_x$As single crystals are fragile, prone to exfoliation and are even more sensitive to air moisture compared to LiFeAs single crystals.

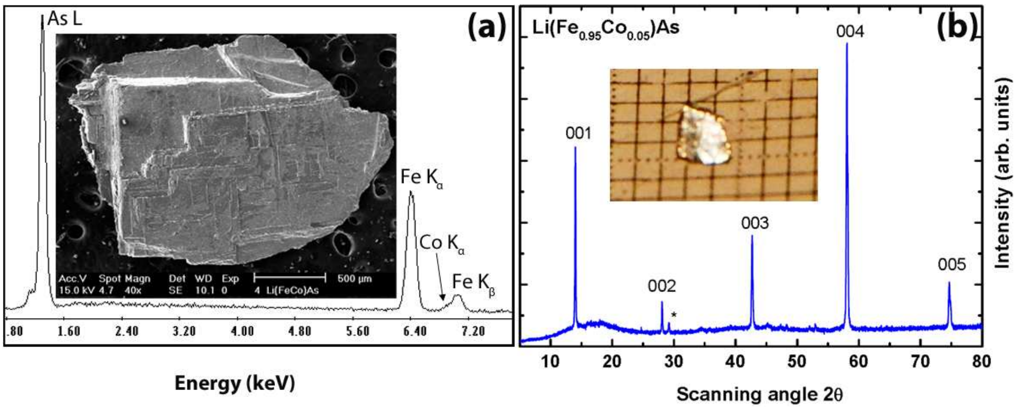

Figure 4.2.1: (a) (a) EDX spectrum of a $LiFe_{0.95}Co_{0.05}As$ single crystal. The inset shows a SEM picture. (b) XRD pattern of a $LiFe_{0.95}Co_{0.05}As$ single crystal, the inset exemplarily shows the picture of an as-grown $LiFe_{0.95}Co_{0.05}As$ single crystal with a shiny and metallic-like surface.

4.3 Characterization

The quality of the as-grown single crystals was assessed by several complementary techniques. Elemental analysis was carried out by ICPOES to get the Li composition in the crystals. The quality, phase purity and compositional analysis of the crystals was also carried out by x-ray diffraction and conventional EDX/SEM .

4.3.1 Inductively coupled plasma spectroscopy

ICPOES measurements were performed by A. Voss. ICPOES analysis was carried out on Co-doped LiFeAs, to measure the composition of the crystals. Samples were prepared as explained in section 2.5. In the case of $LiFe_{1-x}Co_xAs$, competely dissolving crystals to make a clear solution was always a problem as some kind of precipitation accured while dissolving the crystals in HNO_3 acid. This enhanced the error of the accuracy of the compositional analysis. The nominal compositions of the crystals are $LiFe_{0.95}Co_{0.05}As$ and $LiFe_{0.975}Co_{0.025}As$ and the estimated compositions from the ICPOES are $Li_{1.06}Fe_{0.87}Co_{0.04}As_{0.98}$, $Li_{1.17}Fe_{0.85}Co_{0.02}As_{0.99}$. The values of the Li deviate from 1 and exceeding 1 in both samples. The reason for this deviation is yet unclear. The conditions have to be optimized further to dissolve the crystals competely to prepare a clear solution so that to yield higher reliable values of the real composition.

4.3.2 Energy dispersive spectroscopy and x-ray diffraction

Several samples were examined with a Scanning Electron Microscope (see section 2.4). Fig. 4.2.1(a) shows a SEM picture of a $LiFe_{0.95}Co_{0.05}As$ single crystal with nominal composition. The composition is determined by averaging over several points of the same specimen, and for several crystals from each batch. Fig. 4.2.1(a) exemplarily shows such a typical EDX spectrum. The shoulder close to the Fe-K_β line at 7 keV clearly confirms the presence of Co and gives a relatively good estimate of the Co composition. The average Co concentration, measured by EDX for $x_{nominal} = 2.5\%$, 5%, are $x_{EDX} = 3.6\%$, 5.6%. Thus, the deviations from the nominal values are within the absolute error limits of the EDX method. However, the slightly enhanced values as determined from EDX indicate a trend of the actual Co-concentrations to be somewhat higher than the nominal ones. A possible explanation might be excess Co that has been taken from the flux during growth of these crystals. Phase purity of the grown crystals was checked using x-ray diffraction. In order to avoid the degradation of the crystal in air, it was immersed in fomblin oil. Fig. 4.2.1(b) shows a diffraction pattern taken on a plate-like single crystal using a Rigaku miniflex with Cu-K_α radiation. The reflections are indexed to $00l$ indicating the c-axis orientation. However, we see an additional reflection, marked by an asterisk which might indicate that the crystal already started to decompose.

4.4 Magnetization measurements

Fig. 4.4.1 presents the temperature dependent volume susceptibility (χ_{vol}). χ has been deduced from the measured magnetization by correcting for demagnetization effects using an ellipsoidal approximation [77]. We determine T_c from the bifurcation point between ZFC and FC magnetization, and it is found to be 16.8 K, 13.8 K, 10.8 K and 7 K for x = 0, 2.5%, 5% and 7.5% respectively. Interestingly, the substitution of Fe by small amounts of Co apparently results in a significant decrease of the superconducting transition temperature, unlike in the isostructural NaFeAs, where a strong interplay between antiferromagnetism and superconductivity occurs upon doping with Co and Ni, and where superconductivity appears to be stabilized by the substitutions [73]. However, despite the suppression of superconductivity, no signatures of structural/magnetic transitions are observed in the Co-doped samples.

These observations are unexpected, as doping with charge carriers in the $BaFe_2As_2$ suppresses the spin density wave and introduces superconductivity [34, 78]. However, in the present case, superconductivity is suppressed by introducing charge carriers in the LiFeAs system. As shown in Fig. 4.4.1 not only the superconducting transition temperature gets suppressed upon Co-substitution but the width of the transition becomes broader and the superconducting volume fraction decreases, compared to the sharp transition and 100% volume fraction observed for the undoped LiFeAs. This is in agreement with the recent observation of Pitcher *et al.*, who also observed a decrease of T_c, a broadening of the superconducting transition and a decrease of the volume fraction upon Co-substitution in polycrystalline samples of $LiFe_{1-x}Co_xAs$ [74]. Summarizing the reports in literature about the LiFeAs system, the decrease in T_c and the decrease of the superconducting volume fraction seems to be a general result upon doping of charge carriers and/or the presence of impurities in the LiFeAs system [72, 79, 74], in line with the results presented here.

4.5 Resistivity measurements

Resistivity measurements were performed by D. Bombor and A. Bachmann. For each doping level several samples were studied, which yielded a reproducible normalized resistivity (see 4.5.1). However, we observed an unusual spread in their absolute values, clearly exceeding the usual error of the geometric factor (≤10%). The reason for this variation is presently unclear. Nevertheless, the resistivity at room temperature can be specified to be in the range of 0.3-0.6 mΩcm. We observe several systematic tendencies with increasing Co-doping. The residual resistivity ratio $\rho(300\,\mathrm{K})/\rho(20\,\mathrm{K})$ decreases from 24 ($x = 0$) to 7 ($x = 5\%$) and the residual resistivity increases, which could be explained by enhanced scattering of Co-dopants. The superconducting transition width is broadened and shifted to lower temperatures. Using the 90/10 criterion typical superconducting transitions are at $T_\mathrm{c} = (16.6 \pm 0.7)\,\mathrm{K}$ for the undoped compound and $T_\mathrm{c}^{2.5\%} = (16.6 \pm 1.1)\,\mathrm{K}$ and $T_\mathrm{c}^{5\%} = (14.0 \pm 1.2)\,\mathrm{K}$ for the 2.5% and 5% doped samples, respectively. Note, that using this criterion for determining T_c the downgraded superconducting properties at $x = 0.025$ are essentially reflected in the broadened transition width. A more suitable criterion, which also is in line with the results from magnetic susceptibility is the onset temperature of zero resistance. The corresponding values are $T_\mathrm{c,zero}^{0\%} = 15.6\,\mathrm{K}$, $T_\mathrm{c,zero}^{2.5\%} = 13.4\,\mathrm{K}$ and $T_\mathrm{c,zero}^{5\%} = 11.2\,\mathrm{K}$ which differ not more than 1 K from susceptibility measurements.

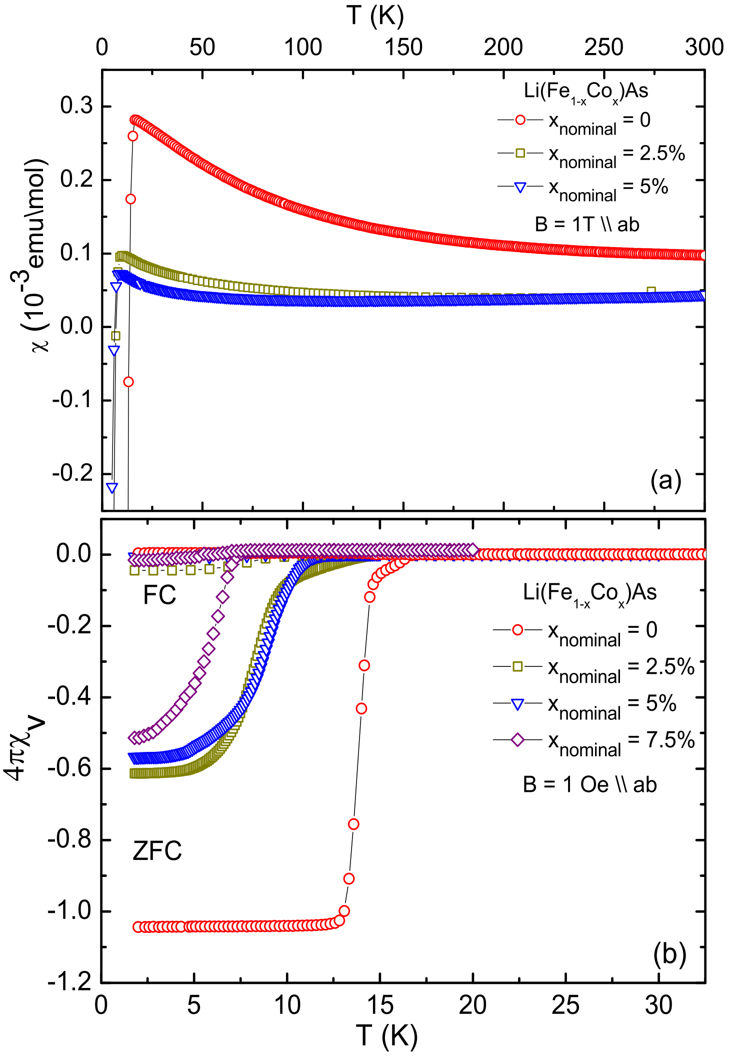

Figure 4.4.1: (a)Temperature dependence of the susceptibilty with an applied field of 1T (b) Temperature dependence of the volume susceptibilty $4\pi\chi_v$ of $LiFe_{0.975}Co_{0.025}As$, $LiFe_{0.95}Co_{0.05}As$ and for $LiFe_{0.925}Co_{0.075}As$ with zero-field cooling (ZFC) and field cooling (FC) in B = 1 Oe. All data have been collected for B$\|$ *ab*.

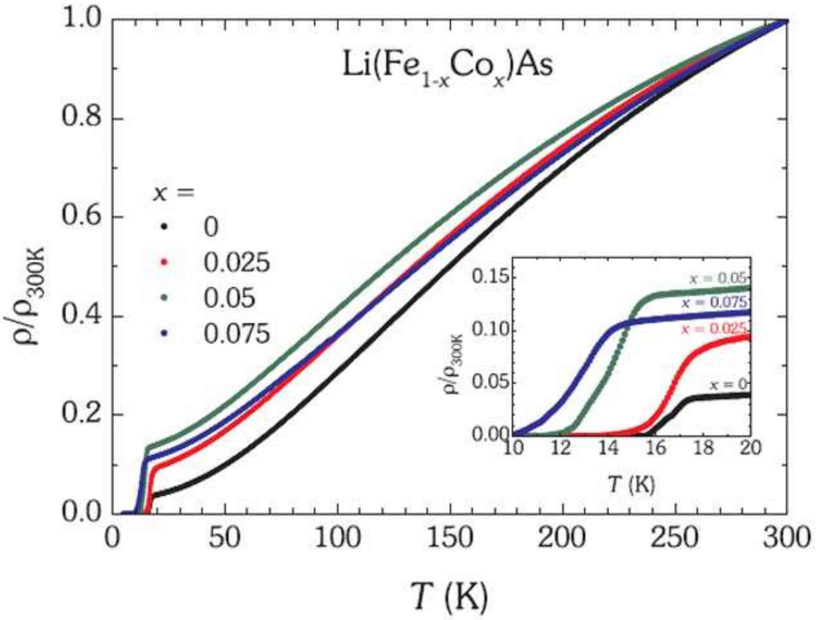

Figure 4.5.1: (a) Temperature dependence of the electrical resistivity $\parallel$ *ab* for different Co-doping levels x of $LiFe_{1-x}Co_xAs$, normalized to the room temperature value. [Data from D. Bombor and A. Bachmann]

4.6 Summary and Conclusion

In summary, single crystals of the new unconventional superconductor $LiFe_{1-x}Co_xAs$ with $x = 0$, 0.025, 0.05, 0.075 were grown. These crystals were characterized with several complementary techniques like ICPOES, SEM-EDX and x-ray diffraction. The superconducting properties have been studied by means of temperature dependent electrical resistivity and magnetic susceptibility measurements. While the parent compound exhibits a sharp superconducting transition, doping with Co at the Fe site suppresses superconductivity quite rapidly. The electronic structure was studied by ARPES, which confirms electron doping upon the substitution of Fe by Co [75]. This study confirms that LiFeAs is unique among the Fe- based superconductors, as charge doping in the $BaFe_2As_2$ family suppresses the spin density wave and introduces superconductivity.

5 Influence of doping in KFe_2As_2 single crystals

5.1 Introduction

KFe_2As_2 is a well known intermetallic compound [80]. However, since early 80´s not much work was done, until the recent discovery of superconductivity in Fe-based materials has brought KFe_2As_2 back into the focus of research again. Superconductivity in stoichiometric KFe_2As_2 is very special case [81, 82, 83, 84] because of its peculiar characteristics like the absence of combined structural and magnetic transitions which are present in $BaFe_2As_2$ and other members of 122 family. Even though KFe_2As_2 belongs to the 122 family, its physical properties like the absence of the Fermi surface nesting [83], resemble more to that of the 111 family like LiFeAs. Dong et al., has shown in their phase diagram a crossover from non-Fermi-liquid behaviour to Fermi-liquid behaviour through a quantum critical point (QCP) at 5 T by resistivity data. One of their main conclusions was the presence of strong antiferromagnetic spin fluctuations. Fig. 5.1.1 shows field induced antiferromagnetic quantum critical point at H_{c2} in KFe_2As_2 [85]. In another study from Grinenko et al., a local moment-induced QCP in KFe_2As_2 single crystals was presented, where it was also proposed that the K122 is close to the incom-

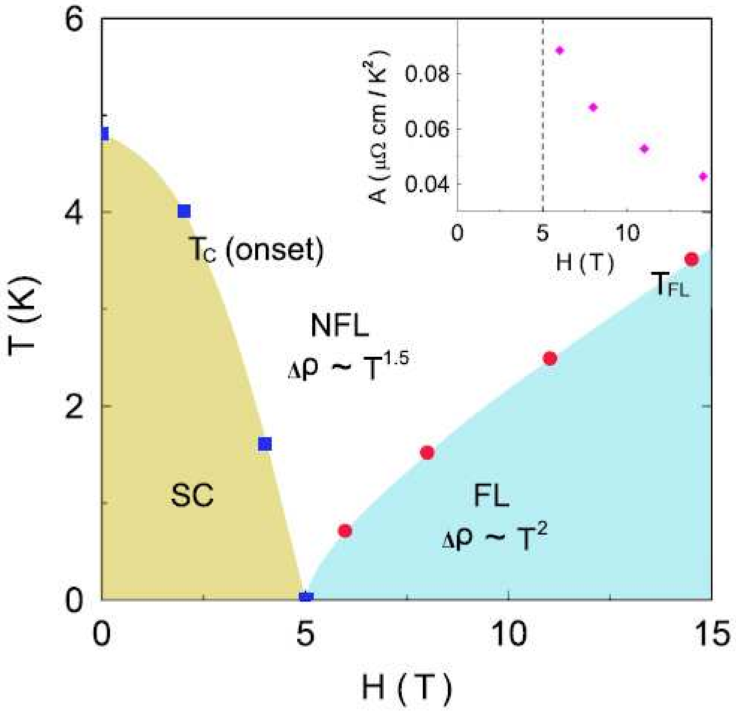

Figure 5.1.1: Field induced antiferromagnetic quantum critical point at 5T in KFe_2As_2 [85].

mensurate SDW state with quantum critical region [86]. Fig. 5.1.2 shows the schematic illustration of the phase diagram, the inset shows the corresponding predicted phase diagram. With the increasing hole doping the valence state of the iron is predicted to change from Fe^{2+} to Fe^{3+} with an AFM state in KFe_2As_2. These features in KFe_2As_2 has to be experimentally investigated. In particular, the valence state of Fe^{3+} is not accomplished experimentaly in Fe-based superconductors. With that motivation, single crystals of KFe_2As_2 parent compound were grown using two different flux techniques namely FeAs flux and KAs flux. Here in this chapter, at first I will focus on the growth of high quality single crystals of KFe_2As_2 parent compound, and in second part of the chapter I will focus on the influence of chemical substitution in KFe_2As_2, especially a systematic investigation of substitution with selected elements like Na, Co, Rh and Cr in KFe_2As_2 single crystals and their physical properties will be presented.

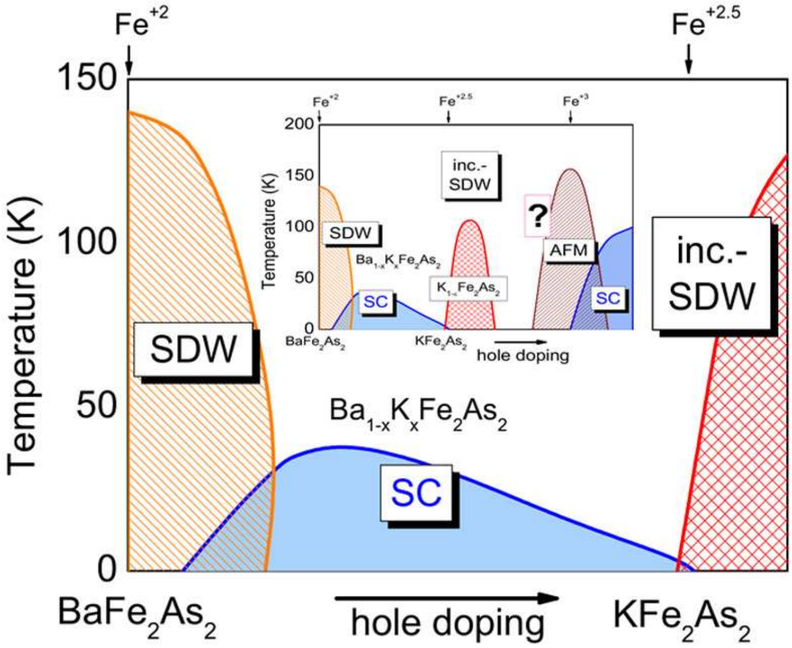

Figure 5.1.2: Schematic phase diagram of the local moment-induced QCP in KFe_2As_2 [86].

5.2 Crystal growth

5.2.1 FeAs flux

Single crystals of KFe_2As_2 have been grown using FeAs-flux with the K:Fe:As in the molar ratio of 1:5:5 by following a similar procedure as described in section of 2.2.5. For the crystal growth several precursor materials were used (for preparation of precursor materials see section 2.1). As a first step the appropriate amounts of precursor material FeAs, Fe_2As and KAs with a total amount of 5 grams were thoroughly ground in an agate mortar. The well ground mixture was placed carefully in alumina crucible and finally sealed in a niobium crucible with Ar atmosphere. The sealed crucible assembly was placed in a vertical furnace, heated up to 1373 K and cooled down to 1023 K with a rate of 2 K/hour. Finally the furnace was cooled very fast from 1023 K to room temperature [87]. All crystals were grown with layer-like morphology and they were quite easy to cleave along the *ab* plane. With the FeAs flux the working temperatures for the growth are rather high, especially when we consider the volatile nature of the potassium. The sizes of the crystals are small because of the small growth region.

5.2.2 KAs flux

Kihou et al.[88] reported centimeter-sized crystals of KFe_2As_2 using KAs flux, where they also investigated the ternary K-Fe-As system. In this work single crystals of KFe_2As_2 have been grown using KAs-flux following the ternary phase diagram [88] in a niobium crucible assembly. As a first step KAs has been prepared by reacting K with the As (see 2.1.3). In the second step precursor materials FeAs and KAs in the molar ration of 2:4 were thoroughly mixed in an agate mortar and placed carefully into the alumina crucible which is sealed inside a niobium container. The sealed crucible assembly is placed in a vertical furnace, heated up to 1173 K and cooled down to 873 K with a rate of 2 K/hour. Finally the furnace is cooled very fast from 1023 K to room temperature. All crystals are grown with layer-like morphology and are quite larger in size compared to the crystals from FeAs flux, but the crystals grown from the KAs flux are more sensitive to air and moisture.

5.3 Characterization

A typical example of as grown KFe_2As_2 single crystals from FeAs flux were shown in Fig 5.3.1(a). The quality of the grown single crystals was assessed by complementary techniques. Several samples were examined with a SEM in EDX mode. The composition was estimated by averaging over several different points of the platelet-like single crystals and is found to be consistent and homogeneous with a 122 composition within the

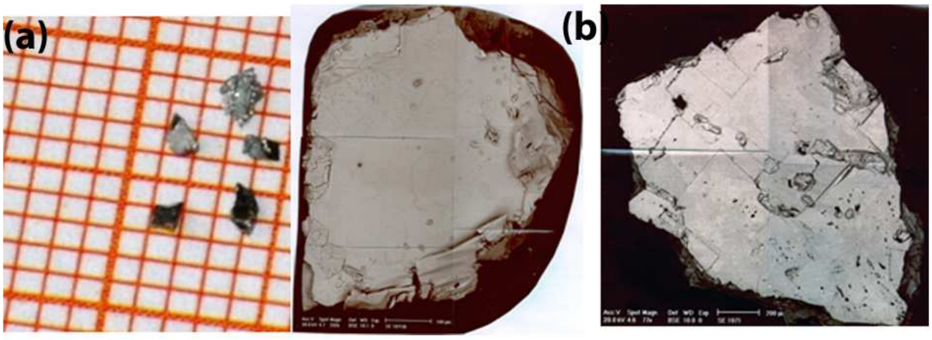

Figure 5.3.1: (a)As-grown single crystals from FeAs flux. (b)SEM pictures of two KFe_2As_2 single crystals grown from FeAs flux.

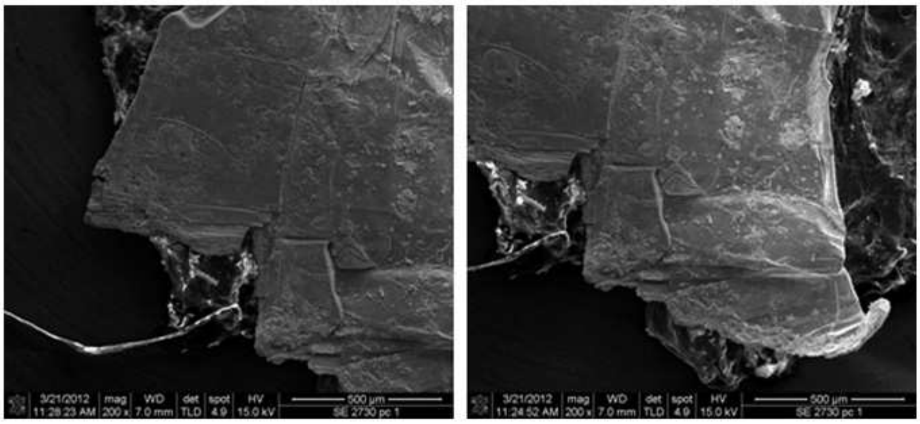

Figure 5.3.2: SEM pictures of two KFe_2As_2 single crystals grown from KAs flux.

instrumental error bars. Typical crystal sizes with a rectangular shape were about $1.2^*\ 0.5mm^2$ and a thickness of 50 μm along the c axis. Fig 5.3.2 shows SEM images of KFe_2As_2 single crystals from KAs flux.

5.4 Magnetization measurements

Superconducting and normal state properties have been measured with temperature dependent magnetization measurements. Bulk superconductivity appears at 3.8 K in both FeAs and KAs flux crystals with 100% superconducting volume fraction as shown in fig 5.4.1(b). It can be concluded that the superconducting properties are the same in both types of crystals but above the superconducting transition few differences were found in susceptibility. A clear splitting is observed in the zero-field-cooled (ZFC) and field cooled (FC) data well above the superconducting transition for FeAs grown crystals whereas in KAs grown crystals does not show any difference between ZFC and FC curves above T_c. This indicates the presence of the magnetic moments in FeAs grown crystals. The normal state susceptibility is also changed in a significant manner in FeAs flux grown crystals compared to KAs flux grown crystals as shown in Fig 5.4.1(a). These differences in the susceptibility may be arising from the induced local magnetic moments which contribute to the susceptibility in the FeAs flux grown crystals. Local moments originating from As vacancies in $LaFeAsO_{1-x}F_x$ has been extensively studied in reference [89, 90]. Where Grinenko et al.found out As vacancies behave as a magnetic defects and contribute to the net magnetic moment. Here in KFe_2As_2 grown from FeAs flux, one could imagine a similar situation that, the point defects might induce local magnetic moments originating from Fe could contribute to large susceptibility [86]. A sufficiently high local defect concentration, can also leads to the formation of magnetic clusters and these magnetic clusters drives the system to more complicated magnetic phases like Griffiths phase as explained in the ref [86]. It would be interesting to grown the single crystals of KFe_2As_2 by varying the concentration of these point defect induced local magnetic moments and investigate the amount of contribution to the net magnetic moment of the crystal. Further investigations in this direction are in progress.

5.5 Resistivity measurements

Resistivity measurements were performed by M. Kumar and V. Grinenko. Fig 5.5.1 compares the temperature dependence of the resistivity measurements for KFe_2As_2 single crystals grown from both techniques. The samples presented in this work have rather

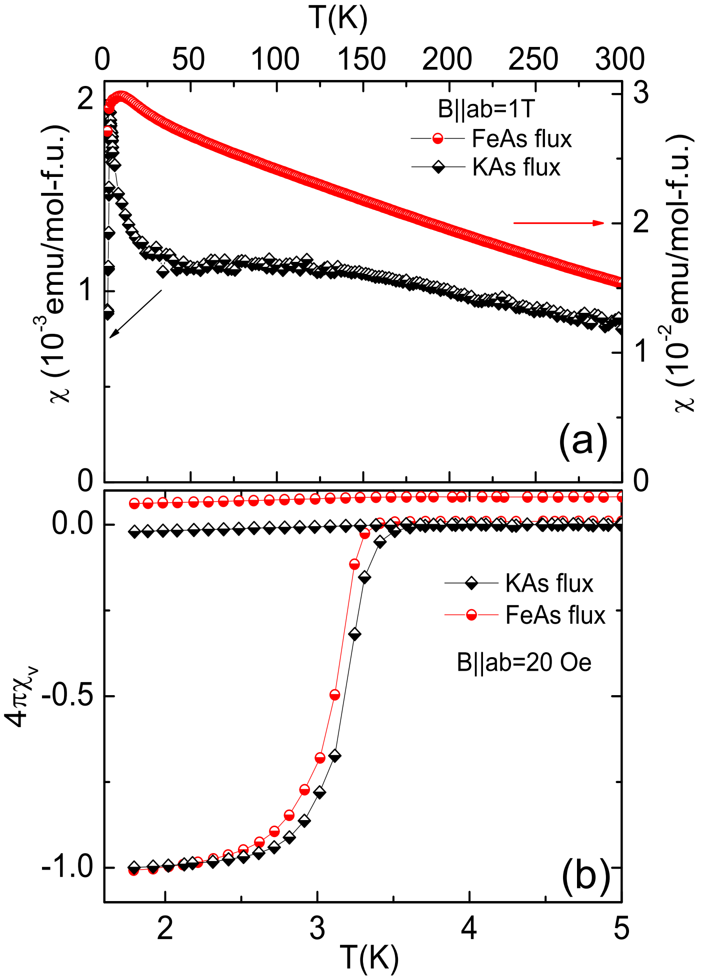

Figure 5.4.1: (a)Temperature dependence of the molar susceptibility for both crystals. (b) Temperature dependence of the volume susceptibility for KFe_2As_2 single crystals [86].

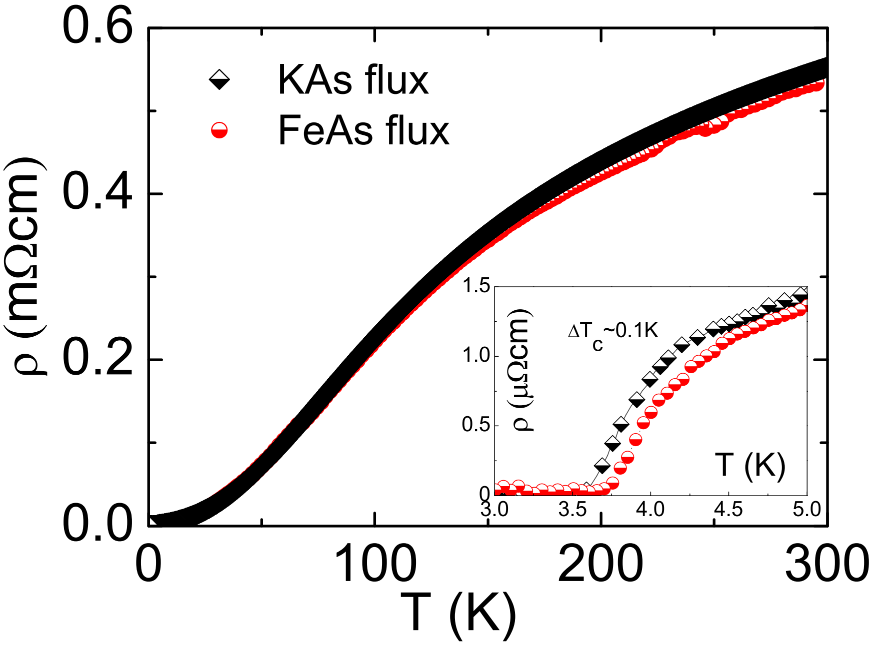

Figure 5.5.1: Temperature dependence of the resistivity for both crystals, which decreases monotonically showing a metallic behavior at all temperatures. Inset shows the superconducting state. [86] [Data from M. Kumar and V. Grinenko].

high transition temperatures: T_c =3.85 K for FeAs-flux-grown sample and T_c = 3.9 K for KAs-flux-grown sample in agreement with magnetization data (section 5.4). RRR values for our crystals are 380 for FeAs-flux crystal and 400 for KAs-flux crystal, the T_c values are comparable with the high T_c-values of other single crystals with large RRR values [91, 92]. The normal state resistivity decreases monotonically showing a metallic behavior at all temperatures for the crystals grown from both techniques. Analysis of the low temperature resistivity data shows a Non-Fermi liquid behaviour for the both crystals [86].

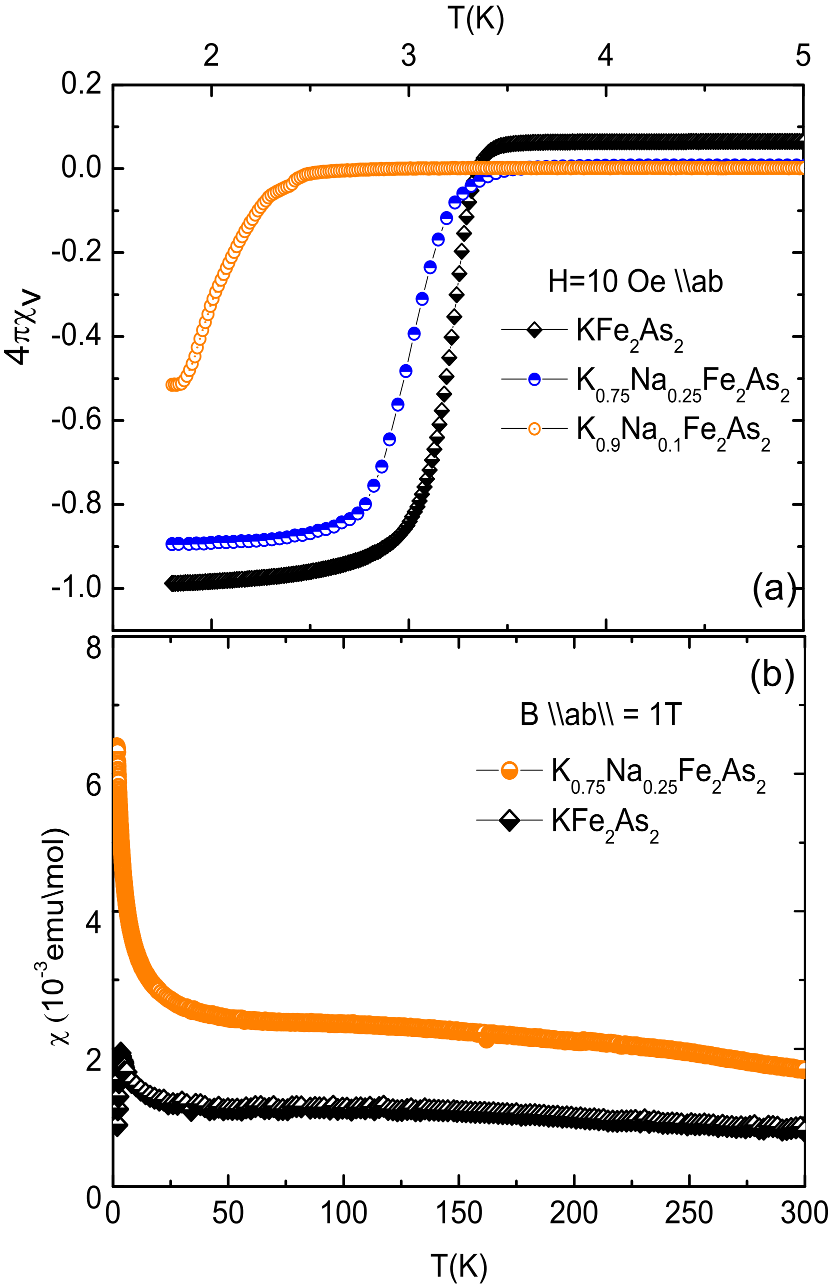

Figure 5.6.1: (a) Volume susceptibility for $(K_{1-x}Na_x)Fe_2As_2$ single crystals. (b) Temperature dependence of the molar susceptibility for $(K_{0.75}Na_{0.25})Fe_2As_2$ with KFe_2As_2 crystals.

5.6 Influence of doping

5.6.1 $(K_{1-x}Na_x)Fe_2As_2$

Chemical substitution allows to systematically vary the physical properties of the Fe-pnictides. However, only few reports on the substitution in KFe_2As_2 system reported yet [93]. Here I will present different chemical substitution in KFe_2As_2 system and their physical properties. Single crystals of $(K_{1-x}Na_x)Fe_2As_2$ with x = 0.1, 0.25, have been grown using KAs-flux. Fig 5.6.1(a) show the temperature dependence of the volume susceptibility for $(K_{1-x}Na_x)Fe_2As_2$ single crystals as a function of different levels of Na. Substitution of Na^+ atoms to K^+ does not act like a simple conventional doping, but the atomic size is different for both, there is difference in the electronic distribution and hence there is a change in the superconducting transition temperature. For $(K_{0.9}Na_{0.1})Fe_2As_2$ superconducting transition did not change drastically but the transition becomes broad and volume fraction slightly decreases. For $(K_{0.75}Na_{0.25})Fe_2As_2$ the superconducting transition is shifted to lower temperature with T_c = 2.5 K and the volume fraction is less than 50%. Fig 5.6.1(b) shows temperature dependence of the molar susceptibility for KFe_2As_2 in comparison with the $(K_{0.75}Na_{0.25})Fe_2As_2$, qualitatively the data are similar except that there is a small shift in the susceptibility with substitution of Na. Fig 5.6.2 shows the resistivity measurement for the $(K_{0.75}Na_{0.25})Fe_2As_2$ crystal, the onset of the superconducting transition starts already at 3.8 K but the resistivity drops completely at T_c = 2.5 K which is in line with the magnetization data. The RRR value for the $(K_{0.75}Na_{0.25})Fe_2As_2$ crystal is found to be 71 which is rather less compared to the values of the pristine KFe_2As_2 crystals, consistent with a higher degree of disorder upon the substitution of K by Na.

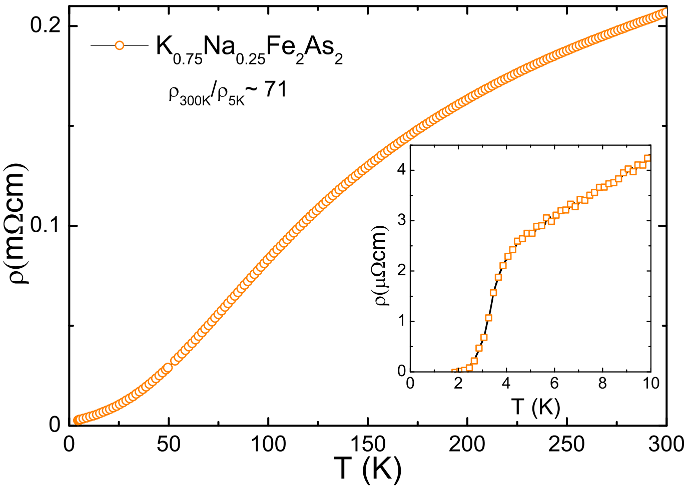

Figure 5.6.2: (a)The resistivity as a function of temperature for $(K_{0.75}Na_{0.25})Fe_2As_2$ [Data from M. Kumar].

5.6.2 $K(Fe_{1-x}Tm_x)_2As_2$

In Fe-As superconductors, transition metal (Tm) substitution at the Fe site is proved to be rather homogeneous and a efficient way to induce superconductivity, compared to the homogenity with alkali metals doping in Fe-pnictides. Here I will present on going work on crystal growth and magnetic measurements performed on transition metal doping in $K(Fe_{1-x}Tm_x)_2As_2$ crystals where Tm = Rh, Co and Cr. Single crystals of $K(Fe_{0.95}Rh_{0.05})_2As_2$ were grown using KAs-flux similarly to the section 5.2.2. It was found that the superconducting transition temperature has been shifted to lower temperatures with 5% of Rh substitution at the Fe site compared to the undoped. T_c derived from low field susceptibility is 2.3 K, which is shown in the Fig 5.6.3(a). The superconducting volume fraction is found to be extremely low, suggesting that 5% of Rh already suppressed the superconductivity, as shown temperature dependence of the volume susceptibility in Fig 5.6.3(a) for $K(Fe_{0.95}Rh_{0.05})_2As_2$ single crystals. Fig 5.6.3(b) shows temperature dependence of the molar susceptibility measured in applied field of 1 T for KFe_2As_2 crystals in comparison with the $K(Fe_{0.95}Rh_{0.05})_2As_2$. The normal state state

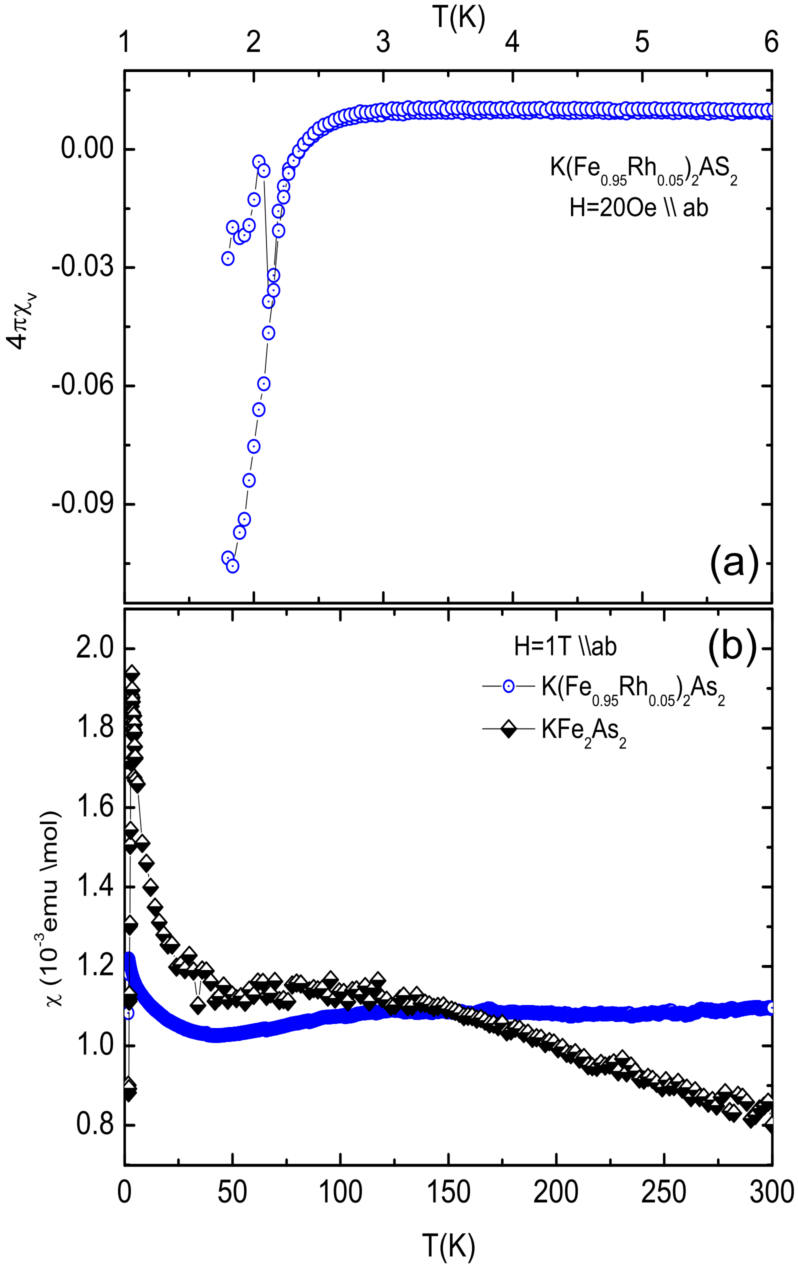

Figure 5.6.3: (a) Low field susceptibility measurements and (b) susceptibility with an applied field of 1T for $K(Fe_{0.95}Rh_{0.05})_2As_2$ single crystals.

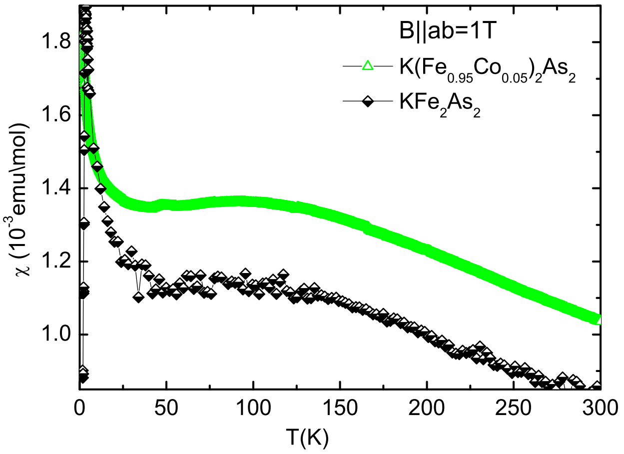

Figure 5.6.4: (a) Susceptibility for $K(Fe_{0.95}Co_{0.05})_2As_2$ single crystals as a function of temperature.

susceptibility is on the same order of magnitude. But with 5% Co and Cr substitution in Fe site i.e., $K(Fe_{0.95}Co_{0.05})_2As_2$, $K(Fe_{0.95}Cr_{0.05})_2As_2$ superconductivity is completely suppressed. The normal state susceptibility is shown in Fig 5.6.4, Fig 5.6.5. The influence of Co and Cr is rather large in suppressing the superconductivity compared to the Rh-doped sample which is still superconducting with 5%. This results confirms that 5% transition metal (Tm) substitution has a large influence in KFe_2As_2 crystals, this is because with the 5% Co substitution in KFe_2As_2 induces large impurity scattering, which may act as a pair breaking leading to suppression of superconductivity which is opposite to Co-substituted $BaFe_2As_2$. This result is in line with the recent study by Wang et al.[93] where they also found that Co-substitution in KFe_2As_2 resulted in rapid suppression of the superconductivity. In their study they found out a universal heat conduction through thermal conductivity measurements in both KFe_2As_2 and Co-substituted KFe_2As_2, they speculated this universal heat conduction in KFe_2As_2 as an evidence for the d-wave superconducting state [93], and needs to be further investigated in this system.

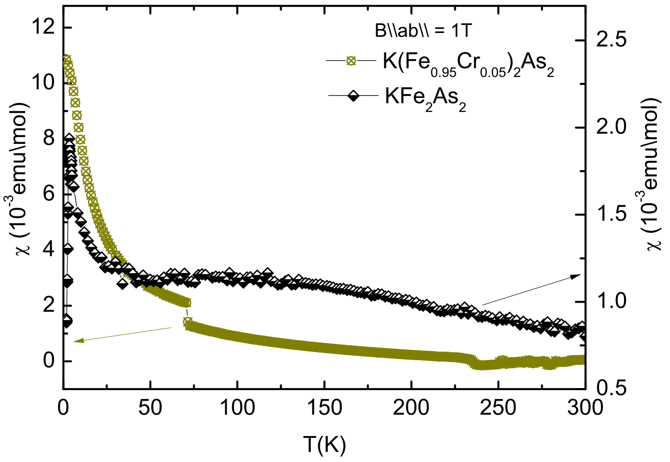

Figure 5.6.5: Normal state susceptibility for $K(Fe_{0.95}Cr_{0.05})_2As_2$ single crystals.

5.7 Summary and Conclusion

In summary, single crystals of the new unconventional superconductor KFe_2As_2 were successfully grown with FeAs and KAs flux. These crystals were characterized with SEM-EDX and x-ray diffraction. The superconducting properties have been studied by means of temperature dependent electrical resistivity and magnetic susceptibility measurements. The superconducting transition was found to be 3.8 K for crystals grown from both flux types while the normal state susceptibility has significantly enhanced by an order of magnitude in FeAs flux grown crystals. This higher magnetic moment can be explained, by considering the formation of localized Fe moments [86]. The influence of Na, Rh, Co and Cr substitution in KFe_2As_2 have been investigated and preliminary results were presented. With Na substitution at K site and with Rh substitution at Fe site, superconductivity has been suppressed to lower temperatures. While with Co and Cr doping at Fe site superconductivity is destroyed rapidly with very small amounts of substitution like 5% in KFe_2As_2 single crystals. All the important observations have been summarized in Table 5.7.1.

Table 5.7.1: Physical properties of KFe_2As_2 single crystals.

$Crystals$	$Flux$	$T_C(K)$	$Non-SC$	χ@$300(K)$
KFe_2As_2	$FeAs$	3.8	*	1.537×10^{-2}
KFe_2As_2	KAs	3.8	*	0.08×10^{-3}
$(K_{0.75}Na_{0.25})Fe_2As_2$	KAs	2.4	*	1.696×10^{-3}
$K(Fe_{0.95}Rh_{0.05})_2As_2$	KAs	2.3	*	1.096×10^{-3}
$K(Fe_{0.95}Cr_{0.05})_2As_2$	KAs	*	$Non-SC$	0.52×10^{-3}
$K(Fe_{0.95}Co_{0.05})_2As_2$	$FeAs$	*	$Non-SC$	1.035×10^{-3}

This study confirms that KFe_2As_2 is different among the Fe-based superconductors, especially compared to the rest of the 122 compounds, where charge doping in $BaFe_2As_2$ family suppresses the spin density wave and introduces superconductivity [94].

6 Influence of Eu in $BaFe_2As_2$ single crystals

6.1 Introduction

In the "122" family of Fe-As superconductors, $EuFe_2As_2$ is yet another special member because of the presence of large local magnetic moments of Eu^{2+} which order antiferromagnetically at around 20 K [20, 19]. Like the rest of the 122 compounds, $EuFe_2As_2$ also undergoes a SDW transition at 200 K, and superconductivity can be introduced by suppressing this SDW by either chemical substitutions or by external pressure [19, 95, 96]. Jiang et al.[97] have shown that there is a strong interaction between the localized spins of Eu with the conduction electrons from the FeAs layers, so the system is higly interesting for studing magnetic interactions. Motivation of this study was to see the influence of the magnetic rare earth to the conduction FeAs layers in $BaFe_2As_2$, so for that reason Eu is chosen to substitute at the Ba-site, with a fixed amount of Eu at Ba-site, i.e., 40% and systematically change the Co content at Fe site yielding $(Ba_{0.6}Eu_{0.4})(Fe_{1-x}Co_x)_2As_2$. Here in this chapter I will present crystal growth from self flux technique and a systematic investigation of magnetic and superconducting properties of $(Ba_{0.6}Eu_{0.4})(Fe_{1-x}Co_x)_2As_2$ single crystals from temperature dependent magnetization, resistivity and finally I will

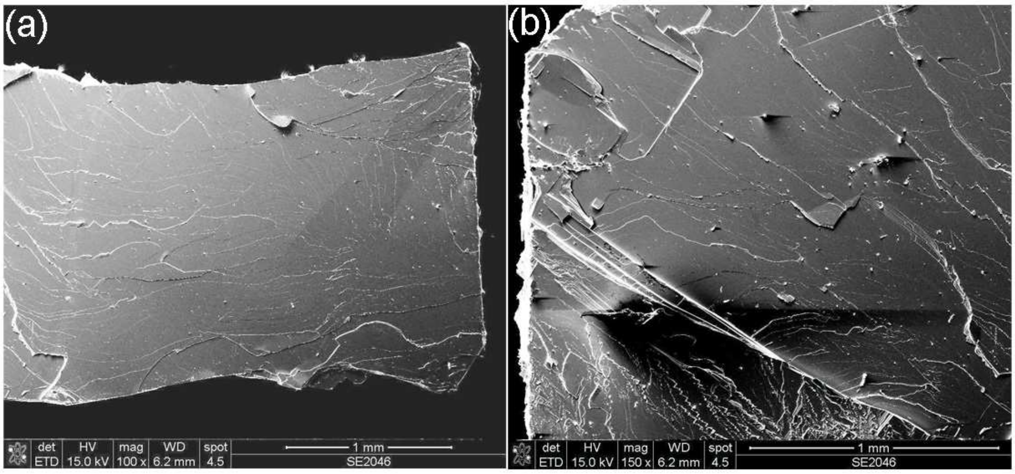

Figure 6.2.1: (a) (b) SEM images of as grown $(Ba_{0.6}Eu_{0.4})(Fe_{0.85}Co_{0.15})_2As_2$ single crystal from FeAs flux

present some preliminary results from ESR measurement on this series of single crystals.

6.2 Crystal growth and characterization

Single crystals of $(Ba_{0.6}Eu_{0.4})(Fe_{1-x}Co_x)_2As_2$ were grown with self-flux (see section 3.2.1). The amount of Eu is fixed to 40% and amount of Co on Fe-site is varied. The precursor materials FeAs, Fe_2As, Co_2As, BaAs and metallic Eu were mixed with a molar ratio of $(Ba_{0.6}Eu_{0.4})(Fe_{1-x}Co_x)_{3.1}As_{3.1}$. This composition was used to achieve a homogeneous melt at T = 1463 K, and then the melt was cooled slowly to achieve the crystal growth (see section 3.2.1). Single crystals of $(Ba_{0.6}Eu_{0.4})(Fe_{1-x}Co_x)_2As_2$ with nominal composition of x = 0, 0.05, 0.1, 0.15 and 0.2 were grown. Platelet-like single crystals of cm-size were obtained, the surfaces of which are shiny and metallic like. All crystals show a layered morphology and are easy to cleave along the *ab* plane. Fig 6.2.1 shows exclusively SEM pictures of $(Ba_{0.6}Eu_{0.4})(Fe_{1-x}Co_x)_2As_2$ crystals with x = 0 and 0.05.

6.3 Magnetization measurements

Fig 6.3.1(b) shows the measurement on $(Ba_{0.6}Eu_{0.4})Fe_2As_2$ where the combined structural and magnetic $T_{S/N}$ transition is shifted to 152 K. With the 40% of Eu at Ba site the $T_{S/N}$ transition has been shifted and is in the middle of the SDW transitions of $EuFe_2As_2$ where the $T_{S/N}$ transition is at 190 K [19] and $BaFe_2As_2$ where the $T_{S/N}$ transition is at 137 K (see Fig 6.3.1(a)). This transition is also confirmed in the resistivity measurement. Fig 6.3.1(c) shows a comparison of resistivity measurements for both $BaFe_2As_2$ and $(Ba_{0.6}Eu_{0.4})Fe_2As_2$ where the anamolies are pronounced at 137 K and 152 K which are in good agreement to susceptibility. Now with the introduction of Co at Fe site, i.e., $(Ba_{0.6}Eu_{0.4})(Fe_{1-x}Co_x)_2As_2$ this $T_{S/N}$ transition is suppressed and superconductivity is achieved with x = 0.1 and 0.15 with $T_c = 20$ K and 10 K as shown in Fig 6.3.2(c). For x = 0.05 (underdoped), 0.2 (overdoped) no superconducting transition is observed down to 1.8 K. All the samples show a simple paramagnetic behaviour in the temperature range 20 to 300 K, with an applied field of 1 T which is shown in Fig 6.3.2(b). The inverse susceptibility plotted as a function of temperature is linear until 300 K, and below 20 K Eu^{2+} orders antiferromagnetically as indicated by the linearity of the inverse susceptibilty deviating at 20 K. This is more evident in the sample x = 0.1 where there is a kink at 20 K in susceptibility which can be attributed to the local ordering of Eu^{2+} which is also observed in $EuFe_2As_2$ [19]. The normal state susceptibility of the superconducting sample $(Ba_{0.6}Eu_{0.4})(Fe_{0.9}Co_{0.1})_2As_2$ with the $T_c = 20$ K is lower compared to the other samples as shown in Fig 6.3.1(a). The deviation from the rest of the samples is also visible in inverse susceptibility Fig 6.3.1(b). In resistivity data no is no such deviation for this specific sample (see Fig 6.4.1) and further investigation is needed to clarify this feature.

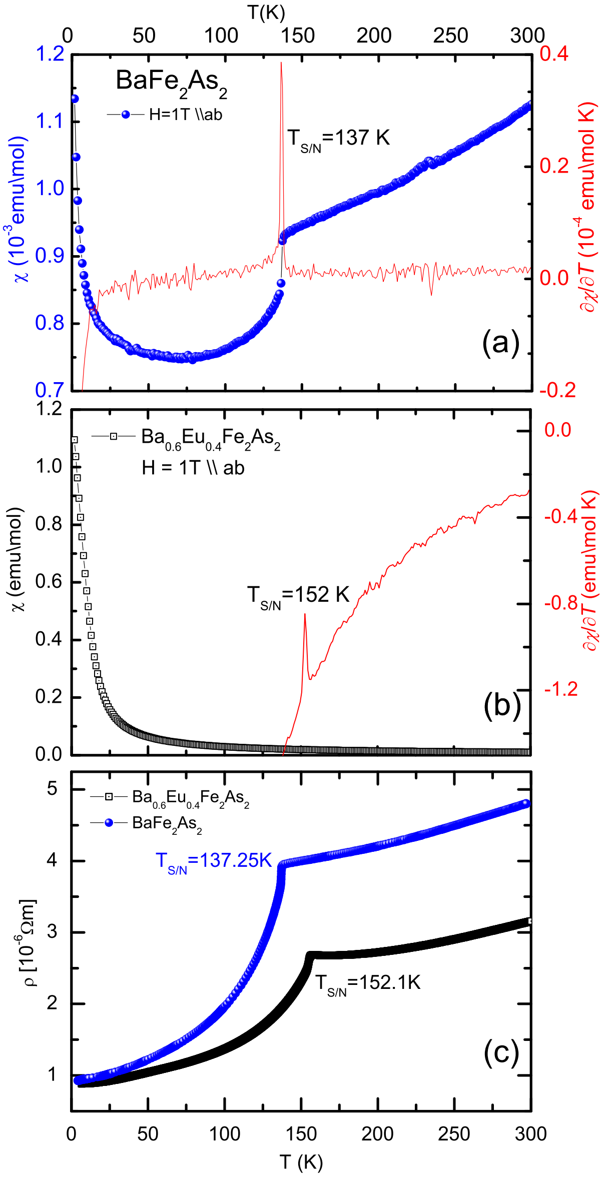

Figure 6.3.1: (a)(b)Molar susceptibility as a function of temperature for BaFe$_2$As$_2$ and (Ba$_{0.6}$Eu$_{0.4}$)Fe$_2$As$_2$ single crystals. (c) Temperature dependent resistivty for BaFe$_2$As$_2$ and (Ba$_{0.6}$Eu$_{0.4}$)Fe$_2$As$_2$ single crystals.

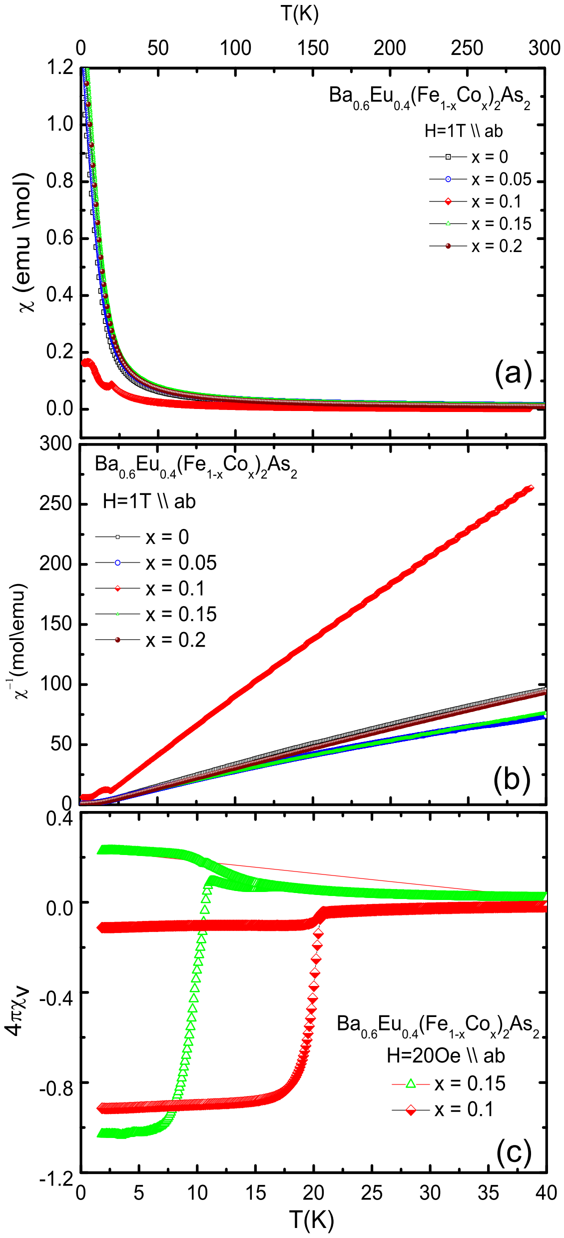

Figure 6.3.2: (a)Temperature dependence of the molar susceptibility, (b)inverse susceptibility as a function of temperature showing the linear paramagnetic behaviour for $(Ba_{0.6}Eu_{0.4})(Fe_{1-x}Co_x)_2As_2$ single crystals. (c)Temperature dependence of the volume susceptibility for two superconducting single crystals.

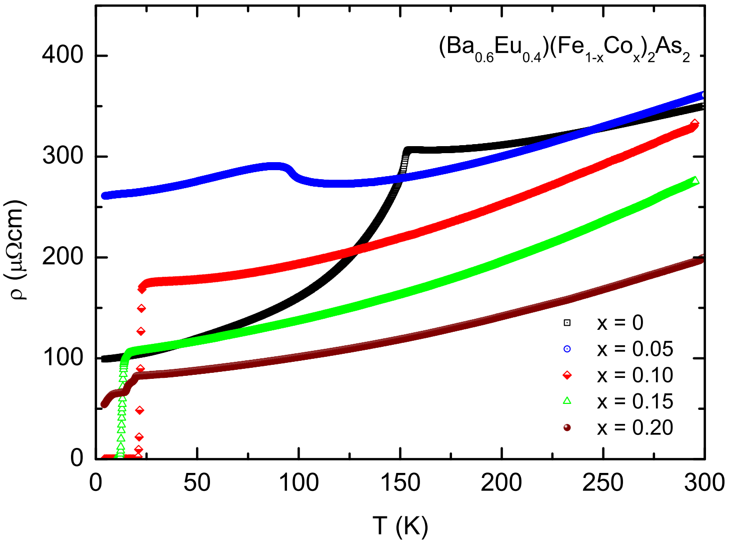

Figure 6.4.1: (a)Temperature dependence of resistivty for (Ba$_{0.6}$Eu$_{0.4}$)(Fe$_{1-x}$Co$_x$)$_2$As$_2$ single crystals. [Data from A. Bachmann]

6.4 Resistivity measurements

Resistivity measurements were performed by A. Bachmann. Fig 6.4.1 shows the temperature dependent resistivity measurements on (Ba$_{0.6}$Eu$_{0.4}$)(Fe$_{1-x}$Co$_x$)$_2$As$_2$ single crystals. The T$_{S/N}$ transition at 152 K in (Ba$_{0.6}$Eu$_{0.4}$)Fe$_2$As$_2$ is shifted to lower temperature and becomes quite broad with 5% Co doping at the Fe site but no traces of a superconducting transition are observed down to 1.8 K. With 10% Co doping the T$_{S/N}$ transition is completely suppressed and superconductivity is evolved with the T_c=20 K which is in good agreement with the magnetization data. Superconducting transition temperature is not enhanced with further increasing of the Co-content but rather decreased to lower temperature, as evident with 15% Co-doping where the T_c shifted to 10 K. For 20% Co-doping however, no superconductivity is observed, and this matches perfectly with the magnetization data. Some important observations are shown in Table 6.6.1.

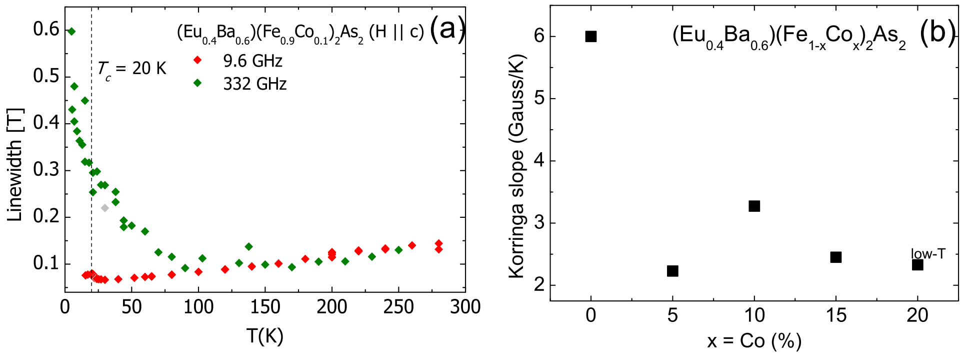

Figure 6.5.1: (a) Line width plotted as a function of temperature and (b) Korringa slope as a function of Co-concentration for $(Ba_{0.6}Eu_{0.4})(Fe_{0.9}Co_{0.1})_2As_2$ single crystals [Data from G. Lang] [98]

6.5 ESR measurements

ESR measurements were performed and analysed by G. Lang, A. Alfonsov, R. Zahn, and V. Kataev. Electron Spin Resonance is a powerful tool to study the spin dynamics and the magnetic interactions in the system. ESR technique is based on the resonant absorption of electromagnetic radiation in a magnetic field which in microwave region probes the magnetic moment of the elecrons. So to study the interactions of magnetic rare earth Eu with the conduction electrons in $(Ba_{0.6}Eu_{0.4})(Fe_{1-x}Co_x)_2As_2$ ESR is an ideal tool. Fig 6.5.1 (a) shows the temperature dependent ESR line width for optimally doped $(Ba_{0.6}Eu_{0.4})(Fe_{0.9}Co_{0.1})_2As_2$ single crystal with the transition temperature of T_c=21 K at two different frequencies. The slope remains linear until around 90 K and starts deviating at lower temperatures, the same behaviour was observed in $GdFeAsO_{1-x}F_x$ where there was a strong coupling to the conduction electrons of FeAs layers to the rare earth Gd [99, 100]. Here in case of $(Ba_{0.6}Eu_{0.4})(Fe_{0.9}Co_{0.1})_2As_2$ one could imagine a similar situation, with the Eu spins interacting with the conduction electrons of FeAs-layers [98]. Fig 6.5.1(a) shows the Korringa slope (which is a reciprocal of T_1 relaxation time to the square of the density of states) as a function of Co-concentration for all the doping levels

Table 6.6.1: Physical properties of $(Ba_{0.6}Eu_{0.4})(Fe_{1-x}Co_x)_2As_2$ single crystals.

$x_{Nominal}$	$T_{S/N}{}^{\chi}$(K)	$T_{S/N}{}^{\rho}$(K)	$T_C{}^{\chi}$	$T_C{}^{\rho}$	$\Delta\ T_C$
0.0	152.5	152.1	[a]	[a]	0.4
0.05	[a]	96.5	[a]	[a]	[a]
0.10	[a]	[a]	20.4	21.9	1.5
0.15	[a]	[a]	10.6	13.3	2.7
0.20	[a]	[a]	[a]	[a]	[a]

[a] absent

of $(Ba_{0.6}Eu_{0.4})(Fe_{1-x}Co_x)_2As_2$ with x = 0, 0.05, 0.1, 0.15 and 0.2. The slope changes from the samples which show SDW to the samples which show superconductivity, this behaviour is quite consistent to the one observed in other Co-doped Eu122 system [101].

6.6 Summary and Conclusion

In summary, single crystals of $(Ba_{0.6}Eu_{0.4})(Fe_{1-x}Co_x)_2As_2$ with x = 0, 0.05, 0.1, 0.15 and 0.2 have been successfully grown and characterized. The SDW transition for $(Ba_{0.6}Eu_{0.4})Fe_2As_2$ is found to be at 152 K, which is in between $BaFe_2As_2$ and $EuFe_2As_2$. Upon substitution of Co at Fe-site, the SDW is shifted to lower temperatures, and with x = 0.1 bulk supercondcutivity is achieved. With higher Co-content superconductivity is suppressed. The magnetic correlations have been investigated with ESR, this data clearly suggests that there is a strong coupling of Eu spins with the conducting electrons of Fe-As layers.

7 Summary/conclusions and Outlook

This work emphasizes important aspects of crystal growth and the influence of chemical substitution in Fe-As superconductors and the physical properties. The high temperature solution growth technique is one of most powerful and widely used technique to grow single crystals of various materials. The biggest advantage of the high temperature solution growth technique is the possibility of growing single crystals from both congruently and incongruently melting materials. Solution growth technique also has the potential to control high vapour pressures, given the fact that, in Fe-based superconductors elements with high vapor pressure like As, K, Li and Na have to be handled during the crystal growth procedure. In this scenario high temperature solution growth is the best suitable growth technique to synthesize sizable homogeneous single crystals.

Using self-flux high temperature solution growth technique, large centimeter-sized high quality single crystals of $BaFe_2As_2$ were grown [39, 56]. This pristine compound $BaFe_2As_2$ undergoes structural and magnetic transition at $T_{S/N}$=137 K. By suppressing this magnetic transition and stabilizing tetragonal phase with chemical substitution, like Co-doping and Na-doping, bulk superconductivity is achieved. Superconducting transitions as high as $T_c = 34$ K upon Na substitution and $T_c = 25$ K upon Co-substitution were obtained. The normal state resistivity behaviour of $BaFe_2As_2$ is typical metallic-like, decreasing with lowering of temperature until it reaches $T_{S/N}$. With the substitution of Fe by Co the transitions $T_{S/N}$ split up and shift to lower temperature, with high Co-content these transitions are completely suppressed and superconductivity is accomplished. It is the same case with the Na-doping on Ba atoms, i.e., the $T_{S/N}$ transition is shifted to lower temperature, but in this case there is no splitting of the $T_{S/N}$ transitions. With a high Na-content bulk superconductivity arises. A combined electronic phase diagram has been achieved for both electron doping with Co and hole doping with Na in $BaFe_2As_2$ as discussed in chapter 3.

Single crystals of $LiFe_{1-x}Co_xAs$ with $x = 0$, 0.025, 0.05 and 0.075 were grown by a self-flux high temperature solution growth technique [75]. All the single crystals of the LiFeAs family are fragile, extremely sensitive to air, moisture and prone to exfoliation. Superconductivity in LiFeAs is extremely sensitive to the stoichiometry and rapidly suppressed with charge doping. The charge doping in LiFeAs is achieved by substitution of Fe by Co. The superconducting properties investigated by means of temperature dependent magnetization and resistivity revealed that superconductivity is shifted to lower temperatures and with higher amount of charge carriers superconductivity is suppressed. This is unexpected as in case of $BaFe_2As_2$ superconductivity has been achieved through charge doping by suppressing the magnetic ordering. This proves that the LiFeAs is a unique member of the Fe-As superconductors.

Single crystals of KFe_2As_2 were grown with two different types of fluxes, namely, FeAs-flux and KAs-flux. The superconducting transition is found to be at 3.8 K in both types of crystals as revealed in both magnetization and resistivity data. But the normal state susceptibility has been significantly enhanced in FeAs-flux grown crystals compared to KAs-flux. This might be attributed to associated Fe local moments. The influence of doping with selected elements like Na, Rh, Co and Cr has been investigated systematically in KFe_2As_2 single crystals. With Na-doping at the K-site, yielding

$(K_{1-x}Na_x)Fe_2As_2$, superconductivity is suppressed to lower temperatures and the normal state susceptibility is comparable to the parent compound KFe_2As_2. With the partial substitution of Rh at Fe site, yielding $K(Fe_{0.95}Rh_{0.05})_2As_2$, superconductivity is also suppressed to lower temperatures. Substitution of Co and Cr at Fe site, yielding $K(Fe_{0.95}Co_{0.05})_2As_2$, $K(Fe_{0.95}Cr_{0.05})_2As_2$ superconductivity is completely suppressed. This study shows that superconductivity in KFe_2As_2 is very sensitive to chemical substitution [94].

Magnetism and magnetic order in Fe-As superconductors is one of the crucial topics to be investigated especially when a magnetic rare earth element is involved in the system. Chapter 6 gives the preliminary investigation performed on the influence of Eu in $BaFe_2As_2$ single crystals. Single crystals of $(Ba_{0.6}Eu_{0.4})(Fe_{1-x}Co_x)_2As_2$ with x = 0, 0.05, 0.1, 0.15 and 0.2 were grown with solution growth technique using Fe-As flux and investigated with several physical measurements. With 40% of Eu at Ba site (yield $(Ba_{0.6}Eu_{0.4})Fe_2As_2$), the magnetic transition is shifted to 152 K which is inbetween the transition observed for $BaFe_2As_2$ (137 K) and $EuFe_2As_2$ (190 K). As expected superconductivity is achieved with 10 and 15% of Co substitution at the Fe site, which confirms that the superconducting dome in the phase diagram shrinks upon Eu substitution in $BaFe_2As_2$ compared to the $Ba(Fe_{1-x}Co_x)_2As_2$ phase diagram. ESR measurements on this system clearly revealed the interaction of Eu with the conduction electrons in the Fe-As layers.

In summary, the work at hand presents optimized crystal growth techniques for growing single crystals of newly discovered Fe-based superconductors using the high temperature solution growth technique. The growth conditions are optimally developed to grow flux free large single crystals. The high quality of the crystals were revealed by several physical properties, as a prominent example, single crystals of $Ba(Fe_{1-x}Co_x)_2As_2$ are of extraordinary high quality which was confirmed by the magnetic ac susceptibility which showed a very sharp superconducting transition [55]. Further optimization of the growth parameters are required, especially to improve the growth along *c*-direction in order to have much thicker single crystals e.g., for further neutron studies. Microscopic investigation of the magnetic order in parent compounds associated with the different dopants has to be investigated to get more insight into magnetism and superconductivity of the Fe-based superconductors. During the course of this PhD work, I have provided samples to several local and international collaborators, resulting in 8 published papers, 6 manuscripts submitted to peer reviewed journals and few more are in preparation.

List of Figures

1.0.1 Superconductivity over the years. [Image courtesy of DOE, US. [5]] . . . 2

1.1.1 Six different types of crystal structures from Fe-As superconductors [11] . 4

1.1.2 Electronic phase diagram of LaFeAsO$_{1-x}$F$_x$ showing structural (T_S), magnetic (T_N) and superconducting transition (T_c) temperatures [13] 5

1.1.3 The generic phase diagram of electron and hole doping in Fe-As superconductors, showing structural (T_S), magnetic (T_N) and superconducting transition (T_c) temperatures [21]. 6

1.1.4 (a) K-doped BaFe$_2$As$_2$ phase diagram (b) Co-doped BaFe$_2$As$_2$ phase diagram [22, 23] 7

2.1.1 Pressed pellets of FeAs before the heat treatment in the sealed quartz tube with vacuum inside 12

2.1.2 Specially designed silica tube with glassy carbon crucible inside for the vapour transport reaction of BaAs. 12

2.2.1 Solubility curve as a function of temperature [32]. 15

2.2.2 Binary phase diagram showing region for solution growth [32]. 15

2.2.3 Schematic illustration of the solution growth technique. 16

3.1.1 Crystal structure of $BaFe_2As_2$ which is a $ThCr_2Si_2$-type structure, space group I4mmm [34]. 22

3.2.1 (a) Double-wall crucible assembly: (1) outer-alumina-shield, (2) inner-alumina-shield, (3) alumina-wool, (4) alumina lid, (5) alumina crucible, (6) molten charge, (7) Silica ampoule. (b) Temperature gradient over the length of the crucible [39]. 24

3.2.2 (a) $Ba(Fe_{0.9}Co_{0.1})_2As_2$ (b) $BaFe_2As_2$. Inset in (a) shows a parallel cleaved surface at 2 mm from the cleavage plane in main panel. 25

3.2.3 SEM images of single crystals grown using the self-flux technique: large cleaved sections of: (a) $Ba(Fe_{0.95}Co_{0.05})_2As_2$ (b) $BaFe_2As_2$ (c) and (d) show the layer by layer growth of these single crystals and a tendency towards exfoliation owing to the layered structure 27

3.2.4 Lattice parameters of $Ba(Fe_{1-x}Co_x)_2As_2$ single crystals grown using self-flux. 27

3.2.5 Temperature dependent resistivity ρ(T) of $Ba(Fe_{1-x}Co_x)_2As_2$ single crystals grown using the self-flux technique: Panel (a) shows ρ(T) of all samples. Panels (b) to (f) compare ρ(T) (normalized to room temperature) with the derivatives of ρ(T) versus temperature. The insets in panels (c) and (d) illustrate how the transition temperatures T_S and T_N have been extracted from the data. [resistivity measurements from G. Friemel] [39] 28

3.2.6 Temperature dependent susceptibility $\chi(T)$ of $BaFe_2As_2$ single crystals. (a) Susceptibility measured at an applied field of $1T\|ab$ plane. (b) Susceptibility measured at an applied field of $6T\|ab$ and $\|c$ planes. 32

3.2.7 (a) Susceptibility $\chi = M/B$ for $Ba(Fe_{1-x}Co_x)_2As_2$ for different doping levels at $H \| ab = 1$ T. (b) Temperature dependent volume susceptibility of superconducting $Ba(Fe_{1-x}Co_x)_2As_2$ single crystals. 33

3.2.8 χ_{ac} vs. Temperature for both real and imaginary components at $\nu_m =$ 9685 Hz and at different H_{dc}. Inset: zoom for $H_{dc} = 30$ kOe around the step-like drop of the real component. The dashed line represents the derivative of the χ'_{ac} with respect to T [55]. 35

3.2.9 Evolution of structural T_S, magnetic T_N, and superconducting T_c, transition temperatures as a function of Co-concentration (x) obtained using EDX in $Ba(Fe_{1-x}Co_x)_2As_2$ single crystal. 36

3.3.1 (a) As grown plate-like single crystals of $Ba_{0.65}Na_{0.35}Fe_2As_2$ (b) Freshly cleaved single crystals of $Ba_{0.75}Na_{0.25}Fe_2As_2$. 37

3.3.2 (a-c) SEM pictures of a $Ba_{0.75}Na_{0.25}Fe_2As_2$single crystal. (d-e) SEM pictures of the $Ba_{0.65}Na_{0.35}Fe_2As_2$ single crystal which shows the typical layer by layer growth. 38

3.3.3 (a) XRD pattern of $Ba_{1-x}Na_xFe_2As_2$ showing only $00l$ reflections. The XRD data were collected using plate-like crystals. 39

3.3.4 (a) Susceptibility $\chi = M/B$ for $Ba_{1-x}Na_xFe_2As_2$ for different doping levels at $H \| ab = 1$ T. The inset shows the derivative of the static susceptibility. (b) Temperature dependence of the volume susceptibilty χ_{vol} following ZFC-FC protocol as described in the text, all data have been collected for $B \|$ ab and the applied field was 20 Oe. 41

3.3.5 In-plane electronic resistivity ρ of $Ba_{1-x}Na_xFe_2As_2$ single crystals for different Na-contents x in dependence of the temperature. Inset: Derivative $d\rho/dT$ around the combined structural and magnetic transition. [data from D. Bombor] 43

3.3.6 Evolution of structural T_S, magnetic T_N, and superconducting T_c, transition temperatures as a function of Na-concentration in $Ba_{1-x}Na_xFe_2As_2$ single crystal. 44

3.4.1 Unified phase diagram, showing structural, magnetic and superconducting regions of electron and hole doped regions in $BaFe_2As_2$ single crystals, dotted lines are guide line to eye. 45

4.1.1 Crystal structure of LiFeAs which is a $Cu_2Sb/PbClF$-type structure, space group P4/nmm [68]. 48

4.2.1 (a) (a) EDX spectrum of a $LiFe_{0.95}Co_{0.05}As$ single crystal. The inset shows a SEM picture. (b) XRD pattern of a $LiFe_{0.95}Co_{0.05}As$ single crystal, the inset exemplarily shows the picture of an as-grown $LiFe_{0.95}Co_{0.05}As$ single crystal with a shiny and metallic-like surface. 50

4.4.1 (a)Temperature dependence of the susceptibilty with an applied field of 1T (b) Temperature dependence of the volume susceptibilty $4\pi\chi_v$ of $LiFe_{0.975}Co_{0.025}As$, $LiFe_{0.95}Co_{0.05}As$ and for $LiFe_{0.925}Co_{0.075}As$ with zero-field cooling (ZFC) and field cooling (FC) in B = 1 Oe. All data have been collected for B$\|$ ab. 54

4.5.1 (a) Temperature dependence of the electrical resistivity $\|$ ab for different Co-doping levels x of $LiFe_{1-x}Co_xAs$, normalized to the room temperature value. [Data from D. Bombor and A. Bachmann] 55

5.1.1 Field induced antiferromagnetic quantum critical point at 5T in KFe_2As_2 [85]. 58

5.1.2 Schematic phase diagram of the local moment-induced QCP in KFe_2As_2 [86]. 59

5.3.1 (a)As-grown single crystals from FeAs flux. (b)SEM pictures of two KFe_2As_2 single crystals grown from FeAs flux. 61

5.3.2 SEM pictures of two KFe_2As_2 single crystals grown from KAs flux. 61

5.4.1 (a)Temperature dependence of the molar susceptibility for both crystals. (b) Temperature dependence of the volume susceptibility for KFe_2As_2 single crystals [86]. 63

5.5.1 Temperature dependence of the resistivity for both crystals, which decreases monotonically showing a metallic behavior at all temperatures. Inset shows the superconducting state. [86] [Data from M. Kumar and V. Grinenko]. 64

5.6.1 (a) Volume susceptibility for $(K_{1-x}Na_x)Fe_2As_2$ single crystals. (b) Temperature dependence of the molar susceptibility for $(K_{0.75}Na_{0.25})Fe_2As_2$ with KFe_2As_2 crystals. 65

5.6.2 (a)The resistivity as a function of temperature for $(K_{0.75}Na_{0.25})Fe_2As_2$ [Data from M. Kumar]. 67

5.6.3 (a) Low field susceptibility measurements and (b) susceptibility with an applied field of 1T for $K(Fe_{0.95}Rh_{0.05})_2As_2$ single crystals. 68

5.6.4 (a) Susceptibility for $K(Fe_{0.95}Co_{0.05})_2As_2$ single crystals as a function of temperature. 69

5.6.5 Normal state susceptibility for $K(Fe_{0.95}Cr_{0.05})_2As_2$ single crystals. 70

6.2.1 (a) (b) SEM images of as grown $(Ba_{0.6}Eu_{0.4})(Fe_{0.85}Co_{0.15})_2As_2$ single crystal from FeAs flux . . . 74

6.3.1 (a)(b)Molar susceptibility as a function of temperature for $BaFe_2As_2$ and $(Ba_{0.6}Eu_{0.4})Fe_2As_2$ single crystals. (c) Temperature dependent resistivty for $BaFe_2As_2$ and $(Ba_{0.6}Eu_{0.4})Fe_2As_2$ single crystals. . . . 76

6.3.2 (a)Temperature dependence of the molar susceptibility, (b)inverse susceptibility as a function of temperature showing the linear paramagnetic behaviour for $(Ba_{0.6}Eu_{0.4})(Fe_{1-x}Co_x)_2As_2$ single crystals. (c)Temperature dependence of the volume susceptibility for two superconducting single crystals. . . . 77

6.4.1 (a)Temperature dependence of resistivty for $(Ba_{0.6}Eu_{0.4})(Fe_{1-x}Co_x)_2As_2$ single crystals. [Data from A. Bachmann] . . . 78

6.5.1 (a) Line width plotted as a function of temperature and (b) Korringa slope as a function of Co-concentration for $(Ba_{0.6}Eu_{0.4})(Fe_{0.9}Co_{0.1})_2As_2$ single crystals [Data from G. Lang] [98] . . . 79

List of Tables

3.2.1 Physical properties of $Ba(Fe_{1-x}Co_x)_2As_2$ single crystals. 34

5.7.1 Physical properties of KFe_2As_2 single crystals. 71

6.6.1 Physical properties of $(Ba_{0.6}Eu_{0.4})(Fe_{1-x}Co_x)_2As_2$ single crystals. 80

List of publications

1. **S. Aswartham**, C. Nacke, G. Friemel, N. Leps, S. Wurmehl, N. Wizent, C. Hess, R. Klingeler, G. Behr, S. Singh, and B. Büchner. "Single crystal growth and physical properties of superconducting ferro-pnictides Ba(Fe,Co)$_2$As$_2$ grown using self-flux and Bridgman techniques" *Journal of Crystal Growth*, 314:341, (2011).

2. **S. Aswartham**, G. Behr, L. Harnagea, D. Bombor, A. Bachmann, I. V. Morozov, V. B. Zabolotnyy, A. A. Kordyuk, T. K. Kim, D. V. Evtushinsky, S. V. Borisenko, A. U. B. Wolter, C. Hess, S. Wurmehl, and B. Büchner. "Suppressed superconductivity in charge-doped Li(Fe$_{1-x}$Co$_x$)As single crystals" *Physical Review B*, 84, 64525, (2011).

3. **S. Aswartham**, M. Abdel-Hafiez, D. Bombor, M. Kumar, A. U. B. Wolter, C. Hess, D. V. Evtushinsky, V. B. Zabolotnyy, A. A. Kordyuk, T. K. Kim, S. V. Borisenko, G. Behr, B. Büchner, and S. Wurmehl. "Hole doping in BaFe$_2$As$_2$: The case of Ba$_{1-x}$Na$_x$Fe$_2$As$_2$ single crystals" *Physical Review B*, 85, 224520, (2012).

4. **S. Aswartham**, S. and Behr, G. and Morozov, I. V. and Roslova, M. and Wolter, A. U. B. and Hess, C. and Wurmehl, S. and Büchner, B., "Influence of doping in KFe$_2$As$_2$ single crystals" *Inpreparation*, (2012).

5. A.K. Pramanik, L. Harnagea, S. Singh, **S. Aswartham**, G. Behr, S. Wurmehl, C. Hess, R. Klingeler, B. Büchner. "Critical current and vortex dynamics in single crystals of Ca(Fe$_{1-x}$Co$_x$)$_2$As$_2$" *Physical Review B*, 82, 14503, (2010).

6. A.K. Pramanik, M. Abdel-Hafiez, **S. Aswartham**, A.U.B. Wolter, S. Wurmehl, V. Kataev, B. Büchner. "Multigap superconductivity in single crystals of $Ba_{0.65}Na_{0.35}Fe_2As_2$: A calorimetric investigation" *Physical Review B*, 84, 64525, (2011).

7. K. Iida, J. Haenisch, M. Schulze, **S. Aswartham**, S. Wurmehl, B. Büchner, L. Schultz, B. Holzapfel. "Generic Fe buffer layers for Fe-based superconductors: Epitaxial $FeSe_{1-x}Te_x$ thin films" *Applied Physics Letters*, 99, 202503, (2011).

8. M. Abdel-Hafiez, **S. Aswartham**, S. Wurmehl, V. Grinenko, C. Hess, S.-L. Drechsler, S. Johnston, A.U.B. Wolter, B. Büchner, H. Rosner, L. Boeri "Specific heat and upper critical fields in KFe_2As_2 single crystals" *Physical Review B*, 85, 134533, (2012).

9. S.-H. Baek, H.-J. Grafe, F. Hammerath, M. Fuchs, C. Rudisch, L. Harnagea, **S. Aswartham**, S. Wurmehl, J. van den Brink, B. Büchner "^{75}As NMR-NQR study in superconducting LiFeAs" *The European Physical Journal B*, 85, 159, (2012).

10. N. Qureshi, P. Steffens, S. Wurmehl, **S. Aswartham**, B. Büchner, and M. Braden "Local magnetic anisotropy in $BaFe_2As_2$: a polarized inelastic neutron scattering study" *arXiv:1201.2332*, (2012).

11. A. K. Pramanik, **S. Aswartham**, A. U. B. Wolter, S. Wurmehl, V. Kataev, and B. Büchner "Flux jumps and vortex pinning in $Ba_{0.65}Na_{0.35}Fe_2As_2$ single crystals" *Physical Review B*, submitted, (2012).

12. D. V. Evtushinsky, V. B. Zabolotnyy, T. K. Kim, A. A.Kordyuk, A. N. Yaresko, J. Maletz, **S. Aswartham**, S. Wurmehl, A. V. Boris, D. L. Sun, C. T. Lin, B. Shen, H. H. Wen, A. Varykhalov, R. Follath, B. Büchner, and S. V. Borisenko "Strong pairing at iron $3_{dxz,yz}$ orbitals in hole-doped $BaFe_2As_2$" *arXiv:1204.2432*, (2012).

13. V. Grinenko, M. Abdel-Hafiez, **S. Aswartham**, A.U.B. Wolter-Giraud, C. Hess, M. Kumar, S. Wurmehl, K. Nenkov, G. Fuchs, B. Holzapfel, S.-L. Drechsler, and B. Büchner "KFe_2As_2: coexistence of superconductivity and local moment derived spin-

glass phases" *arXiv:1203.1585*, (2012).

14. G. Prando, R. Giraud, M. Abdel-Hafiez, **S. Aswartham**, A. U. B. Wolter, S. Wurmehl, and B. Büchner "Unveiling the vortex-glass phase transition in superconducting Ba(Fe$_{0.9}$Co$_{0.1}$)$_2$As$_2$" *arXiv:1207.2457*, (2012).

15. R. Kraus, V. Bisogni, L. Harnagea, **S. Aswartham**, S. Wurmehl, B. Büchner, J. Geck, G. Levy, I. S. Elfimov, and G.A. Sawatzky "Electron spectroscopy of transition metal impurities in iron pnictides" *Physical Review Letters*, submitted, (2012).

16. G. Lang, A. Alfonsov, R. Zahn, V. Kataev, **S. Aswartham**, S. Wurmehl, A. Bachmann, C. Hess, B. Büchner. "ESR measurements of (Ba$_{0.6}$Eu$_{0.4}$)Fe$_2$As$_2$ single crystals" *In preparation*, (2012).

17. O. Vakaliuk, M. Kumar, D. Evtushinsky, A.Yaresko, S. Wurmehl, **S. Aswartham**, C. Hess, and B. Büchner "Out-of-plane Resistivity Anisotropy study on BNFA and BFCA superconductors" *In preparation*, (2012).

18. H. Maeter, H. H. Klauss, J. Knolle, R. Moessner, **S. Aswartham**, S. Wurmehl, G. Behr, B. Büchner, H. Luetkens, G. Pascua, Z. Shermadini, A. Amato and I. Eremin "Microscopic Coexistence of Superconductivity and Magnetic Order in Ba$_{1-x}$Na$_x$Fe$_2$As$_2$" *In preparation*, (2012).

Bibliography

[1] H. K. Onnes. *Commun. Phys. Lab. Univ. Leiden*, 12:120, 1911.

[2] W. Meissner and R. Ochsenfeld. *Natur-Wissenschaften*, 21:787, 1933.

[3] V.L. Ginzburg and L.D. Landau. *Zh. Eksp. Teor. Fiz.*, 20:1064, 1950.

[4] J. Bardeen, L. N. Cooper, and J. R. Schrieffer. *Phys. Rev.*, 106:162–164, 1957.

[5] US. Department of Energy Basic Energy Sciences. 2011.

[6] F. Steglich, J. Aarts, C. D. Bredl, W. Lieke, D. Meschede, W. Franz, and H. Schäfer. *Physical Review Letters*, 43:1892–1896, 1979.

[7] J. G. Bednorz and K. A. Müller. *Zeitschrift für Physik B Condensed Matter*, 64:189–193, 1986.

[8] Y. Maeno, H. Hashimoto, K. Yoshida, S. Nishizaki, T. Fujita, J. G. Bednorz, and F. Lichtenberg. *Nature*, 372:532–534, 1994.

[9] Y. Kamihara, T. Watanabe, M. Hirano, and H. Hosono. *Journal of the American Chemical Society*, 130:3296, 2008.

[10] *Superconductivity, Fundamentals and Applications.* Buckel, W. and Kleiner, R., WILEY-VCH, Weinheim, 2004.

[11] H.-H. Wen and S. Li. *Annual Review of Condensed Matter Physics.*, 2011.

[12] Z. A. Ren, W. Lu, J. Yang, W. Yi, X. L. Shen, Z. C. Li, G. C. Che, X. L. Dong, L. L. Sun, F. Zhou, and Z. X. Zhao. *Chinese Physics Letters*, 25:2215, 2008.

[13] H. Luetkens, H. H. Klauss, M. Kraken, F. J. Litterst, T. Dellmann, R. Klingeler, C. Hess, R. Khasanov, A. Amato, C. Baines, M. Kosmala, O. J. Schumann, M. Braden, J. Hamann Borrero, N. Leps, A. Kondrat, G. Behr, J. Werner, and B. Büchner. *Nature Materials*, 8:305, 2009.

[14] C. de la Cruz, Q. Huang, J. W. Lynn, J. Li, W. Ratcliff II, J. L. Zarestky, H. A. Mook, G. F. Chen, J. L. Luo, N. L. Wang, and P. Dai. *Nature*, 453:0028–0836, 2008.

[15] A. J. Drew, Ch. Niedermayer, P. J. Baker, F. L. Pratt, S. J. Blundell, T. Lancaster, R. H. Liu, G. Wu, X. H. Chen, I. Watanabe, V. K. Malik, A. Dubroka, M. Rossle, K. W. Kim, C. Baines, and C. Bernhard. *Nature Materials*, 8:310–314, 2009.

[16] M. Rotter, M. Tegel, D. Johrendt, I. Schellenberg, W. Hermes, and R. Pöttgen. *Physical Review B*, 78:020503, 2008.

[17] F. Ronning, T. Klimczuk, E. D. Bauer, H. Volz, and J. D. Thompson. *Journal of Physics: Condensed Matter*, 20:322201, 2008.

[18] J.-Q. Yan, A. Kreyssig, S. Nandi, N. Ni, S. L. Bud'ko, A. Kracher, R. J. McQueeney, R. W. McCallum, T. A. Lograsso, A. I. Goldman, and P. C. Canfield. *Physical Review B*, 78:024516, 2008.

[19] H. S. Jeevan, Z. Hossain, D. Kasinathan, H. Rosner, C. Geibel, and P. Gegenwart. *Physical Review B*, 78:052502, 2008.

[20] Z. Ren, Z. Zhu, S. Jiang, X. Xu, Q. Tao, C. Wang, C. Feng, G. Cao, and Z. Xu. *Physical Review B*, 78:052501, 2008.

[21] Basov and Chubukov. *Nature Physics.*, 7:272–276, 2011.

[22] H. Chen, Y. Ren, Y. Qiu, B. Wei, R. H. Liu, G. Wu, T. Wu, Y. L. Xie, X. F. Wang, Q. Huang, and X. H. Chen. *Europhysics Letters*, 85:17006, 2009.

[23] X. F. Wang, T. Wu, G. Wu, R. H. Liu, H. Chen, Y. L. Xie, and X. H. Chen. *New Journal of Physics*, 11:045003, 2009.

[24] J. H. Tapp, Z. Tang, B. Lv, K. Sasmal, B. Lorenz, P. C. W. Chu, and A. M. Guloy. *Physical Review B*, 78:060505, 2008.

[25] D. R. Parker, M. J. Pitcher, P. J. Baker, I. Franke, T. Lancaster, S. J. Blundell, and S. J. Clarke. *Chemical Communications*, 16:2189, 2009.

[26] S. Li, C. de la Cruz, Q. Huang, G. F. Chen, T.-L. Xia, J. L. Luo, N. L. Wang, and P. Dai. *Physical Review B*, 80:020504, 2009.

[27] F. C. Hsu, J. Y. Luo, K. W. Yeh, T. K. Chen, T. W. Huang, P. M. Wu, Y. C. Lee, Y. L. Huang, Y. Y. Chu, D. C. Yan, and M. K. Wu. *Proceedings of the National Academy of Sciences*, 105:14262–14264, 2008.

[28] K. W. Yeh, T. W. Huang, Y. L. Huang, T. K. Chen, F. C. Hsu, P. M. Wu, Y. C. Lee, Y. Y. Chu, C. L. Chen, J. Y. Luo, D. C. Yan, and M. K. Wu. *Europhysics Letters*, 84:37002, 2008.

[29] S. Li, C. de la Cruz, Q. Huang, Y. Chen, J. W. Lynn, J. Hu, Y-L. Huang, F-C. Hsu, K-W. Yeh, M-K. Wu, and P. Dai. *Physical Review B*, 79:054503, 2009.

[30] N. D. Zhigadlo, S. Katrych, Z. Bukowski, S. Weyeneth, R. Puzniak, and J. Karpinski. *Journal of Physics: Condensed Matter*, 20:342202, 2008.

[31] Claudia Nacke. *Thesis.*, IFW-Dresden, 2012.

[32] *The Growth of Single Crystals.* R.A. Laudise, Prentice-Hall, Inc, New Jersey, 1970.

[33] *ASM Handbook, Materials characterization*, volume 10. Inductively Coupled Plasma Atomic Emission Spectroscopy, Materials Park, OH.

[34] M. Rotter, M. Tegel, and D. Johrendt. *Physical Review Letters*, 101:107006, 2008.

[35] A. S. Sefat, R. Jin, M. A. McGuire, B. C. Sales, D. J. Singh, and D. Mandrus. *Physical Review Letters*, 101, 2008.

[36] T. Yamazaki, N. Takeshita, R. Kobayashi, H. Fukazawa, Y. Kohori, K. Kihou, C-H. Lee, H. Kito, A. Iyo, and H. Eisaki. *Physical Review B*, 81:224511, 2010.

[37] J. Shuai, X. Hui, X. Guofang, W. Cao, R. Zhi, F. Chunmu, D. Jianhui, X. Zhuan, and C. Guanghan. *Journal of Physics: Condensed Matter*, 21:382203, 2009.

[38] R. Cortes-Gil, D. R. Parker, M. J. Pitcher, J. Hadermann, and S. J. Clarke. *Chemistry of Materials*, 22:4304–4311, 2010.

[39] S. Aswartham, C. Nacke, G. Friemel, N. Leps, S. Wurmehl, N. Wizent, C. Hess, R. Klingeler, G. Behr, S. Singh, and B. Büchner. *Journal of Crystal Growth*, 314:341, 2011.

[40] N. Qureshi, P. Steffens, S. Wurmehl, S. Aswartham, B. Büchner, and M. Braden. *arXiv:1201.2332*, 2012.

[41] R. Morinaga, K. Matan, H. S. Suzuki, and T. J. Sato. *Japanese Journal of Applied Physics*, 48:013004, 2009.

[42] N. Ni, M. E. Tillman, J.-Q. Yan, A. Kracher, S. T. Hannahs, S. L. Bud'ko, and P. C. Canfield. *Physical Review B*, 78:214515, 2008.

[43] Gerd Friemel. *Diploma Thesis.*, IFW-Dresden, 2010.

[44] X. F. Wang, T. Wu, G. Wu, H. Chen, Y. L. Xie, J. J. Ying, Y. J. Yan, R. H. Liu, and X. H. Chen. *Physical Review Letters*, 102:117005, 2009.

[45] S. D. Wilson, Z. Yamani, C. R. Rotundu, B. Freelon, E. Bourret-Courchesne, and R. J. Birgeneau. *Physical Review B*, 79:184519, 2009.

[46] D. L. Sun, Y. Liu, J. T. Park, and C. T. Lin. *Superconductor Science and Technology*, 22:105006, 2009.

[47] A. S. Sefat, M. A. McGuire, R. Jin, B. C. Sales, D. Mandrus, F. Ronning, E. D. Bauer, and Y. Mozharivskyj. *Physical Review B*, 79:094508, 2009.

[48] C. Lester, J. H. Chu, J. G. Analytis, S. C. Capelli, A. S. Erickson, C. L. Condron, M. F. Toney, I. R. Fisher, and S. M. Hayden. *Physical Review B*, 79:144523, 2009.

[49] C. Hess, A. Kondrat, A. Narduzzo, J. E. Hamann-Borrero, R. Klingeler, J. Werner, G. Behr, and B. Büchner. *Europhysics Letters*, 87:17005, 2009.

[50] A. Kondrat, J. E. Hamann-Borrero, N. Leps, M. Kosmala, O. Schumann, J. Werner, G. Behr, M. Braden, R. Klingeler, B. Büchner, and C. Hess. *Europhysics Letters*, 70:461, 2009.

[51] J.-H. Chu, J. G. Analytis, C. Kucharczyk, and I. R. Fisher. *Physical Review B.*, 79:014506, 2009.

[52] A. K. Pramanik, L. Harnagea, S. Singh, S. Aswartham, G. Behr, S. Wurmehl, C. Hess, R. Klingeler, and B. Büchner. *Physical Review B*, 82:014503, 2010.

[53] Y. Laplace, J. Bobroff, F. Rullier-Albenque, D. Colson, and A. Forget. *Physical Review B*, 80:140501, 2009.

[54] M. H. Julien, H. Mayaffre, M. Horvatic, C. Berthier, X. D. Zhang, W. Wu, G. F. Chen, N. L. Wang, and J. L. Luo. *Europhysics Letters*, 87:37001, 2009.

[55] G. Prando, R. Giraud, M. Abdel-Hafiez, S. Aswartham, A. U. B. Wolter, S. Wurmehl, and B Büchner. *submitted to Physical Review Letters*, 2012.

[56] S. Aswartham, M. Abdel-Hafiez, D. Bombor, M. Kumar, A. U. B. Wolter, C. Hess, D. V. Evtushinsky, V. B. Zabolotnyy, A. A. Kordyuk, T. K. Kim, S. V. Borisenko, G. Behr, B. Büchner, and S. Wurmehl. *Physical Review B*, 85:224520, 2012.

[57] A. K. Pramanik, M. Abdel-Hafiez, S. Aswartham, A. U. B. Wolter, S. Wurmehl, V. Kataev, and B. Büchner. *Physical Review B*, 84:064525, 2011.

[58] R. R. Urbano, E. L. Green, W. G. Moulton, A. P. Reyes, P. L. Kuhns, E. M. Bittar, C. Adriano, T. M. Garitezi, L. Bufaical, and P. G. Pagliuso. *Physical Review Letters*, 105:107001, 2010.

[59] S. Avci, O. Chmaissem, E. A. Goremychkin, S. Rosenkranz, J.-P. Castellan, D. Y. Chung, I. S. Todorov, J. A. Schlueter, H. Claus, M. G. Kanatzidis, A. Daoud-Aladine, D. Khalyavin, and R. Osborn. *Physical Review B*, 83:172503, 2011.

[60] J. L. Mathieu and S. E. Latturner. *Chemical Communications*, 33:4965, 2009.

[61] R. Klingeler, N. Leps, I. Hellmann, A. Popa, U. Stockert, C. Hess, V. Kataev, H.-J. Grafe, F. Hammerath, G. Lang, S. Wurmehl, G. Behr, L. Harnagea, S. Singh, and B. Büchner. *Physical Review B*, 81:024506, 2010.

[62] B. Shen, H. Yang, Z.-S. Wang, F. Han, B. Zeng, L. Shan, C. Ren, and H.-H. Wen. *Physical Review B*, 84:184512, 2011.

[63] L. Fang, H. Luo, P. Cheng, Z. Wang, Y. Jia, G. Mu, B. Shen, I. I. Mazin, L. Shan, C. Ren, and H.-H. Wen. *Physical Review B*, 80:140508, 2009.

[64] F. Rullier-Albenque, D. Colson, and H. Alloul. *Physical Review Letters*, 103:057001, 2009.

[65] L. Harnagea, S. Singh, G. Friemel, N. Leps, D. Bombor, M. Abdel-Hafiez, A. U. B. Wolter, C. Hess, R. Klingeler, G. Behr, S. Wurmehl, and B. Büchner. *Physical Review B*, 83:094523, 2011.

[66] R. Juza and K. Z. Langer. *Zeitschrift für anorganische und allgemeine Chemie*, 58:361, 1968.

[67] S. J. Zhang, X. C. Wang, R. Sammynaiken, J. S. Tse, L. X. Yang, Z. Li, Q. Q. Liu, S. Desgreniers, Y. Yao, H. Z. Liu, and C. Q. Jin. *Physical Review B*, 80:014506, 2009.

[68] X. C. Wang, Q. Q. Liu, Y. X. Lv, W. B. Gao, L. X. Yang, R. C. Yu, F. Y. Li, and C. Q. Jin. *Solid State Communications*, 148:538–540, 2008.

[69] S. V. Borisenko, V. B. Zabolotnyy, D. V. Evtushinsky, T. K. Kim, I. V. Morozov, A. N. Yaresko, A. A. Kordyuk, G. Behr, A. Vasiliev, R. Follath, and B. Büchner. *Physical Review Letters*, 105:067002, 2010.

[70] P. M. R. Brydon, M. Daghofer, C. Timm, and J. van den Brink. *Physical Review B*, 83:060501, 2011.

[71] S. H. Baek, H. J. Grafe, F. Hammerath, M. Fuchs, C. Rudisch, L. Harnagea, S. Aswartham, S. Wurmehl, J. van den Brink, and B. Büchner. *The European Physical Journal B*, 85:159, 2012.

[72] M. J. Pitcher, D. R. Parker, S. A. Paul, J. C. Herkelrath, A. T. Boothroyd, R. M. Ibberson, M. Brunelli, and S. J. Clarke. *Chemical Communications*, 45:5918, 2008.

[73] D. R. Parker, M. J. P. Smith, T. Lancaster, A. J. Steele, I. Franke, P. J. Baker, F. L. Pratt, M. J. Pitcher, S. J. Blundell, and S. J. Clarke. *Physical Review Letters*, 104:057007, 2010.

[74] M. J. Pitcher, T. Lancaster, J. D. Wright, I. Franke, A. J. Steele, P. J. Baker, F. L. Pratt, W. T. Thomas, D. R. Parker, Blundell S. J., and S. J. Clarke. *Journal of the American Chemical Society*, 132:10467, 2010.

[75] S. Aswartham, G. Behr, L. Harnagea, D. Bombor, A. Bachmann, I. V. Morozov, V. B. Zabolotnyy, A. A. Kordyuk, T. K. Kim, D. V. Evtushinsky, S. V. Borisenko, A. U. B. Wolter, C. Hess, S. Wurmehl, and B. Büchner. *Physical Review B*, 84:054534, 2011.

[76] I. Morozov, A. Boltalin, O. Volkova, A. Vasiliev, O. Kataeva, U. Stockert, M. Abdel-Hafiez, D. Bombor, A. Bachmann, L. Harnagea, M. Fuchs, H. J. Grafe, G. Behr, R. Klingeler, S. V. Borisenko, C. Hess, Wurmehl S., and B. Büchner. *Crystal Growth and Design*, 10:4428, 2010.

[77] J. A. Osborne. *Physical Review.*, 67:351, 1945.

[78] A. S. Sefat, R. Jin, M. A. McGuire, B. C. Sales, D. J. Singh, and D. Mandrus. *Physical Review Letters*, 101:117004, 2008.

[79] F. L. Pratt, P. J. Baker, S. J. Blundell, T. Lancaster, H. J. Lewtas, P. Adamson, M. J. Pitcher, D. R. Parker, and S. J. Clarke. *Physical Review B.*, 79:052508, 2009.

[80] S. Rozsa and H. U. Schuster. *Zeitschrift für Naturforschung B*, 36:1668, 1981.

[81] K. Suzuki, H. Usui, and K. Kuroki. *Physical Review B*, 84:144514, 2011.

[82] C. H. Lee, K. Kihou, H. Kawano-Furukawa, T. Saito, A. Iyo, H. Eisaki, H. Fukazawa, Y. Kohori, K. Suzuki, H. Usui, K. Kuroki, and K. Yamada. *Physical Review Letters*, 106:067003, 2011.

[83] T. Sato, K. Nakayama, Y. Sekiba, P. Richard, Y.-M. Xu, S. Souma, T. Takahashi, G. F. Chen, J. L. Luo, N. L. Wang, and H. Ding. *Physical Review Letters*, 103:047002, 2011.

[84] N. Pascher, J. Deisenhofer, H.-A. Krug von Nidda, M. Hemmida, H. S. Jeevan, P. Gegenwart, and A. Loidl. *Physical Review B*, 82:054525, 2010.

[85] J. K. Dong, S. Y. Zhou, T. Y. Guan, H. Zhang, Y. F. Dai, X. Qiu, X. F. Wang, Y. He, X. H. Chen, and S. Y. Li. *Physical Review Letters*, 104:087005, 2010.

[86] V. Grinenko, M. Abdel-Hafiez, S. Aswartham, A. U. B. Wolter-Giraud, C. Hess, M. Kumar, S. Wurmehl, K. Nenkov, G. Fuchs, B. Holzapfel, S.-L. Drechsler, and B. Büchner. *arXiv:1203.1585v1*, 2011.

[87] M. Abdel-Hafiez, S. Aswartham, S. Wurmehl, V. Grinenko, S.-L. Drechsler, A. U. B. Wolter, B. Büchner, H. Rosner, and L. Boeri. *Physical Review B*, 85:134533, 2012.

[88] K. Kihou, T. Saito, S. Ishida, M. Nakajima, Y. Tomioka, H. Fukazawa, Y. Kohori, T. Ito, S. Uchida, A. Iyo, C. Lee, and H. Eisaki. *Journal of the Physical Society of Japan*, 79(12):124713, 2010.

[89] V. Grinenko, K. Kikoin, S-L. Drechsler, G. Fuchs, K. Nenkov, S. Wurmehl, F. Hammerath, G. Lang, H-J. Grafe, B. Holzapfel, J. van den Brink, B. Büchner, and L. Schultz. *Physical Review B*, 84:134516, 2011.

[90] F. Hammerath, S.-L. Drechsler, H.-J. Grafe, G. Lang, G. Fuchs, G. Behr, I. Eremin, M. M. Korshunov, and B. Büchner. *Phys. Rev. B*, 81:140504, 2010.

[91] K. Hashimoto, A. Serafin, S. Tonegawa, R. Katsumata, R. Okazaki, T. Saito, H. Fukazawa, Y. Kohori, K. Kihou, C. H. Lee, A. Iyo, H. Eisaki, H. Ikeda, Y. Matsuda, A. Carrington, and T. Shibauchi. *Physical Review B*, 82:014526, 2010.

[92] J. S. Kim, E. G. Kim, G. R. Stewart, X. H. Chen, and X. F. Wang. *Physical Review B*, 83:172502, 2011.

[93] A. F. Wang, S. Y. Zhou, X. G. Luo, X. C. Hong, Y. J. Yan, J. J. Ying, P. Cheng, G. J. Ye, Z. J. Xiang, S. Y. Li, and X. H. Chen. *arXiv:1206.2030*, 2012.

[94] S. Aswartham, G. Behr, I. V. Morozov, M. Roslova, A. U. B. Wolter, C. Hess, S. Wurmehl, and B. Büchner. *Inpreparation*, 2012.

[95] J. J. Ying, T. Wu, Q. J. Zheng, Y. He, G. Wu, Q. J. Li, Y. J. Yan, Y. L. Xie, R. H. Liu, X. F. Wang, and X. H. Chen. *Physical Review B*, 81:052503, 2010.

[96] C. F. Miclea, M. Nicklas, H. S. Jeevan, D. Kasinathan, Z. Hossain, H. Rosner, P. Gegenwart, C. Geibel, and F. Steglich. *Physical Review B*, 79:212509, 2009.

[97] J. Shuai, L. Yongkang, R. Zhi, Z. Zengwei, W. Cao, X. Xiangfan, T. Qian, C. Guanghan, and X. Zhuán. *New Journal of Physics*, 11(2):025007, 2009.

[98] G. Lang, A. Alfonsov, R. Zahn, V. Kataev, S. Aswartham, S. Wurmehl, A. Bachmann, C. Hess, and B. Büchner. *In preparation*, 2012.

[99] A. Alfonsov, F. Murányi, V. Kataev, G. Lang, N. Leps, L. Wang, R. Klingeler, A. Kondrat, C. Hess, S. Wurmehl, A. Köhler, G. Behr, S. Hampel, M. Deutschmann, S. Katrych, N. D. Zhigadlo, Z. Bukowski, J. Karpinski, and B. Büchner. *Physical Review B*, 83:094526, 2011.

[100] Alexey Alfonsov. *PhD Thesis.*, IFW-Dresden, 2011.

[101] J. J. Ying, T. Wu, Q. J. Zheng, Y. He, G. Wu, Q. J. Li, Y. J. Yan, Y. L. Xie, R. H. Liu, X. F. Wang, and X. H. Chen. *Physical Review B*, 81:052503, 2010.

Acknowledgements

First and foremost I would like to thank Prof. Dr. Bernd Büchner for providing me the opportunity to do PhD in Leibniz Institute for Solid State and Materials Research (IFW), in association with department of physics at the Technical University of Dresden. Secondly I would like to thank Dr. Günter Behr who gave me amazing support and for offering me to work for my PhD in his crystal growth group. I show my deep gratitude to my advisor Dr. Sabine Wurmehl, the group leader of crystal growth laboratory, for her constant encouragement and willingness to help.

Special thanks to Prof. Dr. Claudia Felser, who straight forwardly agreed in reviewing my PhD work.

As the list of the people appears to be endless, I express my sincere thanks to each and everyone, who helped me either directly or indirectly during the course of my PhD work. Thanks to all the members of the crystal group, especially to M. Deutschmann for her incredible energy and the working sprit in the chemistry lab and also thanks to J. Werner, S. Müller-Litvanyi, R. Müller, K. Leger, S. Gaß, S. Pichl for the technical support in the lab. Thanks to Dr. W. Löser, M. Sakaliyska, C. Blum for nice scientific and non scientific discussions especially during and after the group meeting.

This is the opportunity to say thank you to the group leaders of the IFF namely Dr. Hans-Joachim Grafe, Dr. Jochen Geck, Dr. Christian Hess, Dr. Anja Wolter, and also to Prof. Dr. Ruediger Klingeler. I would like to say thank you for the fellow students of IFF with whom I have had a wonderful time in the past 3 years. Franziska, Mahmoud, Yulieth, Daniil, Diana, Norman, Wolfram, Claudia, Alexey, Markus, Steve, Omar, Yulia, Sven, Jorge, Oleksii, Steffen.

Beerstube, my official second office where lot of stimulating scientific discussions took place in the past 3 years has to be acknowledged here. In fact, it is this place where most of my PhD conception had taken place. Thanks to Beerstube and the fellow usual suspects who accompany me in Beerstube.

I wish to express my sincere thanks to all my friends in Dresden, at first to the fellow 2 Musketeers of the 3, Juhnee Han and Sandeep Gorantla, thank you for your great support guys. Special thanks to Michael Schulze for his constant and consistent support. Thanks also to Christoph and Dominik. There are two special persons in my life, my brother-in-law A. N. Prasad and my best friend Ravikumar to whom I deeply owe, with out their support I wouldn´t have been what I am today. Last but not the least I thank my loving sisters and my parents.

Eidesstattliche Erklärung

Die Arbeit wurde von Aug 2009 bis Juli 2012 am Leibniz-Institut für Festkörper- und Werkstofforschung Dresden unter Betreuung von Prof. Dr. Bernd Büchner sowie Dr. Sabine Wurmehl angefertigt.

Hiermit versichere ich, dass ich die vorliegende Arbeit ohne unzulässige Hilfe Dritter und ohne Benutzung anderer als der angegebenen Hilfsmittel angefertigt habe; die aus fremden Quellen direkt oder indirekt übernommenen Gedanken sind als solche kenntlich gemacht. Die Arbeit wurde bisher weder im Inland noch im Ausland in gleicher oder ähnlicher Form einer anderen Prüfungsbehörde vorgelegt. Ich erkenne hiermit die Promotionsordnung der Technischen Universität Dresden an.

Dresden, 14. August 2012